226 + 120 + 79 FAST REACTOR ~~FUELS AND MATERIALS~~ Reactor Safety 784

ANL-7550

ANL-7550

7/1/69

RE A+B Formula

MASTER

# Argonne National Laboratory

## CHEMICAL ENGINEERING DIVISION RESEARCH HIGHLIGHTS

May 1968—December 1968

## DISCLAIMER

The facilities of Argonne National Laboratory are owned by the United States Government. Under the terms of a contract (W-31-109-Eng-38) between the U. S. Atomic Energy Commission, Argonne Universities Association and The University of Chicago, the University employs the staff and operates the Laboratory in accordance with policies and programs formulated, approved and reviewed by the Association.

MEMBERS OF ARGONNE UNIVERSITIES ASSOCIATION

The University of Arizona
Carnegie-Mellon University
Case Western Reserve University
The University of Chicago
University of Cincinnati
Illinois Institute of Technology
University of Illinois
Indiana University
Iowa State University
The University of Iowa
Kansas State University
The University of Kansas
Loyola University
Marquette University
Michigan State University
The University of Michigan
University of Minnesota
University of Missouri
Northwestern University
University of Notre Dame
The Ohio State University
Ohio University
The Pennsylvania State University
Purdue University
Saint Louis University
Southern Illinois University
University of Texas
Washington University
Wayne State University
The University of Wisconsin




Printed in the United States of America
Available from
Clearinghouse for Federal Scientific and Technical Information
National Bureau of Standards, U. S. Department of Commerce
Springfield, Virginia 22151
Price: Printed Copy $3.00; Microfiche $0.65

ANL-7550
General, Miscellaneous,
and Progress Reports

ARGONNE NATIONAL LABORATORY
9700 South Cass Avenue
Argonne, Illinois 60439

# CHEMICAL ENGINEERING DIVISION RESEARCH HIGHLIGHTS

May 1968–December 1968

R. C. Vogel, Division Director
M. Levenson, Associate Division Director
E. R. Proud, Assistant Division Director
J. Royal

THIS PAGE

WAS INTENTIONALLY

LEFT BLANK

# TABLE OF CONTENTS

# TABLE OF CONTENTS

# TABLE OF CONTENTS

# I. COMPACT PYROCHEMICAL PROCESSES

## A. Salt Transport Process for Fast Breeder Reactor Fuels

Research and development work has continued on compact pyrochemical processes for the recovery and purification of ceramic (oxide or carbide) fuels for fast breeder reactors. The studies have been concentrated on the development of a process employing salt transport separations. Salt transport separations are based on the selective transfer of a solute (plutonium or uranium) from one liquid metal solution (donor alloy) to another metal solution (acceptor alloy) by cycling a molten chloride salt between the two metal solutions.

The basic steps of the proposed process are shown in Fig. I-1. This process is being designed to handle short-cooled fuel with plutonium and uranium recoveries exceeding 99% and decontamination factors possibly greater than $10^6$.

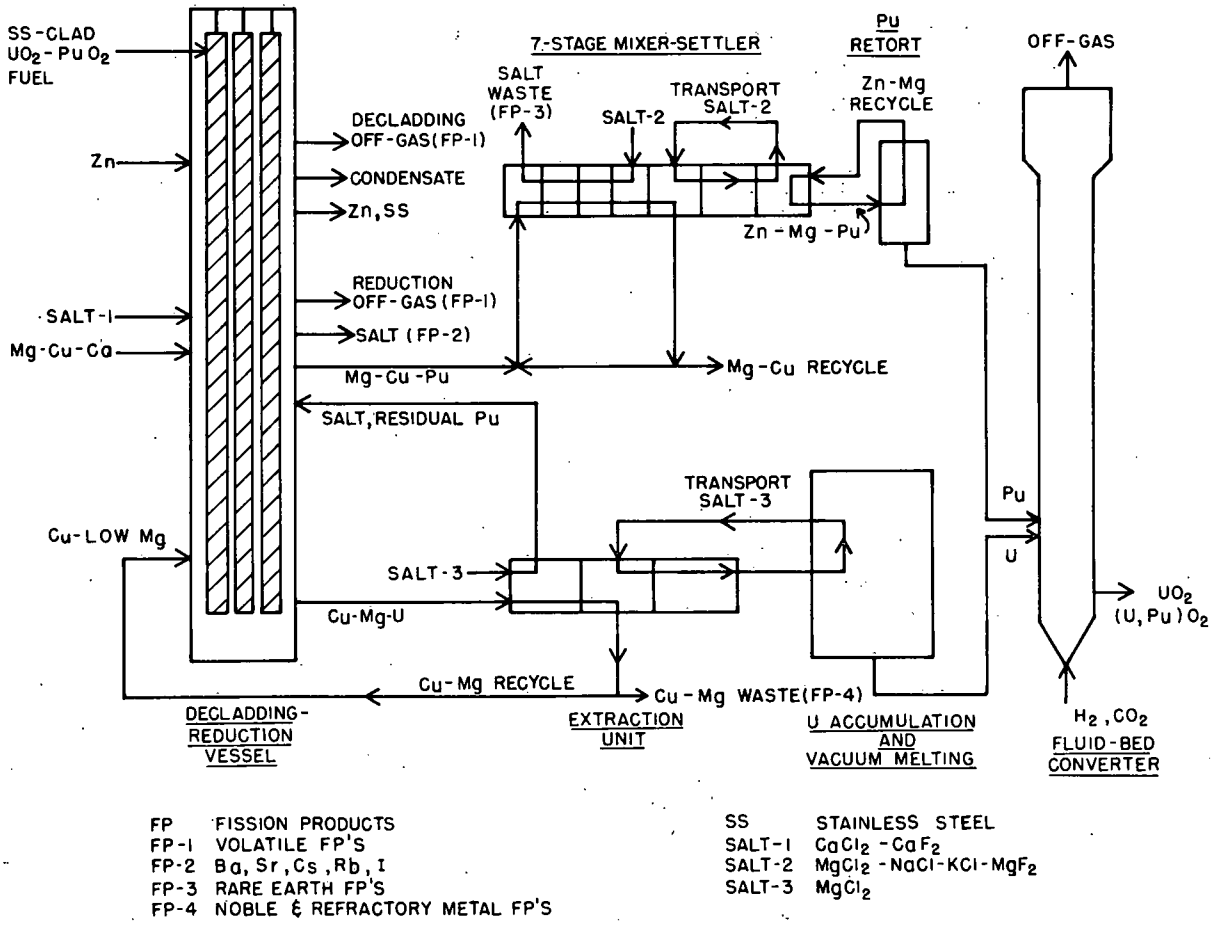


Fig. I-1. Conceptual Pyrochemical Flowsheet for Fast Breeder Reactor Fuels.

1. Decladding and Feed Preparation

In this step, spent fuel assemblies, after having their end hardware trimmed, are immersed in liquid zinc at 800 to 900°C, which selectively dissolves the stainless steel cladding and structural material. The zinc-stainless steel solution is then transferred away from the oxide fuel. The residual zinc is vacuum distilled away from the fuel and is collected in a condenser along with the released volatile fission products (FP-1) and any coolant sodium that may have adhered to the fuel subassembly. The oxide fuel is then reduced in the same vessel at 800°C by calcium metal in a Mg-42 at. % Cu-3 at. % Ca alloy that is added to the vessel along with a $CaCl_2$-20 mol % $CaF_2$ reduction salt. The salt, which contains the CaO by-product of the reaction and the fission products designated FP-2 in Fig. I-1, becomes a waste stream. The gaseous and volatile fission products (FP-1) are collected in an argon atmosphere in the decladding and reduction vessel. After the reduction, the metallic plutonium is in solution in the Mg-Cu alloy. The uranium and noble and refractory metal fission products (FP-4) precipitate. Plutonium and uranium accountability can be achieved readily in the decladding and reduction vessel by analyzing samples of the liquid metal solutions that contain these elements and then accurately weighing the solutions.

2. Plutonium Purification

The Mg-Cu-Pu alloy is transferred away from the uranium precipitate to a semicontinuous mixer-settler battery for removal of the remaining fission products. Seven stages are required to achieve an estimated overall decontamination factor of $10^6$. In this unit a $MgCl_2$-18 mol % NaCl-12 mol % KCl-3 mol % $MgF_2$ salt mixture is employed as the rare earth (FP-3) extraction salt in stages 1, 2, 3, and 4. This salt then becomes a waste stream. In stages 5, 6, and 7, a salt of the same composition is used to transport the plutonium from the Mg-Cu alloy to a Zn-Mg alloy by cycling the salt between the two alloys at 600°C. The Mg-Cu alloy, which contains the noble and refractory metal fission products (FP-4), is recycled.

3. Plutonium Recovery

Zinc and magnesium are vacuum distilled from the plutonium product solution in a retort having a slab geometry. The Zn-Mg-Pu solution from the seven-stage extraction unit is intermittently charged to the retort, and the bulk of the Zn-Mg is evaporated leaving the plutonium in the vessel as a liquid. After the desired amount of plutonium has been charged (within criticality limitations), and the distillation has been continued until the purity of the accumulated plutonium is high, the plutonium product is transferred from the system.

4. Uranium Recovery

Because of the low value of uranium in a fast breeder reactor fuel cycle, the requirements for uranium processing are uncertain. The uranium precipitate in the reduction vessel can be decontaminated and recovered by dissolving it in a Cu-13 at. % Mg alloy at 900°C and salt-transporting it to a Zn-Mg acceptor alloy at 830°C. The acceptor alloy would subsequently be transferred from the uranium, and the uranium would be consolidated by melting under vacuum. An alternative method of handling the uranium would be to wash the uranium precipitate with liquid magnesium and then dissolve the precipitate in a Cu-6 at. % Mg-3.5 at. % U solution or in a U-18 at. % Fe solution and send it to storage for deferred processing. In both uranium processing schemes, any residual plutonium present would be extracted into $MgCl_2$ salt and recycled to the reduction step.

5. Fuel Resynthesis

The metallic uranium and plutonium products can be converted to $(U, Pu)O_2$ core fuel by reaction with a $CO_2$-$H_2$ mixture in a fluidized bed, and the uranium metal can be converted to $UO_2$ blanket material by the same process.

B. Chemical Investigations in Support of Pyrochemical Processes

1. Oxide Reduction Studies

The reduction of the mixed plutonium-uranium oxide fuel to metallic uranium and plutonium is a key step in the salt transport process. This reduction is achieved by vigorously mixing the solid oxide fuel pellets with a molten $CaCl_2$-$CaF_2$ salt mixture and a liquid Mg-Cu-Ca alloy. The products of this reaction are metallic uranium and plutonium and CaO. Plutonium is soluble in the liquid alloy, and CaO is soluble in the molten salt. Uranium has a low solubility in the liquid alloy and precipitates in it. The results of studies with $UO_2$ that led to the choice of this alloy and salt for the reduction step strongly indicated that the main reaction proceeds through dissolution of calcium from the alloy into the molten salt, transport of the calcium through the salt to the $UO_2$-salt interface, and reaction of the calcium with the $UO_2$ to produce metallic uranium and CaO.

Recent experiments showed that single pellets of $UO_2$ were reduced much faster when they were immersed in a molten salt in contact with a liquid Mg-Cu-Ca alloy than when immersed in the alloy itself. The rate of reduction per unit area of $UO_2$ surface, at a constant temperature and a fixed concentration of calcium in molten $CaCl_2$, was found to increase with time to a constant value. The rate of reduction per unit area was directly proportional to the concentration of calcium in molten $CaCl_2$. A relatively

small increase in the reaction rate with temperature over the range from 750 to 850°C suggests that the rate of the reduction reaction is controlled by the transport of calcium from the liquid alloy through the salt to the reaction site.

Portions of solidified salt containing partially reduced $UO_2$ pellets from the studies mentioned above were sectioned, polished, and examined. A photomicrograph of a typical portion is shown in Fig. I-2. This photograph shows that the products of the reduction reaction form concentric layers around the $UO_2$ pellet. Layers of metallic uranium containing small amounts of dispersed alkaline earth chlorides and oxides alternate with layers of alkaline earth chlorides and oxides containing small amounts of metallic uranium. The layers are discontinuous in many places, and, therefore, do not form an impervious layer to inhibit the reduction reaction.

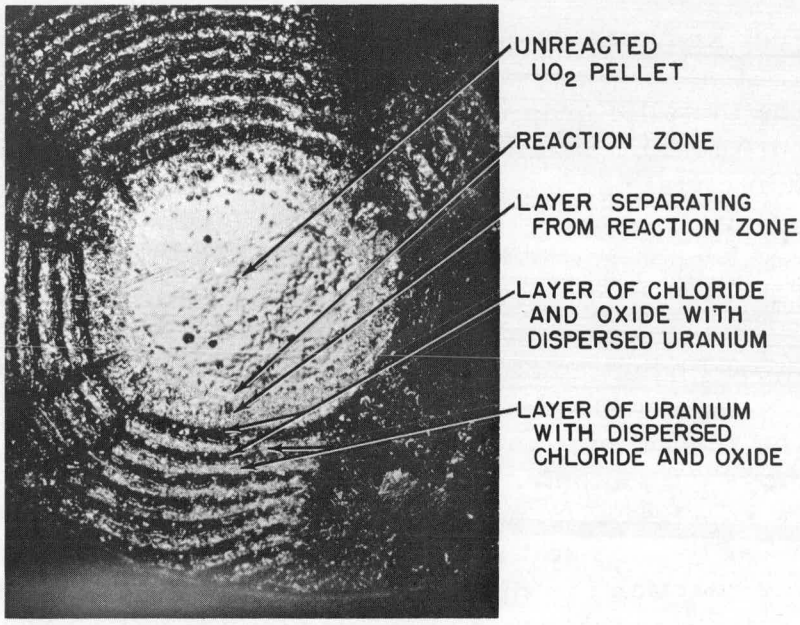


Fig. I-2. Photomicrograph of Layers of Reaction Products Surrounding Partially Reduced $UO_2$ Pellet.

## 2. Phase Studies of the $CaCl_2$-Rich Region of the $CaCl_2$-$CaF_2$-CaO System

The phase diagram of the $CaCl_2$-rich region of the $CaCl_2$-$CaF_2$-CaO system has been studied to provide the necessary information for selecting the salt composition for the reduction step. The phase diagram obtained by thermal analysis is shown in Fig. I-3. The $CaCl_2$-$CaF_2$ binary side of the diagram is in good agreement with previous work.[1] The $CaCl_2$-CaO binary differs from previous work in that a peritectic

[1] G. A. Bukholova, A. G. Bergman, Zh. Ob. Khim. 21, 1723 (1951).

was found at 18.5 mol % CaO and 835°C. The incongruently melting compound is CaO · 2 $CaCl_2$. Previous work[2] indicated the existence of a congruently melting compound CaO · 4 $CaCl_2$ and a eutectic at about 22 mol % CaO.

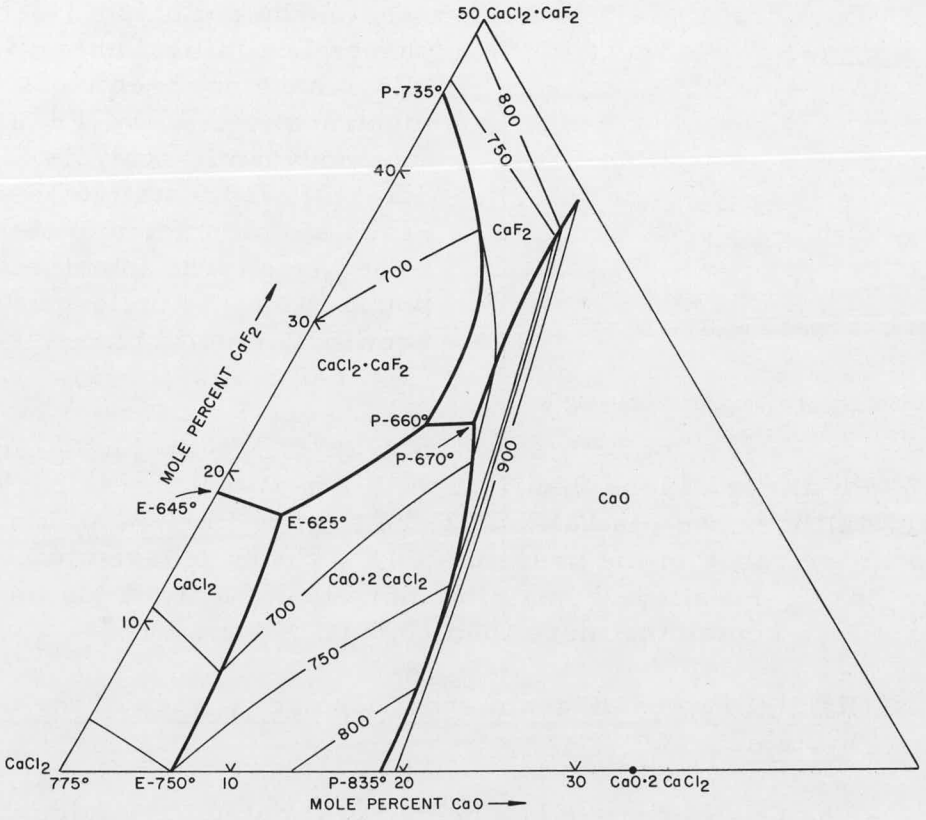


Fig. I-3. Phase Diagram of the $CaCl_2$-Rich Region of the $CaCl_2$-$CaF_2$-CaO System (temperatures in °C).

The present ternary diagram (Fig. I-3) contains a ternary eutectic at $CaCl_2$-17 mol % $CaF_2$-4 mol % CaO and 625°C, and ternary peritectics at $CaCl_2$-23 mol % $CaF_2$-10 mol % CaO and 660°C and at $CaCl_2$-23 mol % $CaF_2$-13 mol % CaO and 670°C. The various phase fields are shown on the diagram.

## 3. Solubility of Plutonium in Liquid Zn-Mg Alloys

Knowledge of the phase relations in the zinc-rich region of the Zn-Mg-Pu system is required to specify the temperature and composition of the acceptor alloy for the salt transport step of the pyrochemical process.

Recent experimental results extend our knowledge of the solubility of plutonium in the Zn-Mg-Pu system to higher temperatures

[2] B. Newmann, C. Kröger, H. Jüttner, Z. Elektrochem. 41, 725 (1935).

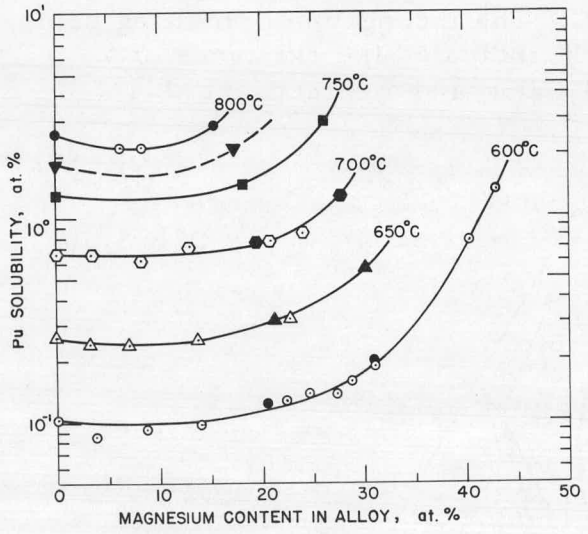


Fig. I-4. Solubility of Plutonium in Zn-Mg Alloy.

and higher magnesium concentrations. These new data (solid symbols) are presented together with previous data[3,4] (open symbols) in Fig. I-4.

The plutonium intermetallic phases in equilibrium with the liquid alloys have not been isolated for identification. However, a previous thermodynamic analysis of the data[5] allowed tentative assignments of the stoichiometry of the phases to be made. The intermetallic compound $PuZn_{12}$ is believed to be the equilibrium solid phase present in (1) Zn-Pu alloys below 710°C, (2) Zn-Mg-Pu alloys of less than 6.2 at. % Mg at 700°C, and (3) Zn-Mg-Pu alloys of less than 16.8 at. % Mg at 600°C. Above 710°C, the intermetallic $Pu_2Zn_{17}$ is believed to be the equilibrium solid phase in the composition range of the present study, as it is believed to be at 700°C for Zn-Mg-Pu alloys containing more than 6.2 at. % Mg and at 600°C for alloys containing more than 16.8 at. % Mg.

### 4. Partial Phase Diagram and Thermodynamics of the Cd-Np System

The Cd-Np system has been investigated to provide data that may be used to develop a neptunium recovery step in the salt transport process. The study closely parallels an investigation that was made of the Cd-Pu system.[6] In the present study, the solubility of neptunium in liquid cadmium was determined over a temperature range from 327 to 626°C. When the logarithm of the solubility was plotted against the reciprocal of the absolute temperature, the data were found to be best represented by two straight lines that intersect at 485 ± 3°C. The equilibrium solid phase below 485°C was shown to be $NpCd_{11}$, which has a cubic structure (isotopic with $BaHg_{11}$) with a lattice parameter of 9.288 Å. Above 485°C, and up to at least 626°C, the equilibrium solid phase is $NpCd_6$, which has a cubic structure (isotopic with $CeCd_6$) with a lattice parameter of 15.614 Å. The phase diagram derived from these data is shown in Fig. I-5.

[3] I. Johnson, M. G. Chasanov, J. Inorg. Nucl. Chem. 26, 2059 (1964).

[4] J. B. Knighton, K. R. Tobias, in "Chemical Engineering Division Semiannual Report, January-June 1967," ANL-7375, p. 25 (October 1967).

[5] I. Johnson, ibid., p.31.

[6] I. Johnson, M. G. Chasanov, R. M. Yonco, Trans. Met. Soc. AIME 233, 1408 (1965).

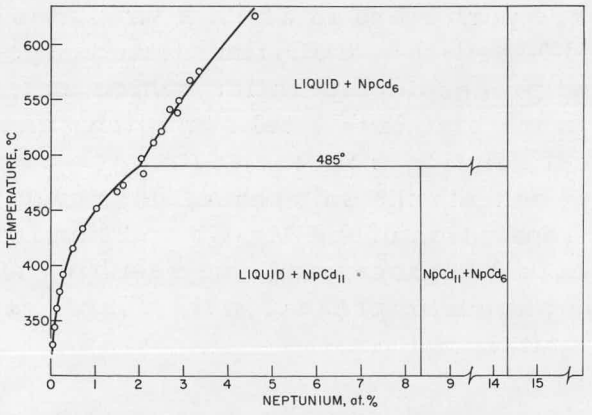


Fig. I-5

Partial Phase Diagram of the Cd-Np System.

The thermodynamic properties of the two intermetallic compounds mentioned above have been determined from high-temperature galvanic cells of the form

$$Np \,|\, NpCl_3,\ KCl\text{-}LiCl\ (eutectic) \,|\, Np\text{-}Cd\ (2\text{-phase alloy})$$

The cells were operated over a temperature range from 393 to 577°C. When the emf data were plotted vs the temperature, the data could be best represented by two straight lines intersecting at 484.8 ± 0.3°C. The temperature of the intersection corresponds to the incongruent melting point of $NpCd_{11}$ and is in excellent agreement with the results obtained from the solubility study. The following equations were derived from the emf and solubility data for the temperature dependence of the standard free energy of formation:

$$NpCd_{11}: \quad \Delta Gf^\circ\ (cal/mol) = -42{,}400 + 39.21T$$

$$NpCd_6: \quad \Delta Gf^\circ\ (cal/mol) = -29{,}130 + 21.88T$$

where T is °K. The enthalpy of formation of $NpCd_{11}$ (-42,400 cal/mol) is closer to that found for $PuCd_{11}$ (-45,900 cal/mol) than that for $UCd_{11}$ (-27,200 cal/mol). The entropy of formation of $NpCd_{11}$ is about 3 cal/(deg)(mol) more positive than the values for $PuCd_{11}$ and $UCd_{11}$, both of which are about 36 cal/(deg)(mol). These results show that the thermodynamic properties of metallic neptunium systems are similar to those of plutonium systems.

## C. Engineering-Scale Process Investigations

### 1. Process Flowsheet Experiments

#### a. Fuel Decladding and Feed Preparation

An experimental program was initiated to study the removal of stainless steel cladding from oxide fuels by dissolution in molten zinc and the subsequent interfacing of this process operation with the reduction step.

Two experiments were performed in which a simulated stainless steel fuel assembly loaded with $UO_2$ pellets and $UO_2$ fines (crushed pellets) was subjected to a complete head-end processing operation, which included the following steps: (1) dissolution of the stainless steel in molten zinc, (2) transfer of the zinc-stainless steel solution from the system, (3) vacuum distillation of the residual zinc (from beneath the salt phase), (4) reduction of the $UO_2$ pellets and fines, and (5) separation of the Mg-Cu solution from the precipitated uranium phase. In actual reprocessing, the resulting Mg-Cu solution would contain the bulk of the plutonium present in the charge, and would be the feed for the extraction unit.

The simulated fuel assemblies (see Fig. I-6) used in the runs were constructed of type 304 stainless steel, and consisted of an array of 13 tubes welded to three circular plates. The tubes were about $12\frac{1}{2}$ in. long, with a 3/8-in. ID, and a wall thickness of 0.035 in. The plates were 4 in. in diameter and 1/4 in. thick. Each of the assemblies contained 2.7 kg of stainless steel and 2.5 kg of $UO_2$, ~5% of which was fines.

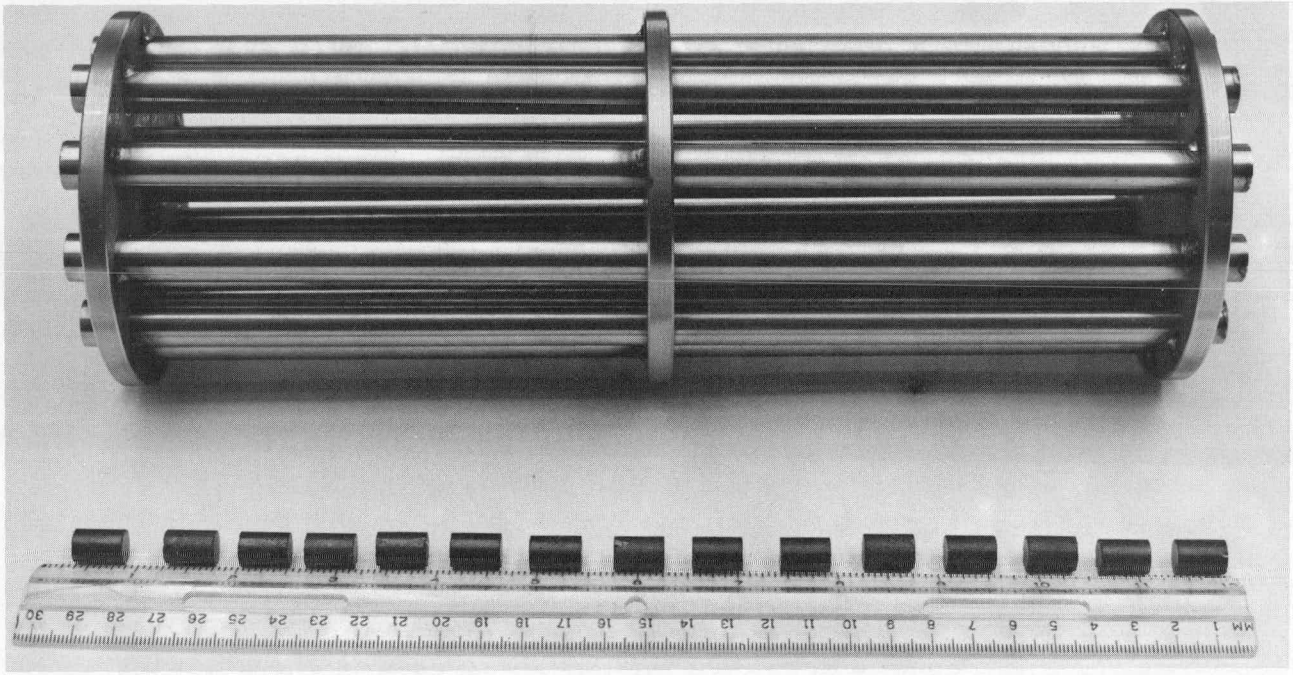

Fig. I-6. Simulated Stainless Steel Fuel Assembly Used in Process Head-End Experiments.

The decladding experiments were conducted in a $9\frac{3}{8}$-in. ID by 20-in. high pressed-and-sintered tungsten crucible. About 84.5 kg of zinc was added to the crucible to provide a liquid metal depth of 14 in. Six kg of $CaCl_2$-20 mol % $CaF_2$ (about 2 in.) was charged to the crucible to retard vaporization of the zinc and to collect $UO_2$ fines. The system was then heated to 800°C and the assembly was completely submerged in the melt. Filtered samples of the zinc-stainless steel solution were taken to ascertain the rate of dissolution in both runs. The results indicate that the tubing

was dissolved in less than 30 min, but the more massive spacer plates required about 4 hr for dissolution.

In each run, most of the zinc-stainless steel solution was removed through a transfer line at the conclusion of the decladding step. The zinc-stainless steel ingots were subsequently dissolved in nitric acid. Analyses of the acid solution showed that the ingots contained very little entrained $UO_2$.

After the bulk of the zinc-stainless steel solution had been transferred from the crucible, a water-cooled condenser was connected to the furnace vessel through the same opening used for the transfer line. The condenser provided for gas flow up out of the furnace and into the vacuum system. The gas flowed through a horizontal section of a steel tube having internal flow baffles and external cooling coils. When the system was evacuated through the condenser, zinc vapors passed through the 2-in. salt layer to the condenser. The crucible contents were maintained at about 800°C throughout the vaporization step.

About 2.3 kg and 4.0 kg of zinc were collected in the two runs. At the distillation rates employed, without any provision for de-entrainment, some salt was entrained, but uranium entrainment was low (<0.1% of the uranium).

Following the zinc distillation step in the two runs, the $UO_2$ was reduced with Mg-42 at. % Cu-3 at. % Ca. More than 99% of the oxide charged was reduced in each experiment.

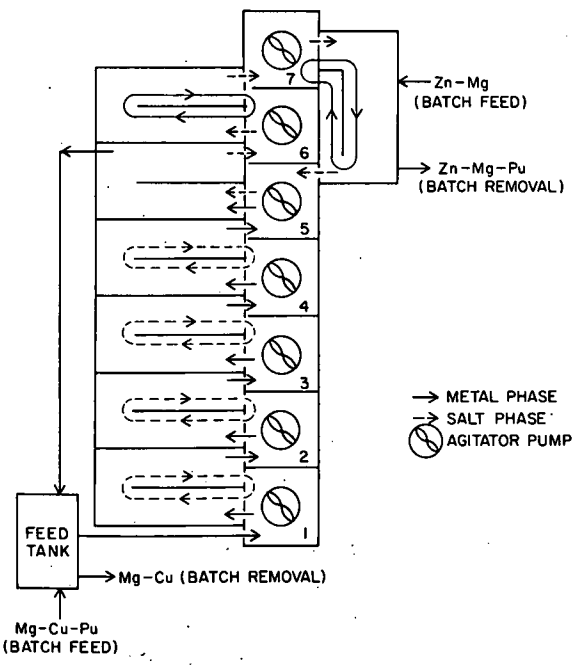


Fig. I-7. Flow Pattern in Seven-Stage Mixer-Settler.

b. Mixer-Settler Investigation

The salt transport process (see Fig. I-1) incorporates a multistage, semicontinuous extraction battery for separation of fission products from plutonium. Unlike conventional multistage mixer-settlers, which employ countercurrent flow of two fluids, several different fluids and several semi-independent flow patterns are used in the proposed mixer-settler battery. The flow patterns for the unit are illustrated in Fig. I-7 which is a plan view of a seven-stage extractor. An agitator-pump located in the mixing chamber of each mixer-settler stage mixes the fluids by means of blades attached to the outside of the rotor and pumps them by

centrifugal force up from an opening in the bottom of the rotor to discharge outlets at the top (see Fig. I-8). A portion of the material discharged from the pump may be refluxed to the mixing chamber; the balance is diverted into a settling chamber. All stages but one, stage 5, operate with either the salt or metal phase as a captive phase. The captive phase flows around a vertical partition in the settling chamber and back into the mixing chamber.

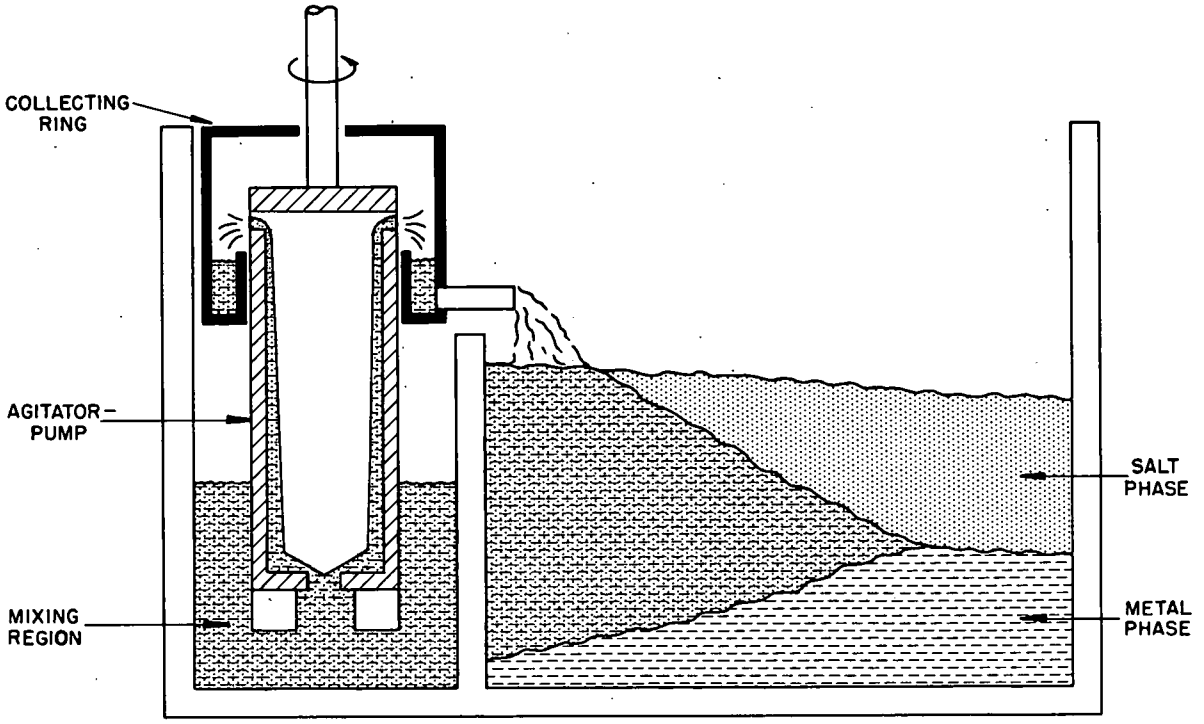


Fig. I-8. Mixer-Settler with Agitator-Pump.

As stated earlier, Mg-Cu-Pu alloy containing fission products is circulated from a feed tank through stages 1 to 4 to extract rare earth fission products from the solution into a captive molten salt phase. In stage 5, plutonium is selectively stripped into the transport salt. The depleted liquid metal (containing most of the nobler elements) is temporarily held up in a retention tank and is then recirculated to stage 1 to strip residual plutonium from the captive salt. In stage 6, the plutonium-bearing salt stream is contacted with a captive Mg-Cd phase to scrub the transport salt for additional removal of nobler elements and traces of Mg-Cu that may be entrained occasionally from stage 5. In stage 7, plutonium is stripped from the continuously recirculated transport salt into a captive Zn-Mg acceptor solution. The acceptor alloy is transferred intermittently to the distillation unit for plutonium recovery and is replaced with recycled Zn-Mg condensate. When the plutonium concentration in the salt in stage 1 has been reduced to an acceptable level, the salt and metal flows are stopped and the salt in stage 1 is sent to waste. The salts in stages 2, 3, and 4 are sent to stages 1, 2, and 3, respectively, and

fresh salt is charged to stage 4. The Mg-Cu solution is recycled to the decladding vessel. The levels of the nobler metals and copper in stage 6 are expected to be sufficiently low to permit reuse of the captive Mg-Cd alloy for several cycles. The transport salt is not consumed or contaminated in this process and may be reused indefinitely.

Full-scale plastic models of a mixer-settler stage have been built and tested. Water and an organic liquid (1 part acetylene tetrabromide and 0.43 parts xylene) were used in these models as light and heavy phases, respectively. These fluids were selected because the ratio of the difference in density of the light and heavy phases to the density of the ligher phase is the same as that of the Mg-Cu and salt system of the reference flowsheet. Fluid flow characteristics for this water-organic system have been determined, and should be similar to the characteristics of the Mg-Cu/salt system to be used.[19]

A furnace has been modified to permit testing of a mixer-settler unit at 650°C with Mg-Cu and salt phases. Pumping characteristics of the rotor have been established and conform closely to predicted values based upon the results of the tests with the water-organic system. Further testing will be done to obtain data on stage efficiencies.

2. Plutonium Salt Transport Facility

Preliminary bench-scale studies of the salt transport process were performed in a small walk-in-hood facility containing two heated furnaces, and were limited to batch studies with a maximum inventory of 200 g of plutonium. A new glovebox facility (called the Plutonium Salt Transport Facility) is being constructed that will contain process equipment capable of demonstrating all of the steps in the pyrochemical process flowsheet with an expected fission product decontamination factor of $>10^6$ and plutonium and uranium recoveries exceeding 99%. The equipment will be sized to handle a process charge of 5-10 kg of fuel containing as much as 1 kg of plutonium, and will incorporate semicontinuous mixer-settler extraction and solvent metal distillation units. The facility will be able to handle simulated stainless steel fuel assemblies containing $(U, Pu)O_2$ pellets and inactive fission product elements.

Figure I-9 is a sketch of the facility that is being constructed. Purified helium atmospheres will be used in the glovebox containing the extraction and retorting equipment and the glovebox for decladding, reduction, and uranium recovery equipment. The two boxes are equipped with cooling systems for removing the heat lost from the various processing vessels. Movable trays that can support cantilevered loads are located in each lock and passthrough, and motorized cranes are provided for materials handling within the gloveboxes.

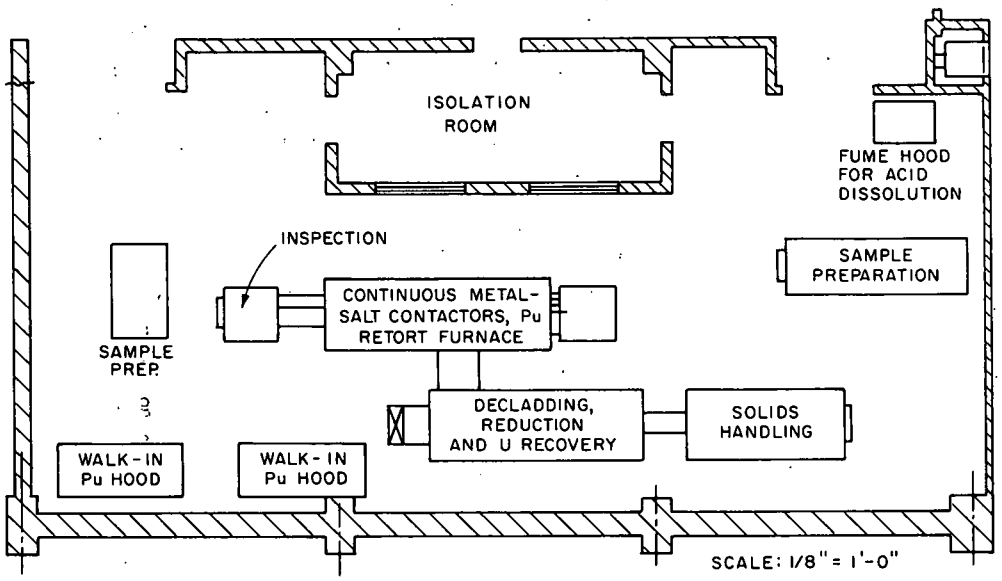


Fig. I-9. Plutonium Salt Transport Facility.

Processing equipment for the decladding, reduction, and uranium recovery box has been designed and is being fabricated; decladding and reduction demonstrations in this glovebox are expected to begin in mid-1969. Extraction equipment for use in the other box is still being developed and is expected to be installed and ready for use early in 1970.

At present, all of the boxes are in position, interconnections have been installed, and service piping installation is progressing.

### 3. Large-Scale Mixer-Settlers

A facility to test mixer-settler components and to evaluate various design concepts under typical processing conditions was installed in the large inert-atmosphere enclosure in Building 310. The equipment consists of a loop containing a centrifugal pump, a constant-head tank, two mixer-settlers, a weigh tank, and a sump tank. The purposes of the initial experiments are to demonstrate the transport of uranium through a salt phase and to determine if there is any entrainment of the liquid metal in the salt.

Two runs have been performed in which uranium was transported by circulating a molten salt from a Cd-2.5 at. % Mg alloy in one mixer-settler to a Cd-48 at. % Mg alloy in the other mixer-settler. In the first run circulation was terminated after only 0.5 hr because of mechanical difficulties. In this period of time 0.8 kg of uranium was transported. The average salt flow rate was 1.5 kg/min.

The second run was successfully completed. Salt was circulated for 5 hr at 4.5 kg/min. Preliminary results indicate a uranium transport rate of 72 g/min in the early part of the run. This is close to the maximum predicted rate.

4. Countercurrent Columns

The behavior of liquid metal-salt systems in packed columns is being studied. A Cd-Mg-Ce metal phase and a molten chloride salt phase were used in a high-temperature column to demonstrate countercurrent contacting and to measure mass transfer rates between the metal and salt phases. A metal-water system that simulated the physical properties of metal-salt systems was used in a low-temperature column to measure the hydraulic behavior of packed columns.

One run was made in the high-temperature column in which the composition of the metal used was Cd-17 at. % Mg-0.35 at. % Ce and the salt was $MgCl_2$-30 mol % NaCl-20 mol % KCl. The metal flow rate was 790 g/min, and the salt flow rate was 670 g/min. The packed section of the column was 1.05 in. in ID by 33 in. long, and the packing was 1/4-in. Raschig rings. The operating temperature of the column was 520°C. During the first 20 min of countercurrent flow, the pressure drop across the column fluctuated, indicating that the column was operating with incipient flooding. The number of theoretical stages was 0.8, and the height of a transfer unit (based on the metal phase) was 44 in. during the operating period. The rather low extraction rate, compared with that in earlier runs, may have resulted from the near-flooding conditions. After about 20 min the column flooded.

The high-temperature column has been dismantled and moved to Building 310 where it will be reassembled for future experimentation. All of the work performed to date indicates that packed columns can be used in pryochemical processes for nuclear fuel recovery.

Measurements of pressure drop, limiting flow rates, and hold-up have been made using Wood's metal and water in the low-temperature column. The packed section of the column was 1.05 in. in ID by 24 in. long, and the packing used was either 3/16-in. metal saddles or 1/4-in. metal Raschig rings. The pressure drop of the continuous aqueous phase was correlated with an equation for pressure drop through a porous medium. The effect of the discontinuous metal phase on the pressure drop could be accounted for by assuming that the column void fraction varied with the metal flow rate to the -0.4 power. At high water rates, near the flooding point, the effective column void fraction became a function of water rate as well as metal rate. This effect is believed to be caused by the onset of turbulence in the metal phase, which dissipates a large amount of energy. The turbulence of the metal phase was also found to influence limiting flow rates. The effects of discontinuous phase turbulence on the behavior of packed columns have not been observed with water-organic systems because countercurrent columns usually flood before the discontinuous phase becomes turbulent.

## D. Pyrochemical Purification of Plutonium-238

A new program was initiated on the development of a pyrochemical process for preparing high-purity $^{238}Pu$ metal from impure $^{238}PuO_2$ feed material. This program is primarily directed toward the recovery and purification of $^{238}Pu$ in the oxide scrap that results from the production of $^{238}PuO_2$ microspheres that are used as fuel in isotopic power sources.

The Plutonium-238 Facility, shown schematically in Fig. I-10, was constructed for the development work. The facility consists of two gloveboxes. The larger unit (Glovebox A), which is designed for the pyrochemical work, has a 343-$ft^3$ helium-atmosphere section and an 86-$ft^3$ air-atmosphere section. This glovebox is connected by a transfer tunnel to a second unit (Glovebox B), a 258-$ft^3$ air-atmosphere unit for analytical and other aqueous work. The two gloveboxes are shown in Fig. I-11. The process equipment in this facility was tested with liquid

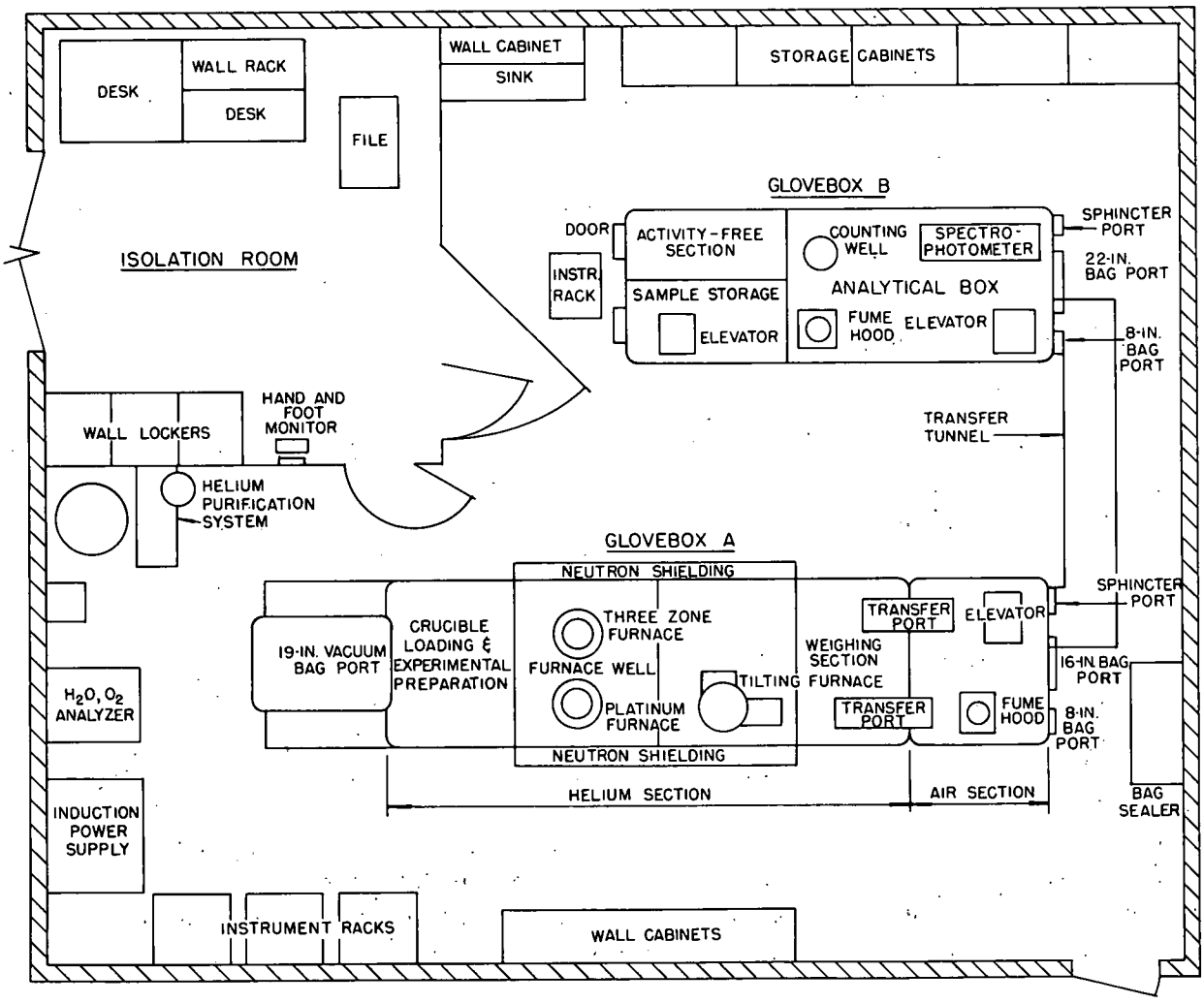


Fig. I-10. Diagram of Plutonium-238 Research and Development Facility.

metal and salt solvents to ensure that all of the sampling and handling operations could be performed safely. Experimental work with plutonium-238 was started in this facility late in 1968.

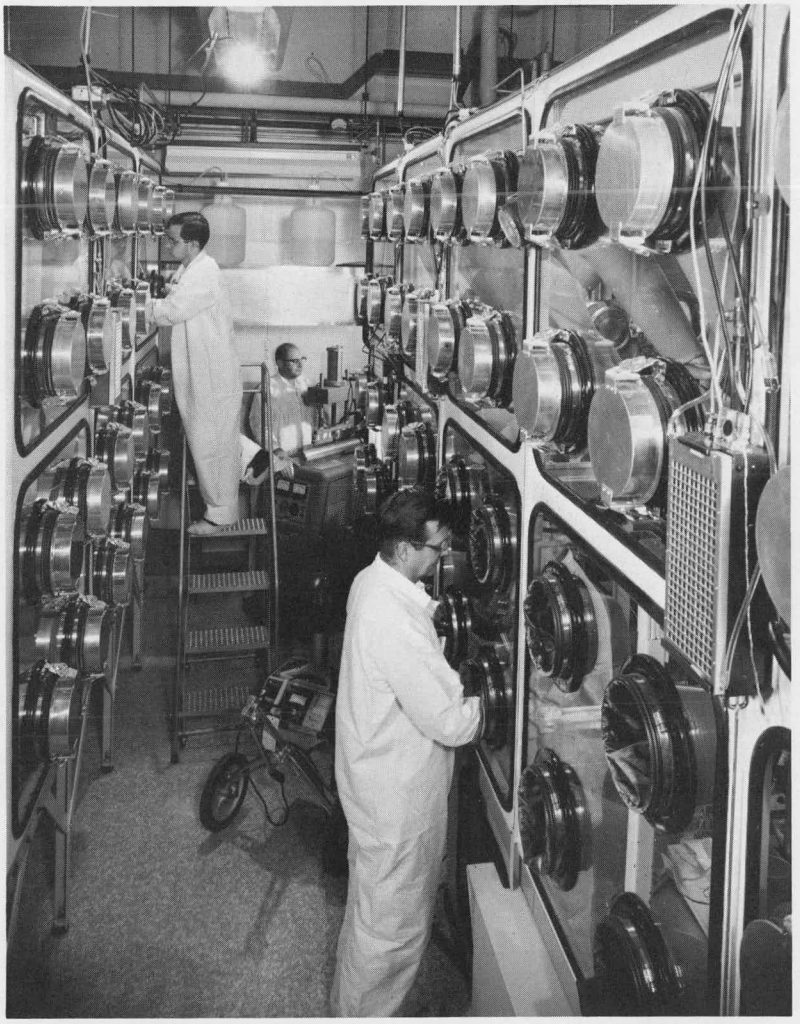

Fig. I-11. Gloveboxes in the Plutonium-238 Facility.

The proposed process for recovery of $^{238}Pu$ from $^{238}PuO_2$ scrap consists of three steps: (1) reduction of the $^{238}PuO_2$ microspheres by a reduction-donor alloy (e.g., Mg-Cd) in the presence of a molten chloride salt, (2) transport of the plutonium away from the impurities by cycling the salt between the reduction-donor alloy and an acceptor alloy with a higher affinity for plutonium (e.g., Mg-Zn), and (3) retorting the acceptor alloy to recover the plutonium metal product. The first experiments with $^{238}Pu$ involve only the reduction and retorting steps. Later experiments will include the salt transport step.

While final preparations were being made for experiments with $^{238}Pu$, two runs were performed with $^{239}PuO_2$ microspheres obtained from

Battelle Memorial Institute. In these runs, the three steps of the process were demonstrated with 10-g charges of the $^{239}PuO_2$. The reduction and salt transport steps were conducted in an induction-heated, tilt-pour furnace containing a two-compartment tantalum crucible. The reduction was carried out in one compartment of the crucible at 725°C for 3 hr with continuous agitation. The salt transport step was then performed by tilting the crucible back and forth to contact the salt alternately with the donor and acceptor alloys. After ten such cycles had been completed, plutonium metal was recovered from the acceptor alloy by vacuum retorting. The salt and metal phases were sampled after the reduction, and both phases in each compartment of the crucible were sampled after the ten salt transport cycles.

Within the accuracy of the sampling and analytical procedures, the plutonium accountability for each of these runs was 100%. Spark-source mass-spectrographic analyses of the $^{239}PuO_2$ feed material and of the $^{239}Pu$ products indicated that the removal of light-element impurities was quite successful. Except for oxygen (100 ppm in the product), a total of only 20 ppm of elements having a lower atomic weight than aluminum was present in the products. This result is especially encouraging, since the presence of these elements results in $(\alpha,n)$ reactions that increase the radiation hazard associated with plutonium-238. However, the overall purity of the $^{239}Pu$ product was only a factor of two or three better than that of the feed material because (1) the feed material itself was quite pure and (2) small amounts of impurities were present in the process solvents. Process solvents of higher purity are being used in runs that are now being carried out.

# II. FLUORIDE VOLATILITY PROCESS

The objective of the fluoride volatility program is to develop technical data that will permit appraisal of the potential of fluoride volatility for reprocessing FBR fuels. The basis for the fluoride volatility processing method is the reaction of fluorinating agents with fuel materials in fluid-bed systems to produce the volatile hexafluorides of uranium and plutonium, which are separable from nonvolatile fission product compounds. Since volatile fluorides of certain fission product elements accompany $UF_6$ and $PuF_6$, additional separation procedures are necessary to produce purified products.

A major effort during the past reporting period consisted of conceptual design studies of a large fluoride volatility plant for processing FBR fuels. The reference flowsheet was designed on the basis of knowledge developed in earlier work with light water reactor (LWR) fuels. The reference fuel is $UO_2$-$PuO_2$ clad in stainless steel. The process involves the following steps: (1) separation of cladding from the fuel, (2) fluorination in a fluid-bed reactor with dilute fluorine at low temperature to produce $UF_6$, (3) fluorination in a second fluid-bed reactor with concentrated fluorine at high temperature to produce $PuF_6$, (4) separation and purification of $PuF_6$ by thermal decomposition to nonvolatile $PuF_4$, (5) purification of the $UF_6$ by distillation and sorption techniques, and (6) mixing of $UF_6$ and $PuF_6$ in the desired proportions and conversion to homogeneous $UO_2$-$PuO_2$ material by simultaneous reaction with steam and hydrogen. The objectives of the current effort are to present the current technological basis for a large fluoride volatility plant in the form of process and engineering flowsheets and to define process uncertainties (problem areas).

The experimental process development effort includes an investigation with a 2-in. dia fluid-bed reactor to establish optimum processing conditions for fluorinating simulated spent FBR fuel. The effect of (1) fuel-to-alumina ratio, (2) fluorination temperature, and (3) duration of fluorination on the plutonium concentration in the final alumina bed was studied.

Four supporting studies are reported: studies of the reaction of $NpF_6$ with NaF, the sorption of ruthenium fluorides on a bed of particulate LiF, the identification of ruthenium fluoride species by sublimation of mixtures of $UF_6$ and ruthenium fluorides, and the filtration of $PuO_2F_2$ aerosol by fiber filters. Basic backup investigations were also performed--studies of the fluid dynamics of bubbles in a fluidized bed and of pulsed-gas contacting of gases and solids.

## A. Conceptual Process for Fast Breeder Reactor Fuels

An objective of the Liquid Metal Fast Breeder Reactor Program[1] is the development of an economically feasible nuclear fuel cycle. Recovery

[1] "Liquid Metal Fast Breeder Reactor Program Plan," USAEC report, ten sections numbered WASH-1101 through WASH-1110 (August 1968).

processes for FBR fuels represent a critical part of the fuel cycle because of the high value of the plutonium in discharged fuel, the need for short turnaround time to minimize fuel-inventory charges, and the handling difficulties associated with the high radioactivity level of high-burnup FBR fuel.

In its current assignment to assess the applicability of fluoride volatility processes to FBR fuels, the Fluoride Volatility Section is making conceptual design studies of a large central plant serving nuclear power plants with a total capacity of 15,000 MW(e). The processing plant would provide a highly decontaminated product (decontamination factor of $10^6$-$10^7$) and an overall minimum recovery of 99% of the uranium and plutonium.

The capacity of the conceptual plant is one metric ton of actinides per day. Key fuel characteristics are the high plutonium content, the high fission product content, and the high heat loads. Recycle of the gaseous reagents is employed to conserve reagents and also to minimize the quantity of effluent gas that must be treated. To eliminate the release of noxious materials to the environment, the design concept includes treatment of the main process off-gas such that there is virtually total containment.

The objectives of this study are to present the current technological basis for such a plant in the form of process and engineering flowsheets and to define process uncertainties. The uncertainties will be translated into key problem areas from which a research and development program will be developed.

Process and engineering flowsheets have been prepared, as well as (1) basic layouts of the process cell and the overall plant and (2) preliminary design of major equipment items. Major design features are continuous fluid-bed fluorinators and (for nuclear criticality safety and satisfactory heat removal) slab geometry of vessels containing significant quantities of plutonium. A simplified version of the conceptual flowsheet is shown in Fig. II-1.

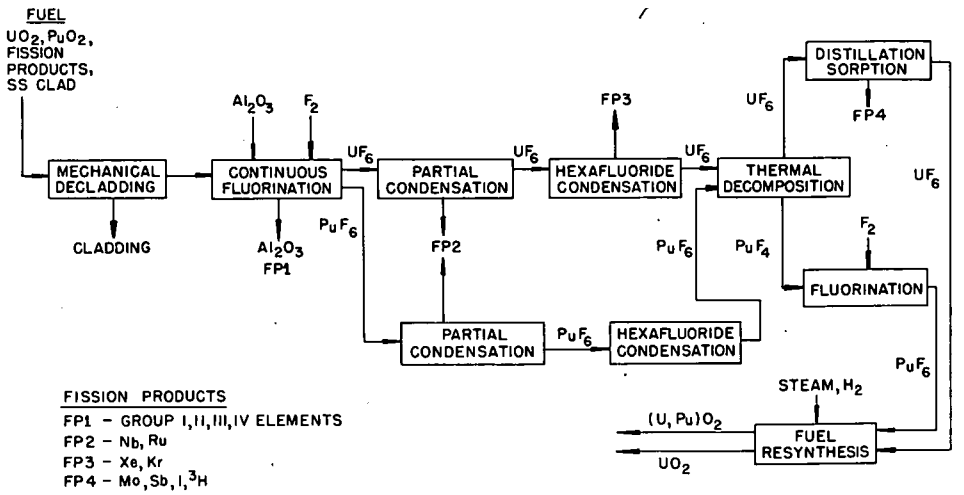


Fig. II-1. Fluoride Volatility Process for Fast Breeder Reactor Fuels.

The mechanical head-end scheme[2] includes mechanical disassembly of the fuel elements, chopping of the fuel pins, and a step to separate the cladding and convert the oxide to a powder. The powdered fuel oxide is next fed along with particulate alumina to the first of two in-series fluid-bed fluorination units, which provide bulk separation of the uranium and plutonium as well as partial decontamination. The bulk of the uranium is removed as volatile $UF_6$ from the first reactor, and the bulk of the plutonium is removed as volatile $PuF_6$ from the second reactor (a two-stage unit). Continuous operation and staging without the use of downcomer pipes appears feasible on the basis of recent exploratory studies.

Fluorine is the only fluorinating agent used in the present process. Fluorination at 350°C with ~20% fluorine-oxygen in the first reactor converts the bulk of the uranium to $UF_6$ and less than 5% of the plutonium to $PuF_6$. The $UF_6$ production rate is approximately 100 lb/(hr)(ft$^2$). During fluorination with ~90% fluorine at 500°C and 550°C in the upper and lower stages of the second reactor, the $PuF_6$ production rate is 13 lb/(hr)(ft$^2$).

The alumina stream, which cascades through the fluorination reactors and finally to waste receivers, represents the main solid waste stream, providing a vehicle for the disposal of those fission products in the feed that do not form volatile fluorides.

The gas streams from each of the two fluid-bed fluorination units pass through a fission product trap (partial condenser) and a hexafluoride-collection cold trap, where separation from some fission products occurs. The $UF_6$ product stream may contain sufficient plutonium to warrant recovery of $PuF_6$ from this stream. This is accomplished in the present flowsheet by recombining the hexafluoride product streams and carrying out a more nearly quantitative separation in a fluid-bed thermal decomposition step,[3] where $PuF_6$ is converted to solid $PuF_4$. This step also gives further purification of the plutonium from remaining volatile fission products. The $UF_6$ stream passes overhead and is purified by a combination of fractional distillation and sorption traps.

The $PuF_4$ produced by thermal decomposition is subsequently refluorinated to $PuF_6$ with concentrated fluorine (~100%) at 500°C and combined with the desired proportion of pure $UF_6$. The mixture is fed to a fluid-bed converter, where a dense homogeneous $PuO_2$-$UO_2$ particulate solid is produced by simultaneous reaction of the hexafluorides with steam and

---

[2] Portions of this head-end process are under development at ORNL and are described in the "Chemical Technology Division Annual Progress Report for Period Ending May 31, 1968," ORNL-4272 (September 1968).

[3] L. E. Trevorrow, M. J. Steindler, "Laboratory Investigations in Support of Fluid-Bed Fluoride Volatility Processes. Part XV. Estimation of Rates of Thermal Decomposition of Plutonium Hexafluoride in Process Streams," USAEC report ANL-7347 (July 1967).

hydrogen. The conversion process is based on work conducted earlier on $UF_6$ alone.[4] Excess $UF_6$ may be converted to the oxide for use in other reactors.

Overall plant problems such as criticality, accountability, and plant safety in the event of hexafluoride release have been considered in this preliminary evaluation. Accountability and burnup analyses are accomplished by weighing, sampling, and analyzing (1) fuel before it is fed into the first chemical process stage, (2) the final products, and (3) final waste streams (which establish loss levels). The approach to criticality control adopted for this volatility-plant concept is one that avoids neutron moderation and minimizes neutron reflection to obtain a low reactivity per unit mass of plutonium in the process system. Also, all vessels expected to contain significant quantities of plutonium are of a slab design, which lends itself to safe-by-shape geometry.

A preliminary analysis of nuclear safety has been made, with attention focused on the uranium fluorination reactor, which represents the point of largest accumulation of fissile material and hence presents the most stringent requirements for nuclear criticality safety. In the safety analysis, plutonium inventory of the reactors, plutonium density, the amount of internal and external reflection involved in containment, and normal and abnormal operating conditions were considered. For both normal and credibly abnormal situations, an acceptable factor of safety is predicted.

Study of the conceptual process indicated that additional work is required to gain added information in the following areas: the mechanical head-end step, continuous fluorination of uranium and plutonium with acceptably low losses, fission product behavior, hexafluoride-to-oxide conversion, and total containment of wastes. Successful demonstration of the flowsheet appears promising on the basis of current technology.

## B. Fluorination of Simulated FBR Fuels in a 2-in. Dia Fluid-Bed Reactor

A 2-in. dia fluid-bed reactor is being used to study the fluorination of powdered uranium-plutonium dioxide from simulated FBR fuels. This oxide, together with a mixture of nonradioactive fission product oxides, was proportioned to simulate FBR core fuel with a burnup of 100,000 MWd/metric ton.

In these laboratory-scale studies, the fuel is first oxidized with oxygen to $U_3O_8$-$PuO_2$ fines. Uranium is then fluorinated to the volatile hexafluoride with 10 vol % fluorine, and plutonium is subsequently fluorinated

[4] I. E. Knudsen, N. M. Levitz, A. A. Jonke, "Engineering Development of Fluid-Bed Fluoride Volatility Processes. Part 6. Preparation of Dense Uranium Dioxide Particles from Uranium Hexafluoride in a Fluidized Bed," USAEC report ANL-6902 (December 1964).

(recycle-fluorination) with concentrated fluorine at temperatures of 300 to 550°C or 450 to 550°C.

The initial scoping experiments with FBR fuel consisted of a fractional factorial set of five experiments. The set was designed to determine the effects on plutonium concentration in the final fluidized bed for two levels of fuel-to-alumina ratio (0.3 and 0.6), two fluorination temperatures with 10 vol % fluorine (350 and 450°C), and two recycle-fluorination times (10 and 20 hr).

An acceptable plutonium concentration in the final bed is considered to be 1% or less of the initial charge of plutonium. For the five experiments, the fraction of plutonium charged remaining in the final bed ranged from 0.51 to 3.19%. In only one experiment was the plutonium concentration (3.19%) significantly above the acceptance criterion of 1%.

The conclusions drawn from the statistical analysis showed that an increase in the fuel-to-alumina ratio from 0.3 to 0.6 and an increase in the temperature of fluorination with dilute fluorine from 350 to 450°C will increase the fraction of plutonium charge remaining in the final bed; increasing the recycle-fluorination time from 10 hr to 20 hr will reduce the fraction of plutonium charge remaining in the bed.

Another finding in this investigation is that much of the uranium can be volatilized without appreciable volatilization of the plutonium. This was indicated by the results of analyses of the NaF product traps that collected $UF_6$ and $PuF_6$ products during fluorination with dilute fluorine. Uranium-to-plutonium ratios in the product for the first hour of this step ranged as high as 5000, and since the uranium-to-plutonium ratio in the charged fuel was 3.96, it is concluded that a separation factor for plutonium from uranium of about $10^3$ can be obtained by a suitable choice of operating conditions.

## C. Supporting Chemistry Investigations

### 1. Reaction of $NpF_6$ with NaF

In the fluid-bed fluoride volatility process, a possible step will be passage of a gas stream containing $UF_6$, $NpF_6$, and other volatile fluorides through a bed of NaF pellets to fix neptunium preferentially. Neptunium will probably have an initial concentration in the $UF_6$ process stream of 100 ppm. The equation representing the reaction at 150 to 250°C of an excess of neptunium hexafluoride at 150 to 300 Torr with sodium fluoride is

$$3\ NaF(s) + NpF_6(g) \rightarrow 3NaF \cdot NpF_5(s) + 1/2\ F_2(g)$$

The partial pressures of fluorine and neptunium hexafluoride in equilibrium with the solid phase formed by this reaction were obtained by

measurements of total pressure and ultraviolet absorbance of the gas phase. At a fixed temperature (350°C) over a tenfold variation of fluorine pressure, the value of log ($p_{NpF_6}$) was found to depend linearly on log ($p_{F_2}$) with a proportionality coefficient of 0.49, comparable with the value of 1/2 expected for the above reaction. Equilibrium constants, $K_p = (p_{NpF_6})/(p_{F_2})^{1/2}$, for the reverse of the above reaction at 250 to 400°C were expressed by the equation

$$\log K_{p(atm^{1/2})} = -3.147 \times 10^3/T\ (°K) + 2.784$$

The percentage of initial $NpF_6$ removed at various NaF bed temperatures (250-409°C), $UF_6$ pressures (18-1330 Torr), and $NpF_6$ concentrations (10-100 ppm) was calculated. In general, the percentage of $NpF_6$ removed is calculated to increase as the initial concentration of $NpF_6$ increases and to increase as the temperature of the NaF bed decreases. The pertinent process pressure for $UF_6$ in the reference flowsheet is 1330 Torr; at this pressure, the NaF bed must be kept above 409°C to avoid formation of $2NaF \cdot UF_6$. At the indicated concentration of $NpF_6$, pressure of $UF_6$, and temperature, a maximum of 46% of the initial neptunium should be removed with NaF in one equilibrium stage and a maximum of 70% in two stages.

2. Ruthenium Fluoride Chemistry

Volatile ruthenium fluoride, formed along with plutonium hexafluoride in the fluoride volatility processing of reactor fuel materials, is one of the contaminants that must be removed in purifying $PuF_6$. As part of the $PuF_6$ purification work, the absorption of ruthenium fluoride by LiF and other absorbents (NaF, nickel wool, $NiF_2$) has been studied. This work had two major goals: the first was to determine the ruthenium fluoride species formed in the fluorination reaction, and the second was to determine the sorptive capacity of LiF and other absorbents for ruthenium fluoride. The question of the ruthenium fluoride species formed during fluorination is important to prediction of the distribution of ruthenium in the fluid-bed fluoride volatility process. If the ruthenium fluoride species formed does not volatilize at 0°C, separation of plutonium from ruthenium can be effected by condensing the mixture of $PuF_6$ and ruthenium fluoride in a cold trap, then recovering the $PuF_6$ by transpiration at 0°C.

The procedure consisted of preparing a mixture of $UF_6$ (a stand-in for $PuF_6$) and ruthenium fluoride by the fluorination of a solid mixture containing $UF_4$ and either ruthenium metal or $RuO_2$, condensing the mixture in a cold trap (the product U-trap) at -78°C, then transpiring the mixture by raising the cold trap temperature in steps to 0, 50, 100, and 150°C while sweeping with fluorine into a series of traps containing the several absorbents held at fixed temperatures.

The results led to the following general conclusions:

1) No ruthenium fluoride other than $RuF_5$ was produced by the fluorination of the $UF_4$-ruthenium metal or $UF_4$-$RuO_2$ mixture. This was indicated by the absence of significant transport of ruthenium during the periods when the cold trap was at -78, 0, or 50°C since other species such as $RuF_6$ and $RuOF_4$ show appreciable volatility at 0 or 50°C.

2) Transpiration of plutonium at 0°C would result in a decontamination factor from ruthenium greater than $10^4$ if ruthenium behavior in such a system parallels that observed with $UF_4$-Ru.

3) The ruthenium sorption capacity of LiF at 350°C was about 23 mg Ru/g LiF, in comparison with the ruthenium sorption capacity of NaF at 100°C of about 22 mg Ru/g NaF. Ruthenium is not retained by lithium fluoride to its total absorption capacity; rather, ruthenium was observed to break through the trap at a point where about 70-80% of the absorption capacity had been reached. In contrast, NaF can be used as an absolute trapping agent for ruthenium, since ruthenium does not break through the NaF before its capacity is reached.

4) Nickel fluoride at 300°C was shown to be a poor absorbent for ruthenium; nickel, in the form of fine strands, did not retain ruthenium at 150°C.

### 3. Fission Product Fluoride Chemistry

A proposed fluoride volatility process for $UO_2$-$PuO_2$ reactor fuel includes the removal of uranium by fluorination of powdered fuel oxide with 77% oxygen-23% fluorine at 350°C to form $UF_6$. The fission product compounds formed in this step must be identified and their volatilities determined so that methods of separation can be developed. Examination of the literature suggested that the volatile compounds $NbF_5$, $RuF_5$, $SbF_5$, $TeF_6$, $MoOF_4$, $TcOF_4$, $IOF_5$, and $XeF_4$ may form in this step.

An exploratory investigation was performed to determine qualitatively the products formed when Nb, Mo, Ru, Sb, Te, $I_2$, Xe, $Nb_2O_5$, $MoO_3$, $RuO_2$, $Sb_2O_5$, and $TeO_2$ are individually reacted with oxygen-10% fluorine mixture at 350°C. Samples were reacted for ~1 hr in a vertical 1-in. dia, 9-in. long furnace, and the reaction gases were discharged through a series of traps including cold traps, activated alumina, and soda lime. The reaction products were tentatively identified by their volatilities (condensation temperatures), vapor pressures, and hydrolysis or reduction behavior. The major products of the reaction with Nb, Ru, Sb, $Sb_2O_5$, Te, and $TeO_2$ were $NbF_5$, $RuF_5$, $SbF_5$, and $TeF_6$. Molybdenum and xenon formed low-volatility fluorides, probably $MoOF_4$ and $XeF_4$. The volatility of the product of iodine-fluorine reaction was higher than those of $IF_5$ or $IF_7$, and thereby suggests

the formation of $IOF_5$. $Nb_2O_5$ showed no significant reaction; the reaction of $MoO_3$ apparently formed an oxyfluoride richer in oxygen than $MoOF_4$; the product of $RuO_2$ reaction was a volatile compound, apparently $RuO_4$.

## D. Basic Studies of Fluidized-Bed Behavior Related to Process Operations

### 1. Fluid Dynamics of Gas Bubbles in a Fluidized Bed

Information for the design and operation of fluidized-bed chemical reactors is largely empirical and is limited to the systems from which the data are derived. The complex character of particle and gas mixing in a fluidized bed is a result of gas bubbles that are formed when the fluidizing gas velocity is greater than the minimum fluidization velocity.

Recent theoretical work reported in the literature,[5-7] which applies to a single bubble and does not indicate the effect of interaction with other bubbles, has laid the foundation for understanding the fluid dynamics of a freely bubbling fluidized bed. A theoretical study was made in this Division to determine the interaction effects on particle movement and gas flow of bubbles in a chain rising through a fluidized bed in a "two-dimensional" column[8] and a conventional three-dimensional column. The effect of bubble spacing on particle mixing was studied, and the effects of (1) bubble spacing and (2) ratio of bubble velocity to minimum fluidization velocity on gas-solids contacting were also studied. Particle mixing was considered to be improved when passage of a bubble caused the length of particle trajectories to increase; gas-solids contacting was considered to be improved when the volume of gas cloud surrounding each bubble increased.

For the two-dimensional case, the area enclosed by the particle trajectories caused by the passage of one bubble in a chain of bubbles is approximately doubled when center-to-center bubble separation decreases from infinity to about 2.8 bubble radii. For the three-dimensional case, the volume enclosed by particle trajectories is approximately doubled as the center-to-center bubble separation decreases from infinity to 2.50 bubble radii.

For ratios of bubble velocity to minimum fluidization velocity (U) greater than one, a gas cloud (the gas in the particulate phase immediately surrounding the bubbles across whose boundary there is essentially no gas interchange) envelops the bubbles in both the two-and three-dimensional cases (see Fig. II-2). At high values of U and/or large bubble separations,

---

[5] J. F. Davidson, Trans. Inst. Chem. Eng. 39, 230 (1961).

[6] R. Jackson, Trans. Inst. Chem. Eng. 41, 13 (1963).

[7] J. D. Murray, J. Fluid Mech. 22, 57 (1965).

[8] A column of rectangular cross section for which the thickness is so small that a rising bubble is in simultaneous contact with two opposite walls.

an individual cloud surrounds each bubble. For low values of U and close bubble spacings, the gas clouds contact and gas flows from one bubble to another. The gas circulates from inside each bubble into the particulate phase and then back into the bubble, but also flows from one bubble into the bubble above (Fig. II-3).

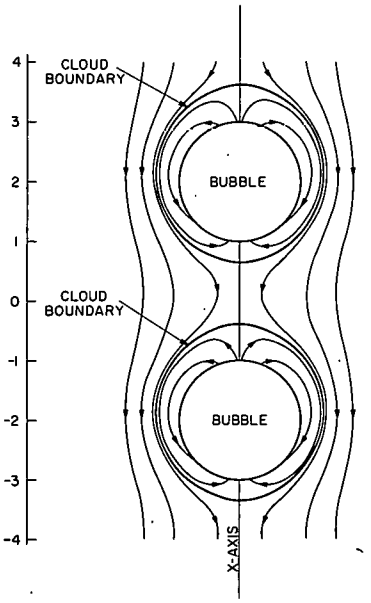


Fig. II-2

Fluid Dynamics of Gas Bubbles in a Fluidized Bed: Two-Dimensional Case. [Gas flow for U = 2.5 and a center-to-center bubble distance of 4 bubble radii; U = (bubble velocity)/(minimum fluidization velocity).]

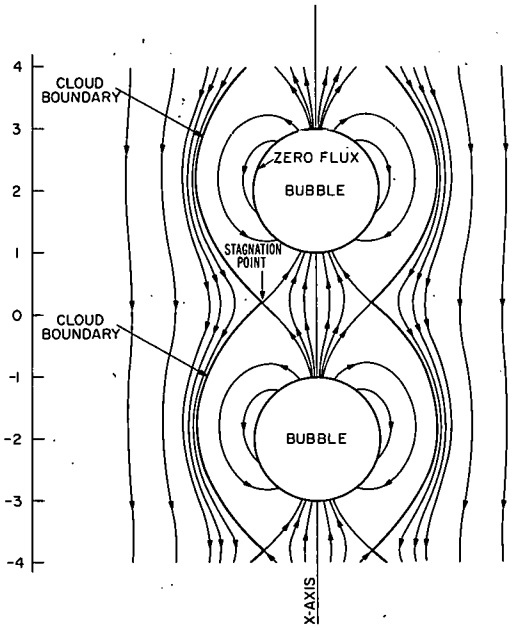


Fig. II-3

Fluid Dynamics of Gas Bubbles in a Fluidized Bed: Two-Dimensional Case. [Gas flow for U = 1.5 and a center-to-center bubble distance of 4 bubble radii; U = (bubble velocity)/(minimum fluidization velocity).]

For the two-dimensional case, when bubble centers are separated by a distance of 4 radii and U is greater than 1.2, the gas cloud is larger than for an isolated bubble, which results in greater gas contact with the particulate phase. For U less than 1.2, the area of the gas cloud per bubble in the chain is less than for a single bubble. However, for most cases of actual fluidization, U is greater than 1.2.

In the three-dimensional case for values of U greater than 1.4, the cloud volume per bubble decreases with increasing bubble separation. However, at the lower values of U, general trends are more complex. At U = 1.1, the cloud volumes for center-to-center bubble separations of 6.0 bubble radii and infinity (where the clouds are not contacting) are greater than for separations of 2.6 and 4.0 bubble radii (where the clouds are contacting). For all bubble separations studied, the cloud volume increases as U decreases from 1.4 to 1.1, but the rate of increase for contacting clouds is not as large as the rate of increase for separated clouds at the lower values of U.

The results of this theoretical study indicate that the gas flow patterns and particle paths determined by observations of a two-dimensional bed will be applicable to the three-dimensional systems in which the necessary observations cannot be readily made that are used in practical processing operations.

### 2. Pulsed-Gas Contacting Studies

Studies have been initiated on the use of pulsed beds for fluoride volatility processes as an alternative to conventional fluidized beds with steady upward flow of gas. In pulsed-bed operations, the bed expands during a pulse, then contracts during the interval when the gas flow is shut off. Possible advantages of pulsed-bed operation for a fluoride volatility process are (1) capability of using wider ranges of particle sizes, (2) better solids-gas contacting with large as well as small particles and improved reactant utilization, (3) improved heat and mass transfer rates, (4) greater mean rates of gas throughput and shorter fluorination periods, and (5) decreased elutriation of particles from the bed.

Exploratory tests were made with pulsed and fluidized beds with operating conditions and particle sizes similar to those used in the fluoride volatility process. An objective was to compare bed behavior for the two modes of operation.

Five sizes of granular alumina with particle sizes from 2380 to 2 $\mu$m were charged to a 3-in. dia, 72-in. long column in layers; the largest sized alumina was charged first, then the next smaller size, and so on. The fluidizing gas was air, and the gas velocity was 0.3 to 0.7 ft/sec. For the pulsed-gas runs, the pulse on-period was 0.36 to 0.5 sec, and the pulse frequency was 0.46 to 0.49 Hz.

Data were obtained on bed expansion and particle mixing in the bed for seven 6-hr runs with pulsed beds and three 6-hr runs with fluidized beds. At similar gas flow rates, bed expansion was consistently greater for pulsed beds than for fluidized beds. For pulsed beds, the bed-expansion ratio (maximum bed height/static bed height) appears to increase with increasing gas velocity, to decrease with increasing pulse frequency, and to decrease as the on-period fraction of the cycle is increased. In the pulsed-bed runs, the layers, which initially were completely segregated, mixed thoroughly within a few minutes of the start of the run and remained well mixed for the remainder of the operation. In the fluidized-bed runs, mixing occurred in the top layers, but the two lower layers remained stationary for the entire period.

## E. Penetration of Fiber Filters by $PuO_2F_2$ Aerosol

The toxicity and volatility of $PuF_6$ require that a very high degree of ventilation-air cleanup be provided in the event of an accidental release of

$PuF_6$ in an enclosure. Previous work (ANL-7175, pp. 85-87) indicates that, with a normal moisture concentration in the atmosphere of the enclosure, hydrolysis occurs within the gas phase to produce a fine aerosol ($PuO_2F_2$ particles of $\leq 0.1$ $\mu$m dia), but that, with low moisture concentrations, reaction occurs at solid surfaces exposed to the reactants.

An objective of the present series of experiments was to determine how gas-phase reaction and surface reaction affect filter penetration. Briefly, plutonium was removed from a gas stream by the combined process of (1) hydrolysis of $PuF_6$ in a gas mixer and (2) filtration of the resulting $PuO_2F_2$ aerosol through a series of pretested high-efficiency (AEC) filters. The quantity of plutonium on each filter was determined by analysis. Process conditions were (1) gas velocity at the filter surface of 0.25 to 2.5 cm/sec, (2) partial pressure of $H_2O$ of 0.3 to 5.3 Torr, (3) partial pressure of $PuF_6$ of 0.28 to 289 Torr, and (4) feed rate of from 1 to 300 mg Pu/hr.

A preliminary correlation of the results indicated that over the ranges studied, gas velocity has the greatest effect on filter penetration. The equation used to fit the results was

$$P = e^{cv^n}$$

where P is the fraction of the released plutonium that penetrates the first filter and is collected on the following filters and v is the gas velocity at the filter surface. The constants c and n, determined by least squares fitting, are

$$c = -16.2 \pm 0.4$$

$$n = -0.09 \pm 0.03$$

The error limits are standard deviations and include the effects of other variables, which have not yet been separately determined.

The value of n in the above equation has some theoretical significance as to the mechanism of filtration. For a homogeneous aerosol collected in the filter by a purely diffusional mechanism, the value of n would be -1. On the basis of a previously reported experimental measurement[9] of surface reaction kinetics, a value of -1 would be obtained for n if filter penetration were controlled by surface reaction. A mechanism of interception alone would give n = 0. A mechanism of impaction alone would give n = 1.

Reaction of gaseous $PuF_6$ with moisture at the filter surface does not operate simultaneously with the other mechanisms. Since the smallest value

[9]R. W. Kessie, D. Ramaswami, "Removal of Plutonium Hexafluoride from Cell Exhaust Air by Hydrolysis and Filtration," USAEC report ANL-7066, pp. 43-47 (December 1965).

for n for all pairs of runs with any significant gas velocity difference is n = -0.25, surface reaction kinetics apparently did not control penetration in any of the runs.

The other mechanisms operate simultaneously on aerosol collection, with the interception mechanism predominating and the diffusion mechanism also effective to a smaller extent.

It has been observed that, in a series of two filters, the fraction of the incident plutonium aerosol penetrating the second filter is usually much greater than the fraction of plutonium aerosol penetrating the first filter. Filter penetration might be a result of electrostatic-charge effects, since ion pairs are generated in a $PuF_6$-air mixture by radiation from plutonium. To investigate this possibility, two runs were performed with an electrically charged aerosol collector installed in the chamber between the first and second filters. Of the total aerosol in the chamber, 96% was found to be neutral, 3.2 to 3.5% was positively charged, and 0.38 to 0.87% was negatively charged.

On the basis of these results, it is hypothesized that one of the mechanisms whereby high penetration of filters by charged aerosols may occur is as follows: collection on the walls of the equipment of a greater proportion of negative than positive ions, due to the larger diffusivity of negative ions, leaves the aerosol with a net positive charge. Gas convection drives the charged aerosol to the filter, which then becomes positively charged. Positive ions and positively charged aerosol particles now penetrate the filter more readily than do neutral or negatively charged particles.

The results of the two runs are consistent with this hypothesis--that is, >3% of the aerosol between the first and second filters was positively charged, and this is sufficient to account for the observed penetration (up to 1% of the incident aerosol) of the second filter. The above work tends to verify the apparently new concept that charge effects can increase aerosol penetration of filters.

# III. MATERIALS CHEMISTRY AND THERMODYNAMICS

## A. High Temperature Thermodynamic and Physical Property Studies

The objective of this program is to obtain phase-diagram, thermodynamic, and physical property data that can be used to interpret and evaluate the performance and safety of candidate fast-breeder reactor fuels. This information will aid in understanding and predicting (1) interactions among fuel, fission product, and cladding materials, (2) migration by diffusion or vapor transport of fissile atoms, anion atoms, and fission products, and (3) melting, flow, and pressure rise rates in core and structural materials associated with possible coolant failure or nuclear excursions. In addition, these data will help to identify phases formed in fuel under operating conditions and to choose cation additives for controlling the chemical potentials of the fuel anions.

### 1. Phase Diagram and Vapor Pressure Studies

High-temperature investigations of the U-Pu-O and U-Pu-C systems have been initiated. These investigations include mass spectrometric vapor pressure measurements, phase diagram studies, and activity measurements by transpiration. In the mass spectrometric study, both the Pu-O and Pu-C systems are being investigated before taking up the ternary systems. Phase diagram studies of the metal-rich end of the Pu-O system have begun. Carbon activities and uranium pressures over U-C are being obtained with a transpiration technique.

#### a. Volatilization Studies of Plutonium Compounds by Mass Spectrometry

Mass spectrometric studies of the volatilization of plutonium-containing materials are under way. Their purpose is to determine (1) the apparent composition of the vapor phase in equilibrium with the condensed phase(s), (2) the partial pressures of the vapor species as a function of temperature, and (3) the thermodynamic properties of the vapor species and condensed phases.

(1) Plutonium-Oxygen System. The first stage of the volatilization studies has been devoted to the plutonium-oxygen system, since mass spectrometric data for this system were not available. Studies relating to the apparently congruently vaporizing plutonia ($\sim PuO_{1.83}$ at 2175°K) and to the binary condensed phase $Pu_2O_3 + PuO_{1.61}$ have now been completed.

Because tungsten and rhenium were shown to react with oxygen-rich plutonia (ANL-7450, p. 40), the experiments were conducted with effusion cells of iridium, which were determined to be nonreactive. Partial

pressures of PuO and $PuO_2$ were obtained from measurements of the temperature dependency of vapor species and total effusion rates (see ANL-7445, p. 124). The composition of the vapor phase was determined from ion intensity ratios corrected for relative ion cross sections,[1] multiplier efficiencies, and the difference between the ionizing voltage and appearance potential[2] of each gas. The small amounts of oxygen and plutonium present in the vapor phase were not included in the calculations.

The partial pressures of PuO(g) and $PuO_2$(g) over $PuO_{1.83}$(s) are given by the equations

$$\log P_{PuO}(\text{atm}) = -\frac{27,810 \pm 600}{T} + 6.710 \pm 0.270 \quad (1)$$

$$\log P_{PuO_2}(\text{atm}) = -\frac{30,330 \pm 240}{T} + 7.750 \pm 0.110 \quad (2)$$

The partial molar heats of sublimation calculated from Eqs. 1 and 2 are 127.2 ± 2.7 and 138.8 ± 1.1 kcal/mol for PuO(g) and $PuO_2$(g), respectively. The total pressure over plutonia has been measured by a number of investigators;[3-7] our results agree well with their data, except those of Phipps et al.,[3] who used tantalum effusion cells.

To study vapor pressures over ($Pu_2O_3 + PuO_{1.61}$), two-phase material[8] was prepared with an O/Pu atom ratio of 1.54. Mass spectrometric observation of the vapor phase over this material indicated Pu(g), PuO(g), and $PuO_2$(g), which, with X-ray diffraction data, indicate that vaporization to produce these species proceeds by the reactions

$$7.33\ Pu_2O_3(s) = 13.66\ PuO_{1.61}(s) + Pu(g) \quad (3)$$

$$2.77\ Pu_2O_3(s) = 4.54\ PuO_{1.61}(s) + PuO(g) \quad (4)$$

$$4.54\ PuO_{1.61}(s) = 1.77\ Pu_2O_3(s) + PuO_2(g) \quad (5)$$

These reactions are based on the assumption that the phase boundaries are $Pu_2O_3$ and $PuO_{1.61}$, and are independent of temperature (Ref. 6, p. 18).

---

[1] J. W. Otvos, D. P. Stevenson, J. Amer. Chem. Soc. 78, 546 (1956).

[2] The appearance potentials, determined by the linear extrapolation method, are 9.4 ± 0.5 eV for $PuO_2$(g), 5.8 ± 0.5 eV for PuO(g), and 6.2 ± 0.5 eV for Pu(g).

[3] T. E. Phipps, G. W. Sears, O. C. Simpson, J. Chem. Phys. 18, 724 (1950).

[4] R. N. R. Mulford, L. E. Lamar, in Plutonium 1960, p. 411, E. Grison, W. B. H. Lord, and R. D. Fowler (eds.), Cleaver-Hume Press, Ltd., London (1961).

[5] R. J. Ackermann, R. L. Faircloth, M. H. Rand, J. Phys. Chem. 70, 3698 (1966).

[6] R. Pascard, CEA, information submitted to a panel on Thermodynamic Properties of Plutonium Oxides held in Vienna, Oct. 24-28, 1966; Technical Reports Series No. 79, "The Plutonium-Oxygen and Uranium-Plutonium-Oxygen System: A Thermochemical Assessment," p. 43, IAEA, Vienna (1967).

[7] D. R. Messier, submitted for publication in J. Amer. Ceram. Soc.

[8] The exact stoichiometry of $Pu_2O_3$ and $PuO_{1.61}$ as a function of temperature has not yet been firmly established; work on this system has recently been initiated (see Section III.A.1.b of this report).

Preliminary temperature-dependency data, normalized at midtemperature, yielded reaction heats in kcal/mol of 110.2, 118.1, and 126.2 for Reactions 3, 4, and 5, respectively. Our value of 118.1 kcal/mol for Reaction 4 is lower than those reported by Ackermann et al,[5] (127.2 kcal/mol) and Phipps et al,[3] (127.7 kcal/mol). The cause for this large difference is not apparent at this time.

The partial pressures of Pu(g), PuO(g), and $PuO_2$(g) over ($Pu_2O_3 + PuO_{1.61}$) as a function of temperature are represented by the equations

$$\log P_{Pu}(atm) = -\frac{24,090 \pm 340}{T} + 5.270 \pm 0.170 \quad (6)$$

$$\log P_{PuO}(atm) = -\frac{25,806 \pm 550}{T} + 7.100 \pm 0.270 \quad (7)$$

$$\log P_{PuO_2}(atm) = -\frac{27,575 \pm 1060}{T} + 5.690 \pm 0.520 \quad (8)$$

(2) Plutonium-Carbon System. Measurements of the partial pressures of vapor species over Pu-C and U-Pu-C have also been initiated. In the Pu-C system, there are, at particular temperatures above 640°C, four thermodynamically invariant two-phase fields consisting of solids only: PuC-$Pu_2C_3$, $Pu_2C_3$-C, $Pu_2C_3$-$PuC_2$, and $PuC_2$-C.

Mass spectrometric analysis of the vapor phase in equilibrium with the condensed systems $Pu_2C_3$ + C and $Pu_2C_3$ + $PuC_2$, in the temperature ranges from 1365 to 1659°C and from 1659 to 2026°C, respectively, showed only the presence of Pu(g). No evidence was found for PuC(g) or $PuC_2$, which indicated that their abundance in the vapor phase was less than 0.1%. This result, coupled with X-ray diffraction data, indicates that vaporization of Pu(g) from the condensed phases proceeds according to the reactions

$$1/2\ Pu_2C_3(s) = Pu(g) + 3/2\ C(s) \quad (<1659°C) \quad (9)$$

$$2\ Pu_2C_3(s) = Pu(g) + 3\ PuC_2(s) \quad (>1659°C) \quad (10)$$

The heats of reaction determined from the slope of the temperature dependency data are 98.1 and 118.7 kcal/mol Pu(g) for Reactions 9 and 10, respectively.

Vapor pressures for Reactions 9 and 10, each at a selected temperature, were determined from measurements of the rates of effusion (weight-loss method). The vapor pressures as a function of temperature obtained by combining the above data are given by the equations

$$\text{Reaction 9:} \quad \log P_{Pu}(\text{atm}) = -\frac{21{,}440 \pm 240}{T} + 4.560 \pm 0.130 \qquad (11)$$

$$\text{Reaction 10:} \quad \log P_{Pu}(\text{atm}) = -\frac{25{,}950 \pm 500}{T} + 6.910 \pm 0.270 \qquad (12)$$

The results for Reaction 9 agree reasonably well with those of Olsen and Mulford.[9] The condensed $Pu_2C_3 + PuC_2$ system has not been previously studied.

Measurements of rates of effusion and temperature dependence are currently being conducted on the condensed $PuC_2 + C$ system. Since Olsen and Mulford[9] as well as others have investigated the $PuC\text{-}Pu_2C_3$ system, our results for the $PuC_2 + C$ system should complete the characterization of the high-temperature volatilization behavior of the Pu-C system from PuC to C.

### b. Phase Diagram Studies of Plutonium Compounds: The Uranium-Plutonium-Oxygen System

The objective of the phase-diagram studies on the U-Pu-O system is to establish the phases existing up to the melting point and compositions at the phase boundaries. The initial part of these studies is concerned with the Pu-O system at high temperature, since information on this system is still incomplete.

In our earlier study[10] of the $U\text{-}UO_2$ system at high temperatures, the existence in the system of a wide liquid miscibility gap was established. At the monotectic temperature, 2470°C, the gap extended over an O/U ratio composition range from about 0.05 to 1.3. It seemed likely that this liquid miscibility gap would extend well into the U-Pu-O system, possibly completely across the system to the $Pu\text{-}PuO_2$ binary side. Initial experiments in the recently completed plutonium facility (ANL-7450, p. 39) were aimed at verifying these possibilities.

Several preparations were made from physical mixtures of plutonium and plutonium dioxide with overall O/Pu ratios of 0.29, 0.38, 0.57, 0.85 and 0.99. These were arc melted; the products of the first four mixtures consisted of both metallic and oxidic appearing portions, whereas the product of the fifth contained only an oxidic material. Metallographic examination of the two-portion products showed that each metallic portion had a similar structure, namely, plutonium with some oxide inclusions, and that each oxidic portion also had a similar structure, namely, that of a monotectic

[9] W. M. Olsen, R. N. R. Mulford, "Thermodynamics of the Plutonium Carbides," in Thermodynamics of Nuclear Materials, p. 467, IAEA, Vienna (1967).

[10] R. K. Edwards, A. E. Martin, Thermodynamics, Vol. 2, Proc. Symp. Vienna, IAEA, Vienna (1966), p. 423.

with plutonium as a dispersed phase in a matrix of oxide. Some of the larger oxide inclusions in the metallic portions were globular with monotectic structures, whereas some of the larger inclusions in the oxidic portions were globules of plutonium. The metallographic appearance of the 0.99 O/Pu preparation, which experienced the relatively large weight loss of 22.7% to yield product with an O/Pu ratio of 1.11, was essentially the same as the oxidic portions of the two-portion arc-melt products. The obvious conclusion from these tests is that a wide liquid miscibility gap does exist in the Pu-$PuO_2$ system at the arc-melting temperature, estimated at about 2500°C.

Measurements of the relative amounts of the metallic and oxidic portions of the preparations with 0.29 and 0.85 O/Pu, with some corrections for minor selective losses of plutonium during melting, have indicated that the liquid miscibility gap extends between O/Pu compositions of about 0.1 and 1.0 at the arc-melt preparation temperature. In view of the relatively small amount of metallic inclusions of appreciable size in the oxidic portions, it is likely that the monotectic composition is also about 1.0 in O/Pu ratio.

An X-ray diffraction examination of a sample of the monotectic portion of the 0.38 O/Pu preparation showed that the dominant phase was hexagonal $Pu_2O_3$ with alpha plutonium as a "possible, very minor" constituent. Thus, $Pu_2O_3$ was shown to be the oxide phase in the monotectic structure and consequently the most plutonium-rich oxide phase in the Pu-$PuO_2$ system at high temperatures.

To establish the monotectic temperature, metallic plutonium was melted in a $Pu_2O_3$ crucible for short periods at successively higher temperatures; when a temperature above the monotectic was reached, the reaction of the plutonium with the crucible caused the charge to melt through the crucible. In this way, the monotectic temperature was indicated as being between 1778 and 1863°C. The monotectic temperature will subsequently be more accurately defined by similar experiments utilizing smaller temperature increments. (Melting tests of 50-mg portions of the oxidic portion of the 0.38 O/Pu arc-melt preparation in tungsten crucibles confirmed the approximate value of the monotectic temperature; a sample heated to 1850°C melted, whereas one heated to 1800°C did not.)

The results of these experiments have, to a degree, established the main features of the plutonium-rich portion of the Pu-$PuO_2$ system at elevated temperatures; these are shown in Fig. III-1. (The melting point of $Pu_2O_3$ in this figure is from the literature.[11])

Since the liquid miscibility gap was observed in both the U-$UO_2$ and the Pu-$PuO_2$ systems in about the same O/M composition range, it seemed likely that a liquid miscibility gap extends as a two-phase field

[11]T. D. Chikalla, C. E. McNeilly, R. E. Skavdahl, J. Nucl. Mater. 12, 131 (1964).

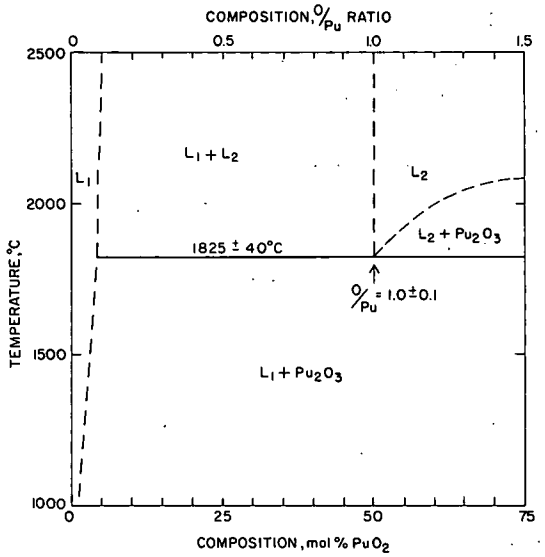


Fig. III-1. Preliminary Phase Diagram of the Plutonium-Rich Portion of the Pu-$PuO_2$ System at High Temperatures.

across the ternary U-Pu-O system at about the same O/M values. One check for the existence of this two-phase field in the ternary system was made at the Pu/U section of 0.25. An alloy of 20% Pu-80% U, made by arc melting, was in turn arc melted with 20% $PuO_2$-80% $UO_2$ oxide in proportions so that the overall O/M composition was 0.5, which was well within the expected two-phase field. The metallographic examination of the product showed that there was a miscibility gap in the ternary U-Pu-O system at this Pu/U section.

### c. Transpiration Studies of the Uranium-Carbon System

An investigation of the vaporization behavior of the uranium-carbon system has been initiated. In addition to acquiring data on the U-C system, the procedures used in this study should be applicable to later studies of the U-Pu-C system. In the study of the U-C system, carbon activity and the total pressure of uranium-bearing species as functions of temperature and composition were measured by the transpiration technique. The transpiration equipment,[12] which had been previously used to investigate the vaporization behavior of the uranium-oxygen system, was modified for the uranium-carbon study (ANL-7450, p. 42). From the measured carbon content in the exit hydrogen carrier gas and the equilibrium constants[13] for the principal gaseous species in equilibrium with graphite at the temperature under investigation, the activity of carbon in the gas phase can be calculated. The total pressure of uranium-bearing species is obtained by collecting the vapor in a condenser tube and assaying the sublimate for uranium.

The results of the measurements of carbon activity as a function of $UC_x$ composition at 2255, 2355, and 2455°K are shown in Fig. III-2. The shapes of the isotherms are consistent with expectations, namely, a sharp decrease in carbon activity as the composition of the condensed phase is reduced toward the lower phase boundary [U(ℓ) + UC] in the hypostoichiometric region. The plateaus of the 2255 and 2355°K isotherms are consistent with the miscibility gap UC + $\beta UC_2$ shown by the phase diagram of the uranium-carbon system.[14] Our measurements

[12] M. Tetenbaum, P. D. Hunt, J. Chem. Phys. 49(11), 4739 (1968).

[13] B. J. McBride, S. Hermel, J. G. Ehlers, G. Sanford, "Thermodynamic Properties to 6000°K for 210 Substances Involving the First 12 Elements," NASA-SP-3001 (1963).

[14] E. K. Storms, The Refractory Carbides, pp. 205-213, Academic Press, New York (1967).

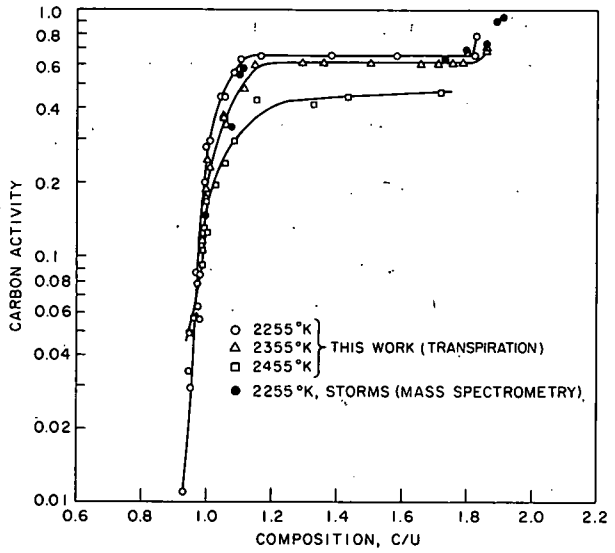


Fig. III-2. Activity of Carbon as a Function of Composition and Temperature.

indicate that the composition at the lower phase boundary of the UC + $\beta UC_2$ diphasic region is C/U ≃ 1.15 at 2255°K, which is in good agreement with the composition C/U ≃ 1.14 estimated from the phase diagram. Our measurements indicate values of C/U ≃ 1.2 and 1.8, respectively, for initial and terminal compositions of the UC + $\beta UC_2$ diphasic region at 2355°K. The values obtained from the phase diagram at this temperature are C/U ≃ 1.2 and 1.35, respectively. Over the composition investigated at 2455°K, the shape of the carbon activity curve is typical of bivariant behavior and is consistent with the phase diagram, which shows a single-phase region above the miscibility gap with a critical temperature of ~2100°C at C/U ≃ 1.3. Calculated carbon activity values at 2255°K are also shown in Fig. III-2; these are based on temperature coefficients derived by Storms[15] from mass spectrometric measurements at 2100 and 2300°K. Our results at 2255°K are in fair agreement with the calculated values.

Measurements of the total pressure of the uranium-bearing species over single-phase UC at 2255°K obtained by the transpiration method are in reasonable agreement with the mass spectrometric measurements of Storms[14,15] (see ANL-7478, p. 102).

An estimate of the free energy of formation of $UC_x$ compositions at 2255, 2355, and 2455°K can be made from our carbon activity values and Storms' extensive uranium vapor pressure values. The estimated values of the free energies (using 126.5 kcal/mol as the heat of vaporization[16] of uranium) are given in Table III-1. The calculated free energies of formation for $UC_{1.00}$ are $-\Delta G_f^\circ$ ≃ 23.3, 23.8, and 25.3 kcal/mol at 2255, 2355 and 2455°K, respectively. For comparison, the thermodynamic assessment of Holley and Storms[17] yields $-\Delta G_f^\circ = 25.2 \pm 2$ kcal/mol at all of these temperatures. The values of the free energy of formation of $UC_x$ shown in Table III-1 should be considered tentative.

---

[15] E. K. Storms, Thermodynamics, Vol. 1, p. 309, IAEA, Vienna (1966).

[16] R. J. Ackermann, E. G. Rauh, "The Vapor Pressure of Liquid Uranium, Effects of Dissolved Tantalum, Phosphorus, Sulfur, Carbon and Oxygen," J. Phys. Chem. (in press).

[17] C. E. Holley, E. K. Storms, Thermodynamics of Nuclear Materials, 1967, p. 417, IAEA, Vienna (1968).

TABLE III-1. Free Energy of Formation of $UC_x$

| 2255°K | | 2355°K | | 2455°K | |
|---|---|---|---|---|---|
| C/U | $-\Delta G_f^\circ$ (kcal/mol) | C/U | $-\Delta G_f^\circ$ (kcal/mol) | C/U | $-\Delta G_f^\circ$ (kcal/mol) |
| 0.97 | 22.2 | 0.97 | 23.6 | 0.97 | 24.4 |
| 1.00 | 23.3 | 1.00 | 23.8 | 1.00 | 25.3 |
| 1.02 | 23.2 | 1.01 | 23.4 | 1.04 | 24.5 |
| 1.05 | 23.4 | 1.05 | 23.2 | 1.06 | 24.6 |
| 1.09 | 24.3 | 1.06 | 23.5 | 1.09 | 25.6 |
| 1.10 | 24.9 | 1.14 | 26.9 | 1.16 | 26.2 |
| 1.16 | 25.6 | 1.84 | 28.8 | 1.33 | 27.6 |
| 1.78 | 28.2 | | | 1.42 | 27.8 |
| 1.81 | 28.6 | | | 1.70 | 30.3 |

Future work will be directed toward extending the measurements of the vaporization behavior of $UC_x$ over a wider range of temperatures and compositions.

2. Enthalpy, Migration, and Other Physical Property Studies

a. Enthalpies and Heat Capacities by Drop Calorimetry

(1) Resistance-Heated Calorimetric System. Enthalpies of materials of interest to the energy conversion program are being measured with the resistance-heated calorimetric system (ANL-7020, p. 172). To carry out these measurements, the system has been modified by installing new heating elements in the furnace and automating the copper-block calorimeter by installing a quartz crystal thermometer. The work is focused on the determinations of enthalpies of $Na_3Bi$ near 850°C. However, enthalpy measurements of $UB_2$ over the temperature range from 579 to 1486°K were carried out in conjunction with the studies employing the electron-beam-heated calorimetric system, reported below. The enthalpy values of $UB_2$ over the temperature range studied can be represented by the equation

$$(H_T^\circ - H_{298}^\circ) = 19.0297T + 1.43535 \times 10^{-3}T^2 + 7.92523 \times 10^5/T - 8351.24 \quad (13)$$

(2) Electron-Beam-Heated Calorimetric System. The electron-beam-heated calorimetric system (ANL-7350, p. 55) has been designed to measure high-temperature enthalpies relative to 25°C. The furnace hot zone consists of a rotating tantalum target that is heated by electron bombardment. An improved target design is now being used that utilizes a 1-in. dia tantalum tube, with a 2-mil wall thickness, for a target support. Because of heat flow, the primary concern is to keep the cross-sectional

area of the supporting tube as small as possible, but yet retain adequate strength. Tantalum discs are stacked inside this tube to cut down radiation to the rotating mechanism, which is located above.

To minimize heat loss during a sample drop, the time required for the sample to drop from the furnace into the calorimeter must be made as short as possible. This was accomplished by attaching a rigid drop rod to the sample capsule, enabling a piston to accelerate the capsule downward. To prevent an unpredictable heat loss due to the rod protruding from the calorimeter after the drop, provision was made to separate the rod from the capsule as the capsule approaches the calorimeter. The calorimeter shutter is then closed after entrance of the capsule, and the capsule heat is measured.

The calorimetric system has been tested over the temperature range from 1300 to 1900°K by obtaining enthalpy data for tungsten metal, a secondary calorimetric standard. Good agreement with data of other laboratories[18,19] was observed.

Work is currently under way on enthalpy measurements of $UB_2$ powder. Data at three temperatures overlapping the range of temperatures employed in the studies with the resistance-heated calorimetric system were in excellent agreement with these results. Extension of the measurements to higher temperatures is planned.

(3) Induction-Heated Calorimetric System; Enthalpy and Heat Capacity of Uranium Dioxide. Determination of the heat capacity of liquid uranium dioxide, an important quantity in fast reactor safety calculations, is continuing. Accurate values of the heat capacity and heat of fusion of molten $UO_2$ will facilitate estimation of the total energy released and the temperatures attained in the core during destructive nuclear excursions. Although the techniques employed [induction heating in conjunction with a drop calorimeter (see ANL-7450, p. 82)] are conventional, they are being used to extend the measurements to temperatures that have not been previously explored.

As part of the initial testing of the system, measurements were made of the enthalpy of tungsten. Measurements by Kirillin et al[18] were made to 3093°K and those of Hein and Flagella[20] to 3248°K. Because of the capabilities of the present equipment, enthalpy measurements of tungsten were extended to 3594°K.[21] These results are presented

[18] V. A. Kirillin, A. E. Sheindlin, V. Ya. Chekhovskoi, V. A. Petrov, Russ. J. Phys. Chem. 37, 1212 (1963).

[19] E. D. West, National Bureau of Standards, private communication.

[20] R. A. Hein, P. N. Flagella, "Enthalpy Measurements of $UO_2$ and Tungsten to 3260°K," GEMP-578 (1968).

[21] L. Leibowitz, M. G. Chasanov, L. W. Mishler, "The Enthalpy of Solid Tungsten from 2800°K to Its Melting Point," Trans. Met. Soc. AIME (in press).

in Fig. III-3. Most of the points shown were obtained with solid tungsten slugs, with corrections being made for radiative heat loss during the drop.[18] Two values for powder samples were obtained by measuring the difference in heat content between an empty tungsten capsule and one filled with tungsten powder. The values for the slug and powder samples are in good agreement. In the region of overlap with earlier work,[18,20] the data also agree well.

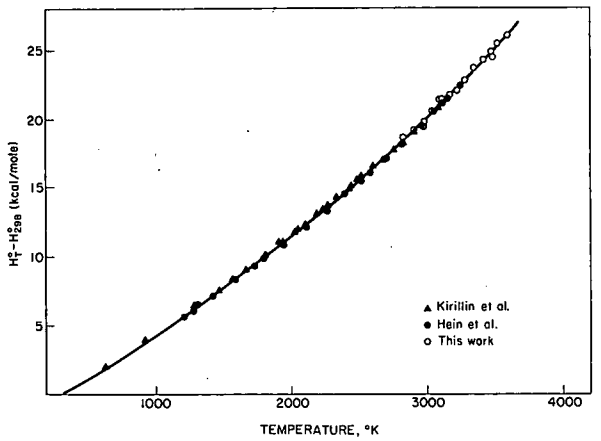


Fig. III-3. Enthalpy of Tungsten.

Measurements of the enthalpy of uranium dioxide are, of course, the primary objective of this study, and these have now been made from 2500 to 3300°K. The data for temperatures below the melting point of $UO_2$ (3123°K) are presented in Fig. III-4. The line drawn through the data in Fig. III-4 is given by the equation

$$H_T^\circ - H_{298}^\circ = 1.0124 \times 10^3 + 3.0577T + 6.3963 \times 10^{-3}T^2 - 7.4317 \times 10^5/T \quad (14)$$

and was fitted to the data by the method of least squares, including the following two constraints:[22]

a) $H_T^\circ - H_{298}^\circ = 0$ when $T = 298$, and

b) $\dfrac{d(H_T^\circ - H_{298}^\circ)}{dT} = 15.2$[23] when $T = 298$.

Agreement between the present results for solid $UO_2$ and those of Hein and co-workers,[20,24,25] also included in the figure, is excellent.

Preliminary values for the enthalpy of $UO_2$ above its melting point are also in good agreement with those of Hein.[25] A preliminary value of 18 kcal/mol was calculated for the heat of fusion of $UO_2$; the value determined by Hein and co-workers[25] is 18.2 kcal/mol.

Measurements of the enthalpy of liquid $UO_2$ are continuing in order to extend the temperature range of these data.

---

[22] T. G. Godfrey, J. M. Leitnaker, "A Computer Program to Calculate High Temperature Thermodynamic Functions," USAEC report ORNL-TM-1599 (1966).

[23] "Thermodynamic and Transport Properties of Uranium Dioxide and Related Phases," Technical Report Series No. 39, IAEA, Vienna (1965).

[24] R. A. Hein, C. H. Sjodahl, R. Szwarc, J. Nucl. Mater. 25, 99 (1968).

[25] R. A. Hein, P. N. Flagella, J. B. Conway, J. Amer. Ceram. Soc. 51, 291 (1968).

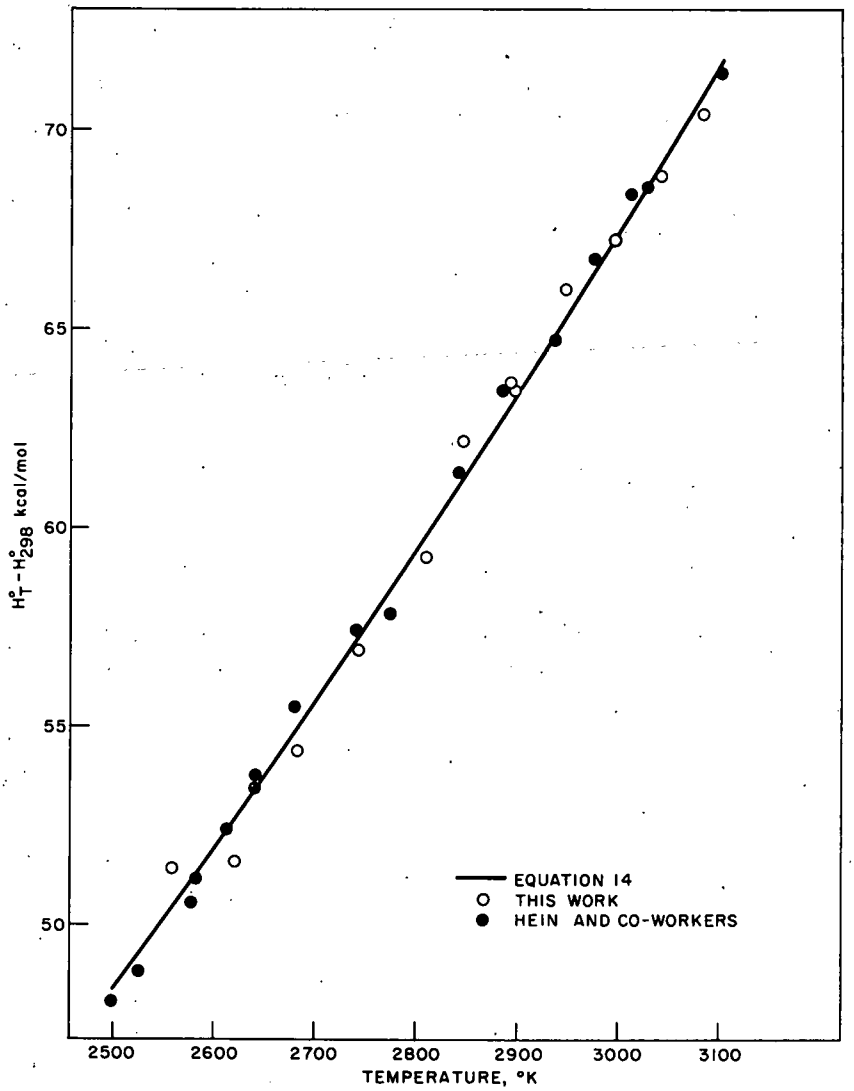


Fig. III-4. Enthalpy of $UO_2$.

b. Other Physical Property Studies

A serious difficulty in the analysis of fast reactor hazards is the lack of reliable data on the physical properties of liquid uranium dioxide and other ceramic fast-reactor fuels. In addition to heat capacity measurements (discussed above), data are needed on such properties as vapor pressure, surface tension, viscosity, compressibility, expansion coefficients, and thermal conductivity. Construction and testing have begun of equipment suitable for vapor pressure measurements by transpiration methods.

Initial analytical efforts have involved preliminary calculations of surface tension, compressibility, and volume expansivity of

liquid $UO_2$ based on the scaled particle theory.[26] This theory has had outstanding success in calculating properties of molten salts. Two input parameters are required: the density of the liquid ($\rho$) and the distance of closest approach of the ions (a). Some calculations were made using density estimates of Robbins[27] and the sum of ionic radii for $\rho$ and a, respectively, assuming a corresponding-states behavior at higher temperatures. The values obtained seem reasonable to a first approximation, and as appropriate experimental data become available, corrections and modifications will be made. A computer program has been employed in conjunction with measurements of frozen $UO_2$ menisci to estimate the surface tension of liquid $UO_2$. A preliminary value obtained from examination of one meniscus is 420 dyne/cm.

### c. Segregation in Ceramic Fuels: Fuel Migration Studies

Migration and segregation of fissile and fertile materials within a fast reactor fuel during its operational lifetime could have significant effects on the operational safety of the fuel. Redistribution of plutonium in $(U,Pu)O_2$ fuels might change the chemical and physical properties of the affected regions enough to alter the neutronics of the system, affect fuel-cladding compatibility, and change the resultant fission product distribution. Investigation of the migration of plutonium and fission products in mixed-oxide fuels in a thermal gradient is under way. These experiments are being performed to evaluate the extent of migration and elucidate the mechanisms involved in the migration processes. Extension of the program to carbide fuels is planned.

Experiments are in progress using right-circular cylindrical pellets 1/2 in. high by 1/2 in. in diameter, which were prepared from coprecipitated $UO_2$-$PuO_2$; the pellets are all nominally $(U_{0.8}Pu_{0.2})O_{2.00}$. These are heated for the desired time period in the thermal gradient furnace previously described in ANL-7450, p. 86. The samples are then analyzed for plutonium and uranium with an electron microprobe analyzer.

In Experiment P-5, the pellet was heated in the thermal-gradient furnace for 1020 hr; the temperature at the pellet top was 1970°C, whereas the temperature at the pellet bottom was 1140°C. As in Experiment P-3 (ANL-7450, p. 88), this specimen was heated in an inverted tungsten crucible. The results of an electron microprobe analysis along the longitudinal axis of the pellet after the heating had been completed are shown in Fig. III-5a; there seems to be clear evidence of an increase in plutonia concentration at the hotter end of the pellet. The relative smoothness of this increase in concentration implies that it is probably not due to the presence of segregated plutonia in the unheated pellet.

---

[26] H. Reiss, "Scaled Particle Methods in the Statistical Thermodynamics of Fluids," in Advances in Chemical Physics IX, I. Prigogine (ed.), Interscience, New York (1965).

[27] E. J. Robbins, "Limits for the Equation of State of Uranium Dioxide," TRG 1344(R) (1966).

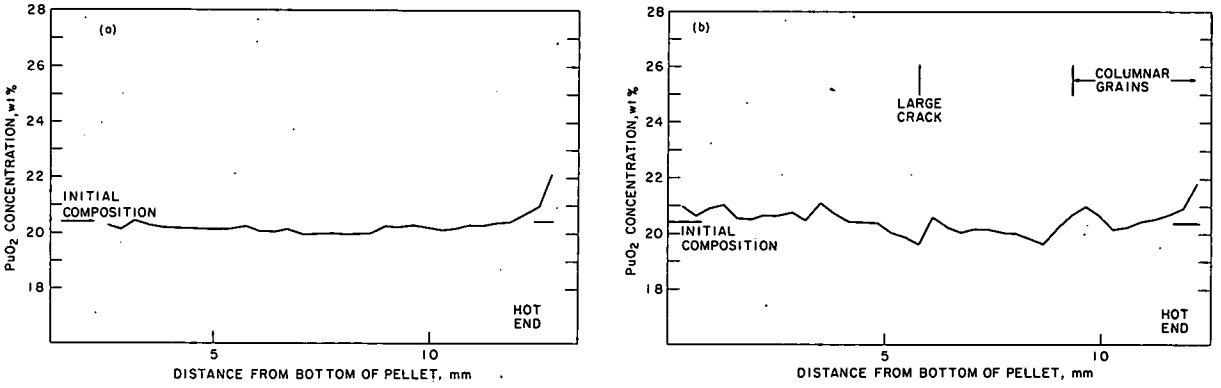


Fig. III-5. $PuO_2$ Distribution in $(U_{0.8}Pu_{0.2})O_2$ Pellets Heated in a Thermal Gradient in Tungsten Crucibles; (a) Pellet P-5: $T_{top}$ = 1970°C, $T_{bottom}$ = 1140°C, 1020 hr; (b) Pellet P-8: $T_{top}$ = 2340°C, $T_{bottom}$ = 1220°C, 123 hr.

In Experiment P-8, the pellet was heated in a tungsten crucible for 123 hr; the top temperature was 2350°C (which was considerably higher than heretofore achieved), and the bottom temperature was 1220°C. The probe analysis along the longitudinal axis of this pellet is shown in Fig. III-5b. Although the variations in plutonia concentration along the pellet are greater than those for pellet P-5, the increase in plutonia concentration at the hotter end of pellet P-8 is quite evident.

Oxygen analyses were performed on samples cut from several of the heated pellets. These showed the expected trend, a marked decrease of oxygen content in the hotter portions of the pellets. In addition, there was an overall loss of oxygen from the pellets, the losses being larger for pellets that were heated for longer periods and held at high temperatures. A sample from the top fourth of pellet P-5 had an O/M ratio of 1.92, whereas one from the bottom fourth had an O/M ratio of 1.94 (the initial O/M ratio of the unheated pellets was 2.00 ± 0.01). In the case of pellet P-8, heated at much higher temperatures, the O/M ratio for the top region was 1.81, while the bottom region had an O/M ratio of 1.92. The O/M ratios in the heated pellets appeared to vary smoothly from the top to the bottom of the pellet.

Future work with $(U,Pu)O_2$ pellets will be directed toward achieving temperature gradients similar to those achieved in Experiment P-8 but maintaining them for longer periods of time.

## B. Chemistry of Irradiated Fast-Reactor Fuels and Materials

An understanding of the chemical and physical behavior of fast reactor fuels during irradiation is necessary for the selection, fabrication, and utilization of fuel and reactor materials that will meet the high-performance criteria required in future commercial fast breeder reactors. The current program is concerned primarily with establishing the properties of irradiated uranium-plutonium oxides clad in stainless steel.

## 1. Electron Microprobe Analysis of Irradiated $UO_2$-$PuO_2$ Fuel

The electron microprobe, which accomplishes microsampling and analysis directly, is being used to provide information on the distribution of uranium, plutonium, and fission products in irradiated fuel as a function of radial position. A detailed study has been made of a cross section of a vibratorily compacted $UO_2$-20 wt % $PuO_2$ fuel pin clad in type 304 stainless steel and irradiated in EBR-II to 2.7 at. % burnup. Initial results of this work were reported in ANL-7450, pp. 50-53. The present report extends these results.

Distribution of Plutonium and Uranium. Plutonium and uranium analyses were obtained for several different radial segments of the fuel cross section. The distribution and homogeneity of the uranium and plutonium oxides were directly associated with concentric microstructural regions that are typical of the temperatures attained in these regions during irradiation. A photomicrograph of one of these radial segments and a corresponding plot of the radial distribution of uranium and plutonium are shown in the uppermost plot of Fig. III-6. The concentrations of both plutonium and uranium are combined in the plot as wt % $(PuO_2/PuO_2 + UO_2)$.

The innermost zone of the fuel, which reached the highest temperature during irradiation, contained long and short columnar grains. In the long columnar grain region (A to B in Fig. III-6), the separate particles of $UO_2$ and $PuO_2$ present in the original fuel material formed a homogeneous solution on a micron scale. The long columnar grains were grouped in clusters of three or four having identical uranium and plutonium concentration profiles (within 0.1 wt % for any given radial position). The maximum difference in concentration between groups of grains for identical radial positions was 2 wt %. In the band of short columnar grains (B to C in Fig. III-6), homogeneity was almost complete. However, the radial-distribution curves in this region were not identical; peaks and valleys occurred at different radial positions from curve to curve.

Although some formation of solid solution was observed in the transition zone of equiaxed grains (C to D in Fig. III-6), many plutonium-free $UO_2$ particles exceeding 50 $\mu$m in cross section and smaller uranium-free $PuO_2$ particles were also observed. This region, which attained intermediate temperatures during irradiation, provided distribution curves that varied markedly from one radial position to another.

Little, if any, solid solution occurred in the outer zone of the fuel (D to E in Fig. III-6), which attained the lowest temperature. The fuel in this region consisted of discrete particles of $UO_2$ and $PuO_2$. Although particles of $UO_2$ as large as 200-300 $\mu$m in cross section were observed, most particles were less than 50 $\mu$m in cross section. Particles of $PuO_2$

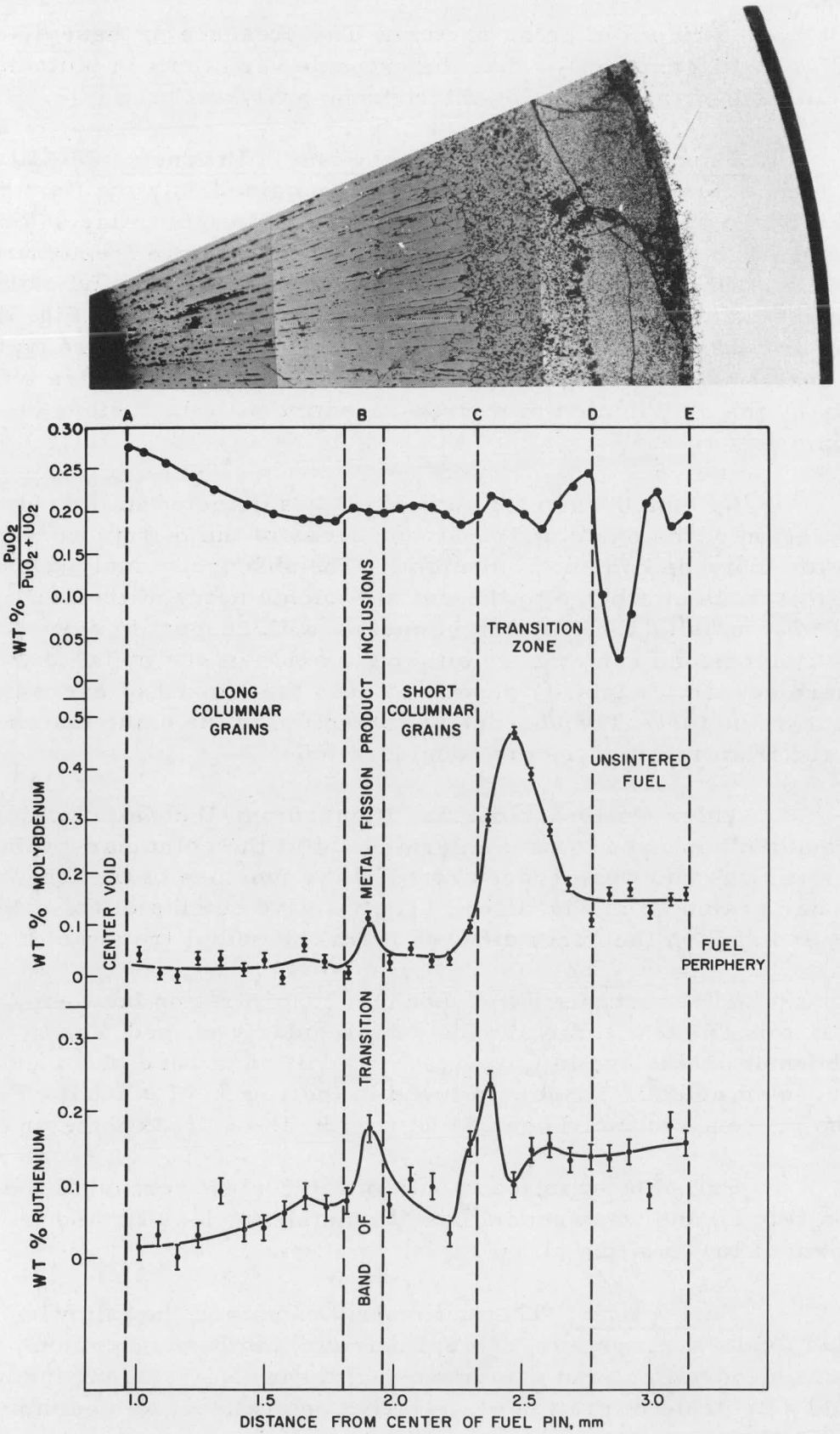


Fig. III-6. Radial Distributions of Plutonium, Uranium, Molybdenum, and Ruthenium in a $UO_2$-20 wt % $PuO_2$ Fuel Pin (2.7 at. % burnup).

did not exceed 50 $\mu$m in cross section. The presence of these discrete particles of $UO_2$ and $PuO_2$ cause the extreme variations in plutonium and uranium concentrations during microprobe analyses.

Distribution of Noble Metal Fission Products. Metallic inclusions found in the columnar grain region contained only the fission products molybdenum, ruthenium, technetium, and rhodium; these inclusions varied in composition as a function of radial position and were free of uranium and plutonium. Complete radial distributions of molybdenum and ruthenium were obtained, and their concentrations are plotted separately in Fig. III-6. The distributions shown along the radius chosen for the figure are typical of all radii analyzed. The shapes of these distribution profiles were influenced mainly by the distribution of micron-sized metallic inclusions of these fission products.

No molybdenum or ruthenium was detected in the columnar-grain region of the oxide matrix (other areas of the matrix were not analyzed for molybdenum and ruthenium). The absence of molybdenum in the oxide matrix is attributed to the initial stoichiometry of the fuel: the $UO_2$-$PuO_2$ was slightly hypostoichiometric with respect to oxygen. Apparently, molybdenum can exist in either the oxide or the metal phase, with its thermodynamic stability dependent upon the amount of excess oxygen present in the fuel. The absence of ruthenium in the oxide matrix was expected from thermodynamic considerations.

The metallic inclusions of ruthenium, technetium, molybdenum, and rhodium appeared to have migrated out of the columnar-grain region to cooler regions and were concentrated at the juncture of the long and short columnar grains (B in Fig. III-6). The relative heights of the peaks at points B and C on the curve differed from one radial traverse to another.

The increase in molybdenum concentration between C and D in Fig. III-6 is due to a large number of irregularly shaped, essentially pure molybdenum inclusions in this area. In addition, a band of a metallic iron-molybdenum eutectic phase was found in the region of point D. The reasons for the presence of molybdenum and iron in these areas is being investigated.

Palladium was found only in the coolest portion of the fuel (the region D to E) and was associated with metals such as tin and tellurium in the form of low-melting alloys.

Fuel Matrix. The fuel matrix contained the following fission product oxides: zirconium, cesium, barium, lanthanum, cerium, praseodymium, neodymium, and samarium. Of these, only cesium and barium showed detectable migration or selective relocation. No cesium was detected in the columnar grain-growth region, but large amounts were found

in the cooler (unsintered) region of the fuel, primarily adjacent to the cladding. Smaller amounts were found in the equiaxed grain-growth region. Barium was barely detectable in the columnar-grain regions, but was found in larger amounts in the cooler region.

The distributions of zirconium, lanthanum, cerium, praseodymium, neodymium, and samarium showed no variation with radial position. The observed concentrations of these elements agreed quite well with the expected values based on theoretical fission yields. The distribution of the neodymium as a function of radial position is shown in Fig. III-7. The ordinate in the figure is expressed in three ways: neodymium, counts/sec; wt % neodymium; and equivalent burnup of total uranium and plutonium based on theoretical fission yields.

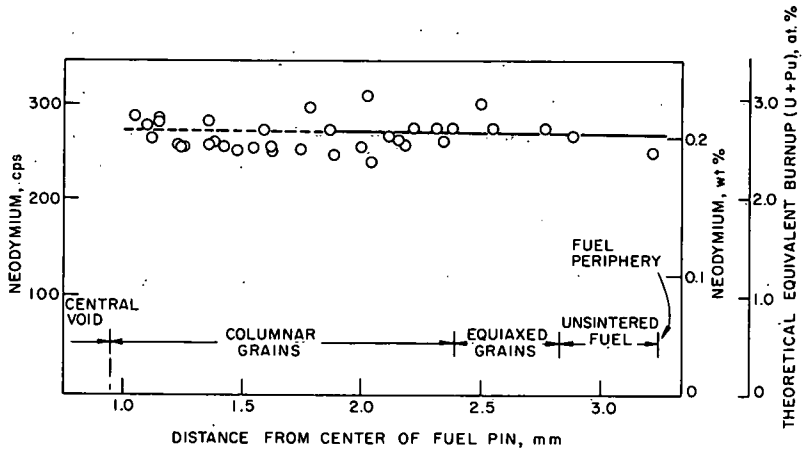


Fig. III-7. Radial Distribution of Neodymium in a $UO_2$-20 wt % $PuO_2$ Fuel Pin (2.7 at. % burnup).

Oxide Inclusions. Barium oxide was found not only in the $UO_2$-$PuO_2$ matrix but also in oxide inclusions distributed throughout the equiaxed region. These inclusions resulted from interaction of barium with an $Al_2O_3$ impurity introduced into the fuel during a ball-milling operation. The composition of the inclusions varied with radial position. In the equiaxed region near the columnar grains, the inclusions were primarily $BaO \cdot 6Al_2O_3$ with trace amounts of chromium oxide (<1 wt %); in the cooler portion of the equiaxed region near the unsintered zone, the inclusions were either aluminum oxide or aluminum oxide containing small amounts of barium oxide, chromium oxide, and, sometimes, strontium and cesium oxides.

## 2. Chemical Studies of Fuel Materials

### a. Laser-Beam Microsampling System

A study of the interaction of sodium with stainless steel is being made with a microsampling device that consists of a small ruby laser

attached to a microscope. With this device, specimens were vaporized from specific locations of stainless steel samples that had previously been exposed to molten sodium. Sample preparation was accomplished by grinding, polishing, and etching the stainless steel using nonaqueous techniques that removed superficial sodium but did not remove any sodium that had penetrated the stainless steel. Samples were obtained by making one to five laser shots in the area of interest and collecting all the vaporized material on a single cover plate. The individual craters produced were of reasonably uniform size, having an average diameter of ~55 $\mu$m and a depth of ~10 $\mu$m; this size corresponds to an estimated sample weight of about 70 ng for each laser shot. The samples were dissolved and analyzed for sodium by a flame-photometric technique.

In a sample of type 304 stainless steel[1] that had been exposed to sodium of low oxygen content (<12 ppm), a trace of sodium was found in only one location. The area around this location was sampled further, but no additional sodium was found. Other samples of type 304 stainless steel[2] were also examined; in the exposure of these samples to sodium, no attempt had been made to minimize the oxygen content of the sodium. Analyses showed that, in general, traces of sodium were found only at cracks or spots that showed some sign of attack; however, in one sample of this group, a different type of behavior was found. This sample was a tube having a 0.020-in. wall that had been machined to 0.005 in. in one segment. The tube had been filled with sodium, sealed, and heated to ~600°C. Laser samples were taken from both the 0.020- and 0.005-in. portions of the tubing. In the 0.005-in. segment, sodium was found on the inner and outer polished surfaces of the tubing and within the tubing wall. In the 0.020-in. segment, sodium was found on both surfaces, but not within the tubing wall. Sodium concentrations, based on an estimation of sample weights, ranged from 0.3 to 1.5 wt %.

Further experiments are planned to investigate the nature of the interaction of sodium with stainless steel. Samples of stainless steel will be exposed to sodium under carefully controlled conditions, and an attempt will be made to correlate any evidence of interaction with conditions of exposure.

### b. Determination of Thermodynamic Oxidizing Potential in Irradiated Oxide Fuel

A study has recently been undertaken to develop a reliable method for measuring the thermodynamic oxidizing potential of high-burnup oxide fuels, primarily uranium-plutonium oxides. This quantity is an important parameter in fuel-development studies because it strongly affects such properties as thermal conductivity of the fuel and fuel-cladding compatibility.

---

[1]Sample supplied by W. E. Ruther of the Metallurgy Division.

[2]Samples supplied by F. A. Smith of the Reactor Engineering Division.

In unirradiated uranium oxide and uranium-plutonium oxide fuels, the oxygen-to-metal (O/M) ratio is a good measure of the oxidizing potential, and a number of methods are in general use for determining O/M ratios in unirradiated fuel. However, none of these have been applied to the analysis of high-burnup fuels. In addition, it has not been established whether the O/M ratio of a fuel of even moderate burnup will provide a useful measure of the oxidizing potential.

The interpretation of data obtained from measurement of O/M ratios in irradiated fuels will be complicated by the following factors: (1) reaction of oxygen in the fuel with some of the fission products to produce a metal-oxygen system that is much more complex than the initial uranium-plutonium-oxygen ternary system, (2) reaction of oxygen in the fuel with the cladding and with impurities introduced into the fuel during fabrication, (3) the known mobility of oxygen in the fuel matrix, and (4) the large thermal gradients in the fuel during irradiation and consequent uncertainties in the temperatures attained in various regions of the fuel.

In our work and in the studies of other investigators, very distinct differences have been observed in the physical and chemical properties of irradiated fuels of different initial stoichiometries. Some of the effects of initial stoichiometry on the behavior of fuel constituents are summarized in Fig. III-8. It should be emphasized that, although these effects are well established, the O/M ratios at which the changes occur are, at best, approximations based on sparse and often conflicting data. A correlation of effects such as these with changes in O/M ratio or oxidizing potential during irradiation should prove valuable in predicting the overall performance of a fuel in a reactor.

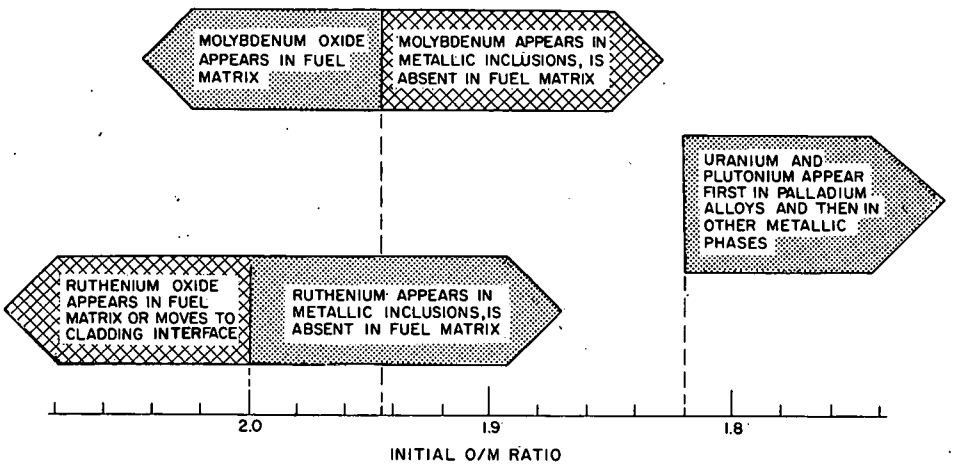


Fig. III-8. Effects of Initial O/M Ratios on the Behavior of Some Fuel Constituents in $UO_2$ and $UO_2$-$PuO_2$ Fuels.

As a first step in this study, possible methods for determining oxidizing potentials will be evaluated and means for overcoming the difficulties associated with analysis of irradiated fuels will be investigated.

### c. Spark-Source Mass Spectrometry

Installation of a spark-source mass spectrometer (Associated Electronics Industries Model MS-7) has been completed in the past year. The instrument has been modified for high-vacuum sealing, alignment of the slit system, and focusing of the ion beam. It has now been calibrated and is in satisfactory operating condition.

The planned addition of a densitometer will greatly increase the output capabilities of the mass-spectrometer system; this instrument handles photoplates and evaluates line intensities automatically, thus minimizing operator attention.

In the immediate future, the mass spectrometer will be used for the analysis of metallic sodium samples from EBR-II (see Subsection 3.a, below) and irradiated fuel samples. A portable inert-atmosphere glovebox has been designed and is being constructed for transferring both types of samples into and out of the source chamber.

## 3. Feasibility Study of Fuel-Failure Detection: Sodium-Soluble Tags

The development of methods for identifying the position of failed fuel in an operating fast reactor such as EBR-II is important to the overall fast reactor program. A program has been undertaken to investigate the feasibility of tagging each fuel element in a particular subassembly with a unique radiochemical or isotopic tag. In the event of a fuel failure, the tag would be released to the primary sodium coolant, and detection of the tag in the sodium would identify the subassembly containing the failed fuel.

To assure reliable identification of a faulty subassembly, appropriate tags must be selected and their detection sensitivity in sodium evaluated (the concentration of tagged elements in the sodium coolant will be a few nanograms per gram of sodium). Techniques must also be developed for placement of the tags in the fuel rod assembly so that they remain available for dispersion into the primary sodium stream should failure occur.

The method of tagging described above is intended for use in EBR-II with sodium-bonded fuel or encapsulated fuel having sodium in the annulus between the cladding and the capsule. A complementary technique, intended primarily for use with unencapsulated gas-bonded fuel, is described elsewhere in this report (Section III.C).

### a. Trace Element Analytical Techniques

Identification of failed fuel elements in EBR-II by means of sodium-soluble tags requires that the type and concentration of impurities

already present in EBR-II primary sodium be known. As part of this investigation, several samples of EBR-II sodium have been examined for trace impurities by spark-source mass spectrometry, gamma spectrometry, and neutron activation analysis.

A preliminary mass-spectrometric examination of "as-received" sodium samples indicated traces of Al, Si, Ca, Cr, Fe, Ni, Mo, Pd, Sn, Bi, Ag, and some rare earths. However, positive identification of the lines in the spectra was complicated by the presence of sodium oxide and complex sodium polymers. Further work on sodium samples awaits the installation of an inert-atmosphere box at the sample entrance port of the spark-source mass spectrometer (see Subsection 2.c, above). The more rigorous protection of the sample and sample chamber from oxygen should minimize oxide contamination. The removal of sodium from the trace elements by distillation will also be investigated; this technique will concentrate impurities and reduce the problem of sodium handling.

Examination of "as-received" sodium samples by gamma spectrometry showed the presence of trace amounts of $^{134}Cs$, $^{137}Cs$, $^{113m}In$, $^{110m}Ag$, and $^{22}Na$; however, the detection sensitivity for impurities with low gamma-ray energies was considerably reduced by the presence of $^{22}Na$ activity. For this reason, effort was concentrated on developing techniques for the separation of the trace impurities from the bulk sodium.

Preliminary experiments indicated that some impurities could be separated from the sodium by ion-exchange procedures using Dowex-1 and Chelex-100 resins. Additional separations and concentrations were effected by adsorption of impurities on ferric hydroxide and potassium cobaltiferrocyanate. These procedures provided an adequate separation from $^{22}Na$ activity. Gamma-spectrometric analysis of the resins and precipitates showed the presence of traces of $^{125}Sb$, $^{117m}Sn$, $^{113}Sn$, $^{113m}In$, $^{110m}Ag$, $^{54}Mn$, $^{134}Cs$, and $^{137}Cs$.

Present effort is being concentrated on neutron-activation analysis to detect impurities with short-lived activation products. In initial tests, impurities separated by ferric hydroxide precipitation were reirradiated in the CP-5 reactor; subsequent re-examination by gamma spectrometry revealed that the spectra were highly complex. It is believed that analysis of the spectra can be greatly simplified by computer treatment of the data. Accordingly, an existing computer program is being adapted for this purpose, and a library of data on gamma energies of activation products and fission products is being completed.

### b. Tag-confirmation Study

The preliminary selection of tags and development of sensitive analytical techniques will require confirmatory studies of the stability of the tag in the sodium-coolant stream and the continued availability of the tag in the fuel pin during an extended irradiation period.

The major effort thus far has been devoted to the design and construction of a small-scale experimental loop for circulating liquid sodium. The construction of the loop is nearing completion. The loop will provide facilities for (a) testing and comparing various sodium sampling techniques and (b) evaluating the behavior of very low concentrations of radiochemical or stable isotopes (approximate levels, nanogram per gram of sodium) in circulating sodium.

## C. Xenon Tagging of Fuel Elements in EBR-II

A program is under way to determine the feasibility of applying mixtures of xenon isotopes as tags for the identification of fuel elements that fail in a nuclear reactor. The work will be carried out in EBR-II with experimental fuel elements, and will entail the development of the identification procedure, the production of suitable mixtures of xenon tags, and the design and construction of the necessary equipment. Emphasis will be placed on the application of the xenon-tag method to the identification of unencapsulated, gas-bonded fuel elements, most of which will contain $UO_2$-$PuO_2$.

The EBR-II reactor is adequately instrumented to detect fuel-cladding failure by monitoring delayed neutrons in the sodium coolant and radioactive fission gases in the reactor cover gas. However, identification of a subassembly in which failure has occurred is difficult and time-consuming. In the proposed xenon-tagging procedure, each fuel element in a subassembly will be tagged with 1 ml of a mixture of xenon isotopes that is unique for a particular subassembly. If a cladding failure is indicated by one of the failure-detection instruments, a sample of the reactor cover gas will be analyzed mass-spectrometrically to determine the ratios of the xenon isotopes. These data will indicate the xenon-tag mixture released; comparison of these data with data obtained from the analysis of a master sample of the indicated mixture will be used to establish positive identification of the failed element(s), and will, at the same time, identify the affected subassembly. It is anticipated that identification can be accomplished within the 4-hr period required to prepare for the removal of a subassembly. This rapid identification should significantly enhance the EBR-II plant factor.

### 1. Preparation of Xenon-Tag Mixtures

Because xenon isotopes with mass numbers 131 through 136 are abundantly produced by fission, xenon-tag mixtures for failed-fuel identification must contain significant concentrations of isotopes of the lower mass numbers 124 through 129. Mound Laboratory[1] is currently producing several different mixtures of isotopes that have been enriched in lighter isotopes by

[1]Mound Laboratory, Miamisburg, Ohio; operated by the Monsanto Research Corporation for the USAEC.

thermal diffusion. Table III-2 shows the isotopic composition of three of these mixtures, as well as that of natural xenon. Initially, tag mixtures, designated Series A, will be prepared by blending each of three Mound Laboratory mixtures with natural xenon in preselected proportions. The $^{129}Xe/^{124}Xe$ ratios in the Series A tag mixtures will range from 4.9 to 73 (the ratio in natural xenon is 275). Released tags from Series A mixtures will normally be identified by the $^{129}Xe/^{124}Xe$ isotopic ratio.

TABLE III-2. Isotopic Composition of Natural Xenon and Three Enriched Mixtures from Mound Laboratory

| Xenon Isotope Mass Number | Total Xenon[a] (mol %) | | | |
|---|---|---|---|---|
| | Mound Mixture | | | Natural Xenon |
| | No. 1 | No. 2 | No. 3 | |
| 124 | 12.0 | 5.7 | 1.3 | 0.096 |
| 126 | 4.5 | 1.9 | 0.8 | 0.090 |
| 128 | 17.4 | 10.1 | 8.1 | 1.92 |
| 129 | 59.0 | 63.8 | 64.3 | 26.44 |
| 130 | 2.4 | 4.2 | 5.1 | 4.08 |
| 131 | 2.8 | 9.1 | 12.8 | 21.18 |
| 132 | 1.4 | 4.8 | 7.1 | 26.89 |
| 134 | 0.3 | 0.3 | 0.5 | 10.44 |
| 136 | 0.2 | 0.1 | 0.1 | 8.87 |

[a]Xenon purity ≥99.0%.

Additional tag mixtures (Series B) will be prepared by blending Mound Laboratory enriched mixtures with pure $^{128}Xe$ prepared by neutron irradiation of natural iodine[2] in a thermal reactor. The $^{128}Xe/^{124}Xe$ isotopic ratio in the Series B tag mixtures is presently planned to extend from 2.0 to 9.3 (the ratio in natural xenon is 20.0). Released tags from Series B tag mixtures will normally be identified by the $^{128}Xe/^{124}Xe$ isotopic ratio. The anticipated isotopic ratios for the Series A and B tag mixtures are shown in Fig. III-9. Each line represents a planned sub-series and each point an

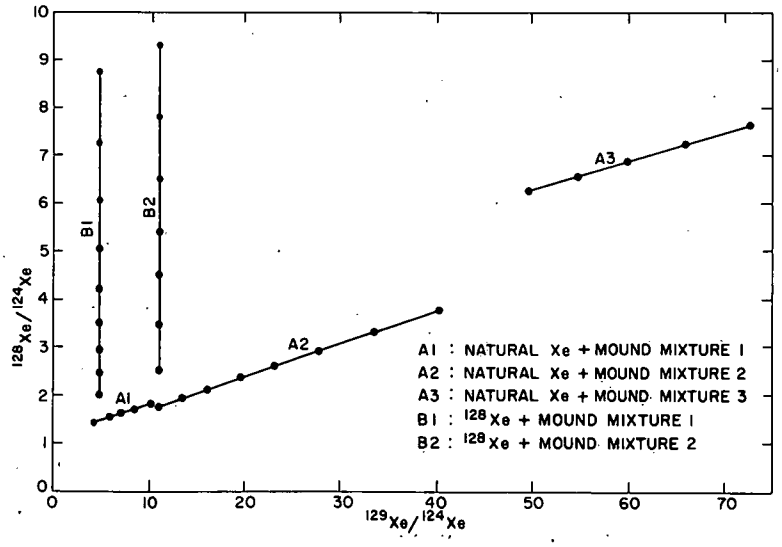


Fig. III-9
Isotopic Relationships of Xenon Tags.

[2]Natural iodine is 100% $^{127}I$; $^{128}Xe$ is formed by the reactions $^{127}I(n,\gamma)^{128}I \xrightarrow{\beta^-} {}^{128}Xe$.

individual tag. The preparation of 34 tagging mixtures is presently planned; however, preparation of an appreciably greater number of tags is feasible.

2. Addition of a Tag to a Fuel Element

Gas-bonded fuel elements irradiated in EBR-II consist of a fuel region and a gas plenum to contain released fission gases. The inside diameter of the cladding is about 1/4 in., the fuel length is about 14 in., and the gas-plenum length is usually greater than 8 in. A suggested method of tag addition consists of injecting 1 ml of the tag near the bottom of the fuel element gas plenum while the element is in the conventional helium-filled glovebox used for element closure.

Two experiments were performed to determine whether the diffusional loss of xenon from a fuel element plenum before final closure would be excessive. In the first experiment, 0.18-in. ID, 7.2-in.-long tubes were used to simulate fuel-element plenums. In the second, longer tubes containing 14-in.-long drill rods were used to simulate gas-bonded fuel elements having 7.2-in.-long plenums and 24-mil fuel-to-cladding diametral gaps. In each experiment, the tubes were charged slowly (in 5 to 10 sec) with 1 ml of natural xenon, allowed to remain open to a helium atmosphere for a predetermined interval of time, and then capped with a septum. The xenon and helium in the tubes were then mixed, sampled, and analyzed with a gas chromatograph.

The experimental results showed that the rate of diffusion of xenon was not affected by the presence of a diametral gap and that diffusional losses were not significant. Approximately 90% of the charge remained in the tubes after 110 sec. (The estimated time required for closure of fuel elements is ~1 min.) Losses of 10-20% of a tag by this means would not impair identification of a released tag because identification depends only on the determination of the isotopic ratios.

The experimental data on rates of loss of xenon by diffusion were compared with calculated values obtained by the use of simplified diffusion equations[3] in which the plenum is assumed to be a part of a semi-infinite tube. This comparison is illustrated in Fig. III-10. The experimental and calculated values are in good agreement up to losses of ~10%. This correlation allows estimation of xenon diffusion rates for fuel elements of different sizes and geometries, and thereby provides a guide for limiting losses to acceptable levels during closure.

[3] J. Crank, The Mathematics of Diffusion, p. 13, Clarendon Press, Oxford (1964).

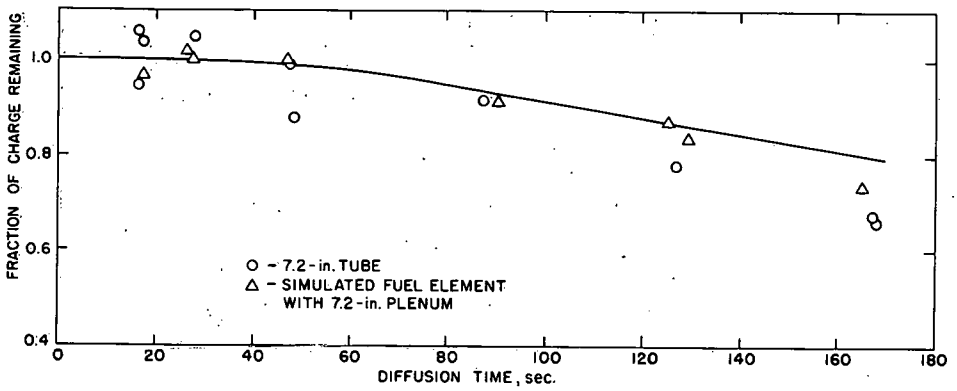


Fig. III-10. Xenon Diffusion Experiments (1 ml Xe charged to 0.18-in.-ID tube).

### 3. Evaluation of Xenon Tagging System

Consideration was given to possible detrimental effects that might arise from the presence of 1 ml of xenon tag mixture in gas-bonded fuel elements. Only one such effect appeared possible, namely, a decrease in the thermal conductance of the fuel-to-cladding gap during early irradiations. An evaluation was made of the available data on the gap conductance of fast-reactor mixed oxide fuels;[4,5] this study indicated that the gap conductance of these fuels, like that of thermally irradiated $UO_2$ fuel,[6] was independent of the species of gas present. From this, it was concluded that the use of xenon tags in fast-reactor oxide fuel elements would not endanger the fuel element or the reactor.

Consideration was also given to the factors that could create difficulties in identifying a released tag. These were as follows: (1) contamination of the tag by light xenon isotopes in either the fuel-element gas plenum or the reactor cover gas, (2) significant neutron transformations of the tag isotopes within the fuel element, and (3) delay or prevention of transport of the tag to the reactor cover gas by solubility effects in the bulk sodium.

Contamination of the tag by xenon isotopes from cumulative fission yields will not be significant because the isotopes of primary interest are shielded. Under assumed operating conditions,[7] approximately 0.02 ml of $^{128}Xe$ can result from neutron capture by fission product $^{127}I$, and the concentrations of the tag mixtures have been selected to tolerate such $^{128}Xe$ contamination. Under the same conditions,[7] neutron transformation of the

[4] W. E. Baily, E. A. Aitken, R. R. Asamoto, C. N. Craig, "Thermal Conductivity of Uranium-Plutonium Oxide Fuels," presented at Nucl. Met. Symp., AIME, Phoenix, Arizona (Oct. 4-6, 1967).

[5] W. E. Baily, C. N. Craig, E. L. Zebroski, "Effect of Diametral Gap Size on the In-Pile Performance of Fast Ceramic Reactor Mixed-Oxide Fuel," Trans. Amer. Nucl. Soc. 9(1), 40 (1966).

[6] J. Belle, Uranium Dioxide: Properties and Nuclear Applications, pp. 585-609, U.S. Government Printing Office, Washington (1961).

[7] Mixed-oxide fuel element (72 g) irradiated at 15 kW/ft to 100,000 MWd/metric ton burnup near center of 50-MW EBR-II.

tag isotopes will not hamper tag identification unless the transformation cross section exceeds 0.50 b for $^{128}Xe$ and 0.24 b for $^{129}Xe$. It is doubtful that cross sections would be this high in the hard (95% of the neutrons >0.07 MeV) EBR-II flux.

Estimates[8] of the low solubility of xenon in 370°C bulk sodium ($\sim 5 \times 10^{-12}$ atom Xe/atom Na at 1 atm xenon pressure) indicate that solubility will not impair tag transfer from a fuel element to the cover gas. In addition, results of over 15 accidental fission-gas releases in EBR-II show that neither pseudo-solubility (formation of microbubbles) nor surface sorption have affected xenon transfer.

The effects of xenon contamination of the reactor cover gas from air leakage, supply argon, tramp fuel,[9] and previous cladding failures were studied experimentally.[10] The cover gas was sampled and analyzed before and after addition of a 0.7-ml tag. Calculations showed that the background xenon in the cover gas was only 3-5% of the added tag. The contaminants in the cover gas only changed the key isotopic ratio ($^{129}Xe/^{124}Xe$) from 11.29 to 11.36; the next isotopic ratio in the series, 13.5, would be readily distinguishable.

The xenon tagging system is considered feasible and desirable. The first tag mixture has been made available for use in EBR-II. It is expected that by early 1969 all unencapsulated gas-bonded fuel elements entering EBR-II will be xenon-tagged.

## D. Calorimetry

The calorimetry program is directed toward the determination of thermodynamic properties of substances that are of interest in high-temperature chemistry and nuclear reactor technology. At present, only room-temperature enthalpies of formation ($\Delta Hf^{\circ}_{298}$) are sought. A continuing part of the program is directed toward the calculation of bond energies, the correlation of enthalpies of formation, and the calculation of tables of thermodynamic functions.

The method of fluorine bomb calorimetry was developed for substances not amenable to conventional calorimetric methods. Where appropriate, oxygen bomb calorimetry is also employed. The acquisition of a commercial solution calorimeter and the development of a rocking solution calorimeter, now in the testing stages, considerably widens the scope of calorimetric reactions that can be studied.

---

[8] E. Veleckis, Argonne National Laboratory, private communication (1968).

[9] Small amounts of fuel inadvertently introduced into the sodium coolant.

[10] Experiments performed by the ANL Idaho Division.

## 1. Thermochemistry of Uranium Compounds

### a. Enthalpy of Formation of Uranium Diboride

As part of a continuing program to provide accurate thermochemical data for uranium compounds, the standard enthalpy of formation of uranium diboride was determined by fluorine bomb calorimetry. Hexagonal diboride was synthesized by repeated arc melting of a mixture of high-purity boron and uranium. The single-phase product had a total impurity content of about 0.05% and a B/U atomic ratio of 1.979 ± 0.006. The enthalpy of the fluorination reaction was measured and combined with our earlier determinations of $\Delta Hf°(UF_6,c)$[1] and $\Delta Hf°(BF_3,g)$[2] to yield $\Delta Hf°_{298}(UB_{1.979},c)$ = -39.1 ± 2.6 kcal mol$^{-1}$. The only other value reported for the enthalpy of formation of $UB_2$ is Rand and Kubaschewski's estimate[3] of -35.3 ± 3 kcal mol$^{-1}$.

The thermochemical effort on uranium diboride was supplemented in the Chemistry Division with low-temperature heat capacity and entropy measurements on the same specimen of $UB_{1.979}$. These data will be reported in a forth-coming publication, together with the enthalpy-of-formation work and some derived thermodynamic properties. In addition, high-temperature enthalpy increments of $UB_{1.979}$ were measured in the temperature range 600-1500°K; the results are reported in Section III.A.2.a.

### b. Enthalpy of Formation of β-Uranium Disulfide

The energy of combustion of orthorhombohedral uranium disulfide (β-$US_2$) in fluorine was measured by essentially the same technique as that used for uranium diboride. The single-phase specimen had an impurity content of about 0.09% and an anion-to-cation atomic ratio of 2.000 ± 0.002. By combining the enthalpy of the fluorination reaction with $\Delta Hf°(UF_6,c)$[1] and $\Delta Hf°(SF_6,g)$,[4] the value $\Delta Hf°_{298}(US_2,\beta)$ = -124.2 ± 2.1 kcal mol$^{-1}$ was obtained. Rand and Kubaschewski[3] had estimated this value as -120 ± 10 kcal mol$^{-1}$.

Further thermochemical measurements on uranium-sulfur compounds are projected. Samples of $US_{1.9}(\alpha)$ and $US_3$, now on hand, are being analyzed to determine whether or not their compositions and purities are acceptable for calorimetric combustions. [Determination of the value $\Delta Hf°_{298}(US_{1.011})$ = -73.2 ± 3.5 kcal mol$^{-1}$ was reported earlier.[5]]

---

[1] J. L. Settle, H. M. Feder, W. N. Hubbard, J. Phys. Chem. 67, 1892 (1963).
[2] G. K. Johnson, H. M. Feder, W. N. Hubbard, ibid. 70, 1 (1966).
[3] M. H. Rand, O. Kubaschewski, The Thermochemical Properties of Uranium Compounds, Interscience Publishers, New York, N. Y. (1963).
[4] P. A. G. O'Hare, J. L. Settle, W. N. Hubbard, Trans. Faraday Soc. 62, 558 (1966).
[5] ANL-7450, p. 62.

## 2. Thermochemistry of Plutonium Compounds

The technique of oxygen bomb calorimetry was selected to determine the enthalpies of formation of the potential reactor fuels plutonium mononitride and plutonium monocarbide.

### a. Enthalpy of Formation of PuN

The standard enthalpy of formation, $\Delta Hf^{\circ}_{298}$, of stoichiometric PuN(c) was found to be $-71.51 \pm 0.62$ kcal $mol^{-1}$. This value may be compared with the oxygen bomb calorimetric result of Lapage and Bunce,[6] $-70.2 \pm 1.5$ kcal $mol^{-1}$, and the result deduced by Spear and Leitnaker[7] from equilibrium measurements, $-76.0 \pm 1.0$ kcal $mol^{-1}$. We consider our value to be the most reliable obtained thus far.

### b. Enthalpy of Formation of Plutonium Monocarbide

Since no reliable calorimetric measurement of the enthalpy of formation of plutonium monocarbide has been reported, we have undertaken this task. Plutonium monocarbide was prepared (in the Metallurgy Division) by arc melting high-purity plutonium and graphite to give a product that contained 1 to 5% $Pu_2C_3$ as a second phase, as well as 0.35% of other impurities (mainly tungsten). Despite these impurities, the specimen was judged suitable for calorimetric use; the uncertainties thereby introduced affect the final result to about the same extent as do the scatter of the experimental data or the uncertainties of the required auxiliary enthalpy data. The composition $C/Pu = 0.859 \pm 0.013$ was assigned to the monocarbide phase on the basis of the $Pu_2C_3$ content and the assumption that all other impurities were in solid solution in the monocarbide phase.

The preliminary result obtained from the combustion of this specimen in oxygen was $\Delta Hf^{\circ}_{298}(PuC_{0.859},c) = -11.23 \pm 0.67$ kcal $mol^{-1}$, which compares favorably with some of the results derived from high-temperature equilibrium studies on various monocarbide compositions.

## 3. Enthalpy of Formation of Liquid Hydrogen Fluoride

Hydrogen fluoride (HF) is a key thermochemical compound. Its importance in fluorine reaction calorimetry is analogous to that of water in oxygen reaction calorimetry. Yet, $\Delta Hf^{\circ}(HF)$ has not been determined with sufficient accuracy. Furthermore, $\Delta Hf^{\circ}(HF,aq)$--another important quantity because of the many thermochemical values dependent on calorimetric reactions involving aqueous HF--also lacks sufficient accuracy: $\Delta Hf^{\circ}(HF,aq)$ is obtained by combing $\Delta Hf^{\circ}(HF)$ with values of $\Delta H_{soln}$ of HF in water (which are somewhat uncertain).

---

[6] R. Lapage, J. L. Bunce, Trans. Faraday Soc. 63, 1889 (1967).

[7] K. E. Spear, J. M. Leitnaker, USAEC Report ORNL-TM-2106 (1968).

To help correct this situation, $\Delta Hf°(HF,l)$ has been determined directly by measuring the energy of the reaction of fluorine with excess hydrogen in a bomb calorimeter. The combustion chamber was presaturated with HF(g) so that the only reaction product would be HF(l). In this manner, one of the problems with the existing thermochemical data, the uncertain correction for the nonideality of HF(g) at room temperature, was avoided. The preliminary value obtained for $\Delta Hf°_{298}(HF,l)$ is $-71.8 \pm 0.2$ kcal $mol^{-1}$.

4. Enthalpies of Formation of $IF_5$ and $IF_7$

A long-range interest in the thermochemistry of halides in general and, more specifically, of thermally decomposable iodides used in purification or vapor plating of metals (e.g., van Arkel-de Boer method with $ZrI_4$, $UI_4$) led to our measurement of the enthalpies of formation of $IF_5$ and $IF_7$ by fluorine bomb calorimetry.

Iodine and fluorine were found to react spontaneously on contact, yielding a mixture of $IF_5$ and $IF_7$. By varying the excess of fluorine, the yield of $IF_7$ could be made as small as a few tenths of a percent or as large as 80 percent. The relative amounts of $IF_5$ and $IF_7$ produced in each combustion were determined by differential iodometric titration of the hydrolyzed combustion product. A linear relationship was derived between the mole percent of $IF_7$ produced and the internal energy change per gram of iodine reacted. Extrapolation of this line to its extremes, i.e., 100% $IF_5$ or 100% $IF_7$, yielded $\Delta Hf°_{298}(IF_5,l) = -210.7 \pm 0.5$ kcal $mol^{-1}$ and $\Delta Hf°_{298}(IF_7,g) = -227 \pm 3$ kcal $mol^{-1}$.

5. Enthalpy of Formation of $GeF_4$

Fluorine reaction calorimetry has been developed at this laboratory into a powerful general method for deriving the enthalpies of formation of a large variety of compounds, and we have strongly advocated its use. Accordingly, we were concerned when the application of fluorine calorimetry to combustion of germanium by different laboratories led to the discrepant values $\Delta Hf°_{298}(GeF_4,g) = -284.37 \pm 0.15$ kcal $mol^{-1}$ [8] and $-274.13 \pm 0.13$ kcal $mol^{-1}$.[9] In an attempt to uncover the cause of this discrepancy, we measured the energy of combustion of germanium in fluorine and derived the value $\Delta Hf°_{298}(GeF_4,g) = -284.58 \pm 0.21$ $(2\sigma)$ kcal $mol^{-1}$. This value is in excellent agreement with that reported by Gross and coworkers and, taken together with other evidence, points to an error in Charlu and Margrave's result. The source of the error cannot be established unequivocally without repeating their work, but we suspect that it is connected with their combustion technique.

[8] P. Gross, C. Hayman, J. T. Bingham, Trans. Faraday Soc. 62, 2388 (1966).

[9] T. V. Charlu, J. L. Margrave, J. Chem. Eng. Data (in press).

## 6. Enthalpies of Formation and Solution of Boric Oxides

A previous report[10] noted that our fluorine bomb calorimetric determination of $\Delta Hf^\circ_{298}(B_2O_3, \text{amorph})$, -299.52 ± 0.51 kcal $mol^{-1}$, agreed with the literature values obtained by solution calorimetry; however, the values obtained for $\Delta Hf^\circ_{298}(B_2O_3,c)$, -303.02 ± 0.51 kcal $mol^{-1}$, and, consequently, for the enthalpy of transition, 3.50 ± 0.33 kcal $mol^{-1}$, disagreed with those in the literature. Because a significant error in one or both of our combustion results was possible, additional calorimetric combustions were made, and the enthalpies of solution in water of both forms of $B_2O_3$ were determined.

The solution reaction that was studied is given by

$$B_2O_3(s) + 686\ H_2O(l) \rightarrow 2(H_3BO_3 \cdot 341.5\ H_2O)(l) \qquad (1)$$

where $B_2O_3(s)$ is either crystalline or amorphous. The enthalpy (at 298°K) obtained for Reaction 1 was -3.54 ± 0.04 kcal $mol^{-1}$ with $B_2O_3(c)$ and -7.98 ± 0.06 kcal $mol^{-1}$ with $B_2O_3$(amorph). The enthalpy of transition, 4.44 ± 0.07 kcal $mol^{-1}$, is in excellent agreement with the literature values 4.36 ± 0.02[11] and 4.33 ± 0.06[12] kcal $mol^{-1}$.

Combustions of crystalline $B_2O_3$ in fluorine yielded $\Delta Hf^\circ_{298}(B_2O_3,c)$ = -304.50 ± 0.59 kcal $mol^{-1}$, which is 1.48 kcal $mol^{-1}$ more negative than the earlier result. Two combustions of the amorphous specimen yielded $\Delta Hf^\circ_{298}(B_2O_3, \text{amorph})$ = -300.1 kcal $mol^{-1}$, which is in accord with the earlier result. The enthalpy of transition computed from the present combustion data, 4.4 kcal $mol^{-1}$, is in excellent agreement with that obtained for the same specimens by solution calorimety.

Apparently, the earlier fluorine bomb calorimetric determination of $\Delta Hf^\circ(B_2O_3,c)$ is in substantial error from some unknown cause.

## 7. Enthalpy of Formation and Dissolution of Potassium Perbromate

A preparative method for the synthesis of perbromates ($BrO_4^-$), hitherto unknown, was recently announced by E. H. Appleman of the Chemistry Division.[13] A joint effort with the Chemistry Division is under way to determine some of the thermodynamic properties of perbromates and, possibly, to learn why they have been so difficult to prepare. Our current objective is to determine the enthalpy of formation of $KBrO_4$ and the enthalpy of its dissolution in water. A comparison of the thermodynamic properties of $KBrO_4$, $KClO_4$, and $KIO_4$ will be made.

---

[10] ANL-7225, p. 147.

[11] J. C. Southard, J. Amer. Chem. Soc. 63, 3147 (1941).

[12] L. G. Fasolino, J. Chem. Eng. Data 10, 373 (1965).

[13] E. H. Appleman, J. Amer. Chem. Soc. 90, 1900 (1968).

The method chosen to determine $\Delta Hf°(KBrO_4)$ involves a two-step thermal decomposition in a combustion bomb, according to Eqs. 3 and 4:

$$KBrO_4 \xrightarrow{275°C} KBrO_3 + 1/2\ O_2 \qquad (3)$$

$$KBrO_3 \xrightarrow{390°C} KBr + 3/2\ O_2 \qquad (4)$$

The energy needed for the decomposition is supplied by the reaction of graphite with oxygen. Trial decompositions with $KBrO_3$ have proved successful, and the calorimetric measurements on $KBrO_4$ have been started.

The decomposition of $KBrO_3$ will also be measured since the reported enthalpies of formation of $KBrO_3$ and $BrO_3^-$ are highly uncertain and only little additional effort is entailed. The solution calorimetry on $KBrO_4$ has been completed, but the results are not available yet.

### 8. Calculation of Thermodynamic Functions

A computer program has been set up to calculate by means of the rigid-rotator, harmonic-oscillator approximation the thermodynamic functions $C_p^\circ$, $S°$, $-(G° - H_0^\circ)/T$, and $(H° - H_0^\circ)/T$ for molecules in the ideal gas state. The program also derives values for the functions $H° - H_{298}^\circ$, $\Delta Hf$, $\Delta Gf$, and log Kf. The computations have been made for the chalcogen fluorides, $P_2$, $P_4$, some phosphorus fluorides, $As_2$, $As_4$, some arsenic fluorides, $Ge_2$, and the germanium fluorides. Tabulated values (0-2000°K or 0-6000°K) of these functions are being published in ANL topical reports. One of our interests in these tables is the calculation of thermodynamic equilibria of high-temperature gaseous reactions.

## E. Chemistry of Liquid Metals

A research program designed to develop a better understanding of the physicochemical properties of liquid sodium in particular and of liquid metals in general is in progress. The emphasis on sodium stems from both fundamental and technological considerations. Knowledge of the chemical and physical properties of sodium is a prerequisite to its use as a reactor coolant and also may help to understand and control corrosion in liquid sodium systems.

Structural materials corrode in liquid sodium as a result of carburization, decarburization, nitridation, denitridation, and oxidation, as well as mass transfer. However, an understanding of the mechanisms involved in these processes is lacking and is a principal objective of the current research. Major effort is being placed on identifying the species responsible for carbon transport and carburization in sodium-steel systems and on measuring the solubility in sodium of compounds that may be important in nitridation. In addition, evidence is being sought for the existence of interatomic

complexes in liquid metallic solutions, a concept that has been invoked to account for the migration of transition metals between steels in sodium systems. Thermodynamic activities in selected fission product-sodium systems are also being measured.

## 1. Mechanism of Carbon Transport in Sodium Systems

Various mechanisms for carbon transport in liquid sodium systems have been proposed, but none has been generally accepted. Identification of the migrating carbon-bearing species could provide significant insight into this mechanism, and experiments with this aim have been undertaken. Materials labeled with beta-active $^{14}C$ are being used to differentiate between the carbon that is transported and the carbon that exists as a contaminant of sodium, a distinction that has proven difficult to make in past studies.

It was shown previously that the carbon from a capsule made of a ferritic $^{14}C$-labeled iron-carbon alloy migrated through liquid sodium at 650°C to an immersed austenitic coupon made of type 304 stainless steel (SS).[1] Detectable quantities of labeled carbon remained in the sodium even after 165 hr at temperature. To provide samples of sodium for the identification of this $^{14}C$-labeled species, further experiments, both with and without transport, were made and are discussed below.

Experiments without Transport. In a typical experiment, reactor-grade sodium was sealed in a crucible made of a ferritic iron-carbon alloy (0.030% C) labeled with carbon-14. The crucible was sealed in a secondary capsule and heated at 650°C for 120 hr. After being cooled to room temperature, the crucible was opened and the sodium was dissolved in deaerated water, which was subsequently acidified. Analyses for carbon-containing compounds in the resulting off-gas, solution, and residue showed that the bulk of the labeled carbon appeared in the off-gas; hence, effort was concentrated on identifying the labeled species in this fraction first. Results of radiogas chromatographic analyses[2] on a typical off-gas are given in Table III-3 under "Ferritic Alloy + Na."

TABLE III-3. Radiogas Chromatographic Analysis of Gases from Aqueous Dissolution of Sodium

| | Ferritic Alloy[a] + Na | | Ferritic Alloy[a] + Na + 316 SS | |
|---|---|---|---|---|
| Gas | Ppm C in Na | Specific Activity (dpm/μg C) | Ppm C in Na | Specific Activity (dpm/μg C) |
| $C_2H_2$ | 18 | 2740 | 0.34 | 1910 |
| $C_2H_4$ and $C_2H_6$ | 2.2 | 2600 | 0.19 | 1750 |
| $CH_4$ | trace | - | trace | - |
| $CO_2$ | 1.8 | 28 | 3.7 | 15 |

[a]Specific activity 2650 ± 200 dpm/μg C.

[1]ANL-7450, p. 71.

[2]R. Wolfgang, F. S. Rowland, Anal. Chem. 30, 903 (1958).

Acetylene is the major $^{14}C$-labeled gas. Its specific activity is in close agreement with that of the carbon in the ferritic iron-carbon alloy. The ethylene and ethane found in small amounts are believed to originate from hydrogenation of acetylene during dissolution. The similarity of their specific activities is consistent with this contention. The minor amount of $CO_2$ found and its very low specific activity indicate that it originated from a carbonate impurity that was originally present in the sodium or introduced during the experiment.

Experiments with Transport. In these experiments, an austenitic type 316 SS coupon was immersed in the sodium; otherwise, the experimental conditions were identical with those above. The results of a typical analysis of the off-gas from the sodium in these experiments are given in Table III-3 under "Ferritic Alloy + Na + 316 SS." The concentrations of acetylene and of ethylene plus ethane (and therefore of the precursor) are drastically reduced. This result is consistent with the frequent observation made here and elsewhere that austenitic steels in liquid sodium behave as sinks for carbon supplied by ferritic alloys. Note also that the specific activities of the hydrocarbons are about 30% lower than that of the source carbon in the ferritic crucible. Dilution by inactive carbon in this experiment is most likely due to the precursor of $CO_2$ ($Na_2CO_3$) or to carbon from the stainless steel. This is suggested by our observations that acetylene is one of the gases evolved on aqueous dissolution of sodium that contains $Na_2CO_3$ and is heated above 450°C, or of sodium that is simply heated at 650°C while held in type 304 SS.

Separation of the precursor of the acetylene from sodium for identification by direct methods was impractical; hence its identity was deduced. Only acetylides (salts of $C_2^=$) are known to react with water to give acetylene. Hence the most likely precursor of acetylene in these experiments is disodium acetylide ($Na_2C_2$). The possibility that $CaC_2$ (from calcium impurity in the sodium) was involved was ruled out in separate experiments that showed that acetylene production was independent of calcium concentration in sodium. Cementite, $Fe_3C$, from the ferritic crucible--which might have gotten into the sodium--was ruled out as a precursor of acetylene by showing that methane, but no acetylene, was formed by the hydrolysis of manganese-stabilized $Fe_3C$ with aqueous NaOH.

The finding that considerably less acetylene was evolved from the sodium with the carbon sink than without strongly suggests that its precursor, $Na_2C_2$, partook in the carbon transport. Insight into the mechanism of $Na_2C_2$ formation was gained from the mechanism postulated for $Li_2C_2$ formation in lithium-steel systems. Various workers[3,4,5] have proposed

[3]N. M. Beskorovainyi, V. K. Ivanov, M. T. Zuev, in High-Purity Metals and Alloys, V. S. Emel'Yanov, A. I. Evstyukhin (eds.), Consultants Bureau, New York (1967).

[4]M. Beniere, M. Chemla, M. Aucouturier, P. LaCombe, C. Roques-Carmes, Corrosion 24(4), 83 (1968).

[5]E. F. Hoffman, USAEC Report ORNL-2924 (1960).

that corrosion of carbon steels in lithium proceeds via the reaction of cementite in grain boundaries, according to the following thermodynamically favored reaction:

$$2\ Li(l) + 2\ Fe_3C(s) \rightarrow Li_2C_2(s) + 6\ Fe(s) \qquad (1)$$

The formation of $Na_2C_2$ in sodium-steel systems may proceed by an analogous reaction:

$$2\ Na(l) + 2\ Fe_3C(s) \rightarrow Na_2C_2(s) + 6\ Fe(s) \qquad (2)$$

Flint in 1965 suggested that $Na_2C_2$, formed according to Reaction 2, was involved in carbon transport. By assuming that the free energy and enthalpy of formation of $Na_2C_2$ were approximately equal, he estimated the free energy of Reaction 2 to be about -3 kcal/mol at 550°C, i.e., the reaction is thermodynamically possible. However, because of the tenuous nature of this conclusion, accurate measurements of the thermodynamic functions of $Na_2C_2$ are needed, and this work is now beginning.

## 2. Solubility of Nitrogen Compounds in Liquid Sodium

Transport of nitrogen is known to occur in sodium-steel systems but has received only limited attention in the past. Thermodynamic and kinetic data on common nitrogen compounds in sodium, which are needed to begin a rational study of the mechanism of transport, are lacking. To correct this situation, studies are being made on the solubility and stability of nitrogen compounds frequently found in sodium-cooled reactors. The first compounds investigated were sodium cyanide, which appears in large amounts as a precipitate in reactor cold traps, and nitrogen gas, which is known to exist as a contaminant in reactor cover gas.

### a. Solubility of Sodium Cyanide

The solubility of cyanide in liquid sodium was determined by equilibrating reactor-grade sodium with excess sodium cyanide at a preselected temperature, withdrawing a sample of the melt through a stainless steel filter into a tantalum pipette, dissolving the sodium from the pipette, and assaying the resulting aqueous solution spectrophotometrically[6] for cyanide.

The results of the solubility experiments are given in Table III-4. Solubilities were measured both below and above the monotectic temperature, which was found by thermal analysis to be 565 ± 2°C. A monotectic in the Na-NaCN system had been anticipated because cyanide ion is a pseudohalide[7] and monotectics had been observed[8] with the Na-sodium

[6] I. Nusbaum, P. Skupeko, Metal Finishing 49(10), 61 (1951).
[7] T. Moeller, Inorganic Chemistry, p. 463, John Wiley and Sons, Inc., New York (1952).
[8] M. A. Bredig, J. W. Johnson, W. T. Smith, Jr., J. Amer. Chem. Soc. 77, 307 (1955).

halide systems. The reliability of each solubility value was established by multiple determinations. The data collected below the monotectic temperature were fitted by the method of least squares to the linear equation

$$(400\text{-}565°C)\ \log\ (\text{ppm CN}) = 13.5 - 9140\ T^{-1}$$

The heat of solution calculated from this equation is 42 ± 5 kcal/mol.

TABLE III-4. Solubility of Sodium Cyanide in Liquid Sodium

| Temp. (°C) | Mean Solubility (ppm CN) | Relative Std. Dev. (%) | Number of Determinations |
|---|---|---|---|
| 402 | 0.70 | 79 | 12 |
| 425 | 4.2 | 111 | 8 |
| 450 | 4.2 | 123 | 12 |
| 500 | 40 | 25 | 8 |
| 525 | 160 | 14 | 14 |
| 549 | 180 | 18 | 10 |
| 575 | 500 | 28 | 8 |
| 600 | 780 | 27 | 8 |
| 650 | 1630 | 14 | 6 |

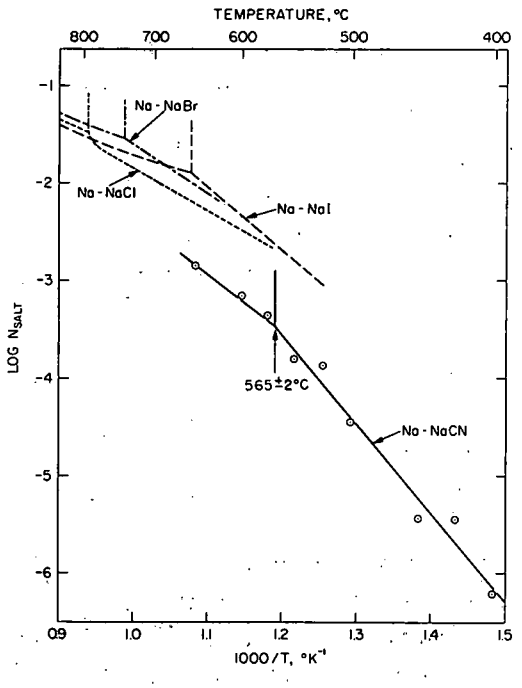


Fig. III-11. Solubilities (Mole Fraction) of Sodium Cyanide and Sodium Halides in Liquid Sodium.

The variation with temperature of the solubility of NaCN in liquid sodium (on a mole fraction basis) is shown in Fig. III-11 together with similar data for NaCl, NaBr, and NaI. The qualitative resemblance between the cyanide and halide solubility curves is consistent with the usual behavior of the cyanide ion as a pseudohalide.

Finally, it is noteworthy that the solubility found for sodium cyanide is the highest measured so far for any carbon- or nitrogen-containing compound in sodium. Consequently the tendency of cyanide to carburize and nitride steel was tested. Type 304 SS tabs were immersed for about 8 days at 660°C in reactor-grade sodium (~8 ppm carbon, 20 ppm oxygen) containing 0.15% NaCN. The reactants were contained in an alumina crucible, which was sealed inside a stainless steel capsule. Analysis of the tabs showed that the carbon and nitrogen concentrations, initially 0.07% and 0.03%, respectively, increased approximately threefold. It appears that cyanide in liquid sodium is quite effective in simultaneously carburizing and nitriding steel.

b. Solubility of Nitrogen Gas

The solubility of nitrogen was measured by saturating reactor-grade sodium at a preselected temperature with nitrogen at 10 atm, stripping the dissolved nitrogen from sodium with helium, trapping the stripped gas on liquid-nitrogen-cooled molecular sieves and transferring it to a bulb, and, finally, analyzing it with a mass spectrometer.

The solubility experiments were carried out with the aid of nitrogen enriched with nitrogen-15. In this manner, the dissolved nitrogen could be distinguished from extraneous nitrogen. The measurements were made at 50-deg intervals between 450 and 600°C, with the results shown in Table III-5. The solubilities are Henry's law constants expressed in parts per trillion per atmosphere nitrogen pressure. The reliability of each solubility value was established by multiple determinations. The data were fitted by the method of least squares to the linear equation

$$(450\text{-}600°C)\ \log S = -7.18 - 2780\ T^{-1}$$

where S is solubility in grams of nitrogen gas per gram of sodium per atmosphere, and T is temperature in degrees Kelvin. The heat of solution obtained from this equation is 13 ± 3 kcal/mole.

TABLE III-5. Solubility of Nitrogen in Liquid Sodium[a]

| Temp. (°C) | Mean Solubility (g $N_2$ per $10^{12}$ g Na per atm pressure) | Relative Standard Deviation (%) | Number of Determinations |
|---|---|---|---|
| 451 | 10 | 78 | 7 |
| 502 | 17 | 44 | 6 |
| 550 | 25 | 31 | 7 |
| 600 | 44 | 21 | 6 |

[a]All solubilities were determined at ~10 atm nitrogen pressure.

The use of nitrogen-15 tracer provided not only the requisite sensitivity for the solubility measurements but also an insight into the nature of the dissolution process. The sodium was saturated with isotopically unequilibrated nitrogen having the typical composition 27.4 mol % $^{15}N_2$, 49.6 mol % $^{14}N_2$, and 23.0 mol % $^{14}N^{15}N$. If this nitrogen dissolved monatomically, then random recombination of the atoms on exsolution would be expected to give the equilibrated composition 15.2 mol % $^{15}N_2$, 37.3 mol % $^{14}N_2$, and 47.5 mol % $^{14}N^{15}N$. However, mass spectrometric analyses of the stripped gas revealed only a small change in isotopic composition to 25.7 mol % $^{15}N_2$, 46.1 mol % $^{14}N_2$, and 28.2 mol % $^{14}N^{15}N$, which

is not consistent with purely monatomic dissolution. More likely, this change is catalytic, occurring at the hot steel surfaces of the apparatus. (Slow exchange between $^{15}N_2$ and $^{14}N_2$ over hot iron catalysts has been observed.[9]) The results, therefore, appear to be consistent with the mechanism of diatomic dissolution of molecular nitrogen in sodium. Past studies have shown that diatomic gases dissolve or react monatomically in liquid metals; this is the first to show that molecular dissolution also occurs.

### 3. Stability of Carbon and Nitrogen Species in Liquid Sodium

Information concerning the bond strengths of compounds dissolved in liquid sodium is virtually nonexistent. The solubility and transport studies described above provide some insight: the triple covalent (electron-rich) bonds that link the nitrogen atoms in $N_2$, the carbon atoms in acetylide ion ($C_2^=$), and the carbon and nitrogen atoms in cyanide ion ($CN^-$) are seen to be stable in sodium at temperatures as high as 650°C. Apparently, electron-rich bonds such as these are stabilized in the electron-rich environment of liquid sodium. It is interesting to note in this connection that carbonate ion ($CO_3^=$), in which the bond order is 4/3, is unstable in sodium above ~400°C, and that its decomposition proceeds with formation of the apparently more stable acetylide ion.[10] Although this information on bond strengths is rather limited, it suggests that the more electron-rich the bond, the greater is its stability in sodium.

### 4. Molecular Complexes in Liquid Metallic Solutions

Complex-formation, a phenomenon known to occur in nonmetallic liquids, has also been claimed in metallic liquids. The transport of transition metals between steels in liquid sodium, for example, is said to proceed via sodium-oxygen-transition metal complexes.[11] Similarly (and more generally), anomalies in curves of viscosity or electrical conductivity of binary liquid metallic solutions are often ascribed to the formation of complexes. The existence of complexes in liquid metals, however, has not been substantiated by direct experimental observation; hence their existence or nonexistence has been the subject of much controversy. Although optical spectroscopy, a common method for detecting complexes in liquids, cannot be used to resolve this controversy because of the opacity of metals, ultrasonic absorption spectrometry offers an alternate approach.

Nonmetallic liquids exhibit three types of sonic absorption: (a) classical absorption[12] (e.g., liquid argon); (b) excess absorption without maxima,[13] as in structured systems (e.g., alcohols); and (c) excess absorption

[9] J. T. Kummer, P. H. Emmett, J. Chem. Phys. 19, 289 (1951).

[10] J. A. J. Walker, E. D. France, UK Atomic Energy Authority, TRG Report 1635(c) (1968).

[11] G. W. Horsley, J. Iron and Steel Inst. 182, 43 (1956).

[12] Absorption due only to the viscosity and thermal conductivity of the liquid.

[13] Absorption in excess of classical but which is characterized by an absorption coefficient proportional to the square of frequency.

with one or more maxima vs. frequency, as in systems with dissociable complexes (e.g., $MgSO_4$ and $H_2O$).[14] This same distinction is expected to hold for metallic liquids and, therefore, to serve as a criterion for the existence or nonexistence of complexes in metallic liquids.

Accordingly, the ultrasonic absorption spectra of liquid metallic systems claimed to contain complex molecules are being determined. Three such systems that have been examined are Hg-50 at. % In,[15,16] In-33 at. % Bi,[17] and Hg-18 at. % Na.[18] Figure III-12 shows for each alloy the variation of the coefficient of absorption per wavelength ($\alpha\lambda$) with frequency between 45 and 165 MHz. Over this frequency range, no maxima are apparent and no support is given to the concept that complexes form in these systems. However, they are not precluded because of the possibility that $\alpha\lambda$ may peak at frequencies higher or lower than those studied. Hence in future measurements, as the search for complexes continues, a considerably broader range of frequencies will be employed, namely, 1 MHz to 1 GHz.

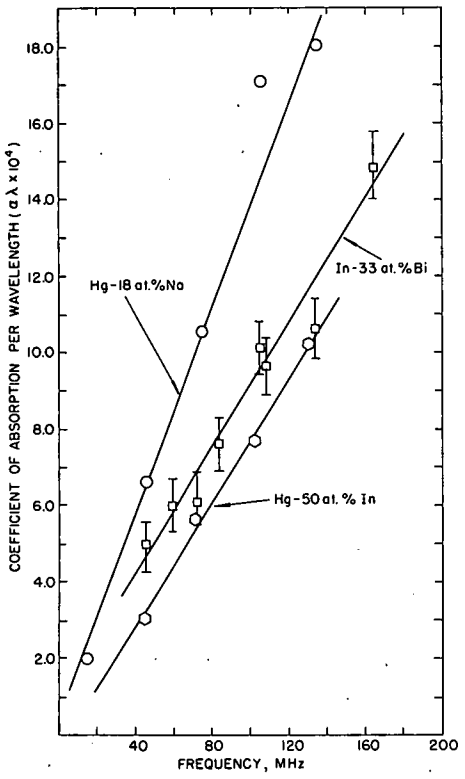


Fig. III-12. Absorption Coefficient per Wavelength Versus Frequency for Hg-Na, Hg-In, and In-Bi Alloys. (The magnitude of the errors for the mercury alloys is approximately the same as that shown for In-33 at. % Bi.)

## 5. Thermodynamic Properties of Liquid Na-Cs Alloys

Under existing technology, fission products in a reactor may find their way into coolant sodium only by accident. However, should vented fuel, now only a concept, be adopted in the future, fission products will find their way into the coolant by design. In both situations, the availability of thermodynamic information, such as Henry's law constants, can be helpful in understanding the behavior of fission products and in devising methods for their removal. Accordingly, a program to obtain such information for selected fission products has started.

The fission product cesium was selected for study because of fundamental interests in the Na-Cs system. Activities in the Na-Cs system are being measured by the technique of vapor-phase atomic absorption

[14] K. Tamm, G. Kurtze, R. Kaiser, Acustica 4, 380 (1954).
[15] N. Sundén, Z. Elektrochem. 57, 100 (1953).
[16] E. W. Collings, Advan. Phys. 16, 459 (1967).
[17] G. B. Styles, Advan. Phys. 16, 275 (1967).
[18] B. W. Mott, M. E. Downey, P. A. Cumming, UK Atomic Energy Authority Report AERE-Bib 151 (September 1966).

spectrophotometry. Resonance radiation characteristic of one of the alkali metals (the 5890 Å line for sodium, the 8521 Å line for cesium) is beamed through the vapor over the pure alkali metal and over the alloys. The absorption is a measure of the partial pressure of monomeric alkali metal in the vapor. Comparison of the absorption by the alloy ($p_i$) with that by the pure metal ($p_i^\circ$) yields the activity ($a_i = p_i/p_i^\circ$) of the metal in the alloy.

Direct experimental determinations of cesium activity in Na-Cs alloys containing ~1 at. % Cs have not yet been completed because of experimental difficulties. Meanwhile, because the Gibbs-Duhem equation can be used to deduce the Henry's law constant for cesium (although the error is large) from the sodium activities, the latter are being measured. Sodium activities in several Na-Cs alloys have been determined at ~140°C. Figure III-13 shows the results and, for comparison, the similarly obtained activity data for Na-Rb and Na-K alloys. Significant positive departures from ideality are evident; however, the departures are smaller than those for the Na-Rb system but larger than those for the Na-K system. It is noteworthy that the heats of mixing for the three systems vary in the same way.[19]

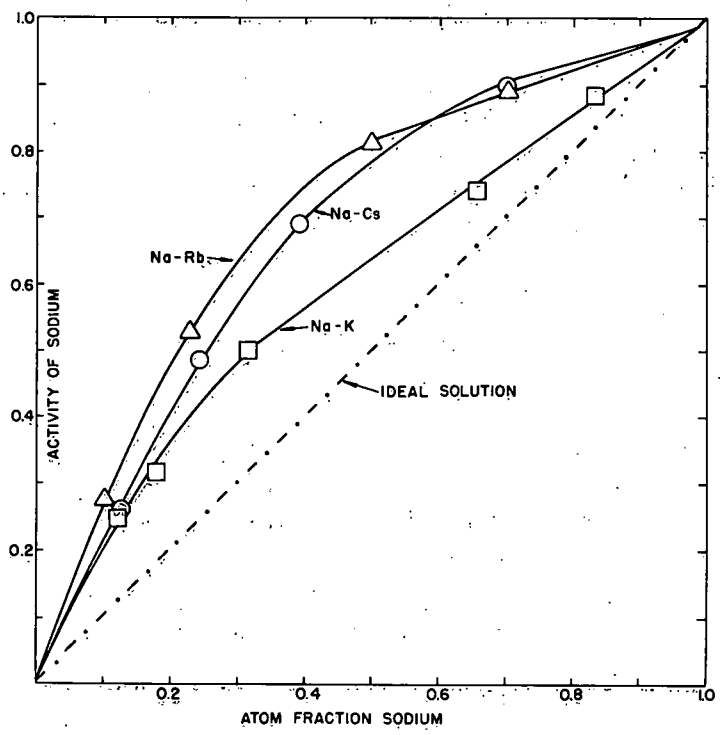


Fig. III-13

Variation of Sodium Activity with Composition of Liquid Alkali Metal Alloys at ~140°C.

[19] T. Yokokawa, O. J. Kleppa, J. Chem. Phys. 40, 46 (1964).

# IV. ENERGY CONVERSION

The use of electrochemical cells and systems for the conversion of thermal energy to electrical energy and for the storage of electrical energy continues to be an area of potential importance in the effective use of nuclear and radioisotopic energy. The cells and the corresponding systems of special interest in our research can be divided into two groups: those having lithium anodes and those having sodium anodes. The variety of systems and range of requirements for the cells have made it necessary to carry out a broadly based research program to provide the required thermodynamic, electrochemical, and physicochemical data.

The research program of the energy conversion group for the period 1961-1966 has been summarized in a topical report, ANL-7316. Subsequent work has been reported in ANL-7375, pp. 160-175; ANL-7425, pp. 172-189; ANL-7450, pp. 92-104; and in the open literature.[1-5]

## A. Cells with Lithium Anodes

Thermally regenerative and secondary cells with lithium anodes continue to be attractive for a range of possible applications from topping units and off-peak energy storage devices to specialty power sources for space, military, industrial, and, perhaps ultimately, consumer applications. The research program has continued to gather the needed thermodynamic and electrochemical information necessary for the choice of the best systems, designs, and operating conditions for these applications.

### 1. Thermodynamics of the Lithium-Tin System by the Vapor-Liquid Equilibrium Method; the Lithium/Tin Thermally Regenerative System

The lithium-tin system is being investigated for application in a thermally regenerative galvanic cell. The rational design of a regenerator requires knowledge of the liquid-vapor equilibrium. Thus, the vapor pressures and vapor-phase compositions for the lithium-tin system were determined for the full composition range at 1200°C (a likely regeneration temperature) and for selected compositions at lower temperatures.

---

[1] E. J. Cairns, H. Shimotake, "High Temperature Batteries," Science (in press).

[2] V. A. Maroni, E. J. Cairns, "A Review of Raman Spectroscopy of Fused Salts and Studies of Some Halide-Containing Systems," Abstracts of Papers, 156th Amer. Chem. Soc. Mtg., Atlantic City, New Jersey, September 8-13, 1968, ANAL-30.

[3] H. Shimotake, G. L. Rogers, E. J. Cairns, "Secondary Cells with Lithium Anodes and Immobilized Fused-Salt Electrolytes," Ind. Eng. Chem. Process Des. Develop. 8, 51 (1969).

[4] H. Shimotake, E. J. Cairns, "A High Rate Lithium/Selenium Secondary Cell with a Fused-Salt Electrolyte," Comité Intern. de Thermodynamique et de Cinetique Electrochemiques, Intern. Union Pure and Appl. Chem., 19th Meeting, Detroit, September 23-27, 1968. Extended Abstracts, pp. 254-258.

[5] H. Shimotake, E. J. Cairns, "A Lithium/Tin Cell with an Immobilized Fused-Salt Electrolyte: Cell Performance and Thermal Regeneration Analysis," Intersoc. Energy Conversion Eng. Conf. 1968 Record, pp. 76-91, IEEE, New York, 1968.

The data were collected mainly by transpiration techniques.[6] Where the behavior of lithium-rich mixtures made the transpiration method impractical, a boiling point method was used to obtain the total vapor pressure.

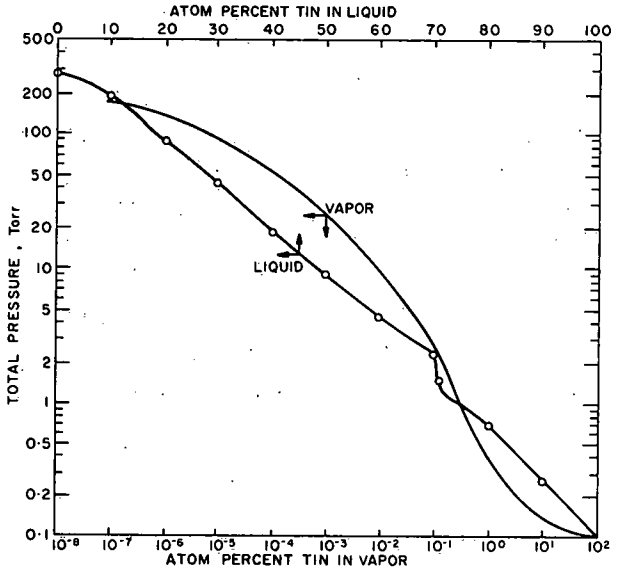


Fig. IV-1. Pressure-Composition Phase Diagram for Lithium-Tin System at 1200°C.

The data from the transpiration experiments at 1200°C have been plotted in Fig. IV-1 as a pressure-composition diagram, and the activity coefficient curves are shown in Fig. IV-2. The tin vapor pressures and the tin content of the vapor were calculated from the tin activity coefficients obtained by a Gibbs-Duhem integration. Figure IV-1 provides useful information for regenerative cell design, e.g., a cathode alloy with 60 at. % lithium has a total vapor pressure of 18.8 Torr and a vapor composition of $2.5 \times 10^{-3}$ at. % tin at 1200°C.

A series of low-temperature transpiration experiments was performed to determine the critical pressure below which solid will deposit in the regenerator and interfere with cell operation. Experiments were performed at four compositions: 79, 81, 85.5, and 90 at. % lithium. With the first three compositions, the

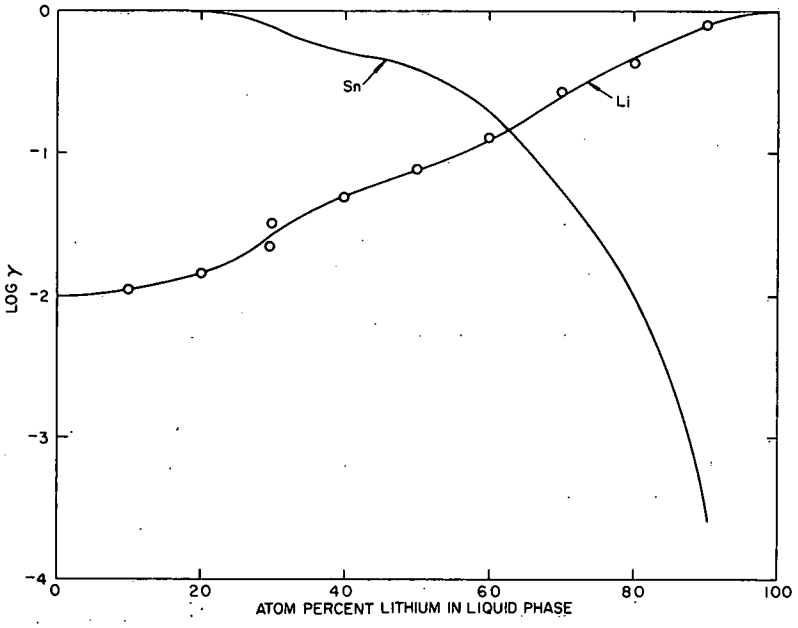


Fig. IV-2
Activity Coefficients for Lithium-Tin System at 1200°C.

[6] The apparatus for the high-temperature transpiration experiments is an adaptation of the apparatus shown in Fig. 71 of ANL-7316 (p. 112); the low-temperature transpiration technique is described in ANL-7055 (p. 222).

system contained solid as well as liquid and vapor. By extrapolating the transpiration data for each composition to the melting temperature (determined from the phase diagram), the pressure that defines the limit between liquid-vapor and liquid-vapor-solid equilibrium was found to be 0.41-0.42 Torr. Consequently, a lithium/tin thermally regenerative galvanic cell should be operated at pressures greater than 0.42 Torr.

Engineering studies of a lithium/tin thermally regenerative cell are also in progress. Performance data have been obtained for lithium/tin cells with immobilized (paste) electrolytes operating under various conditions (see Section IV.A.6.b of this report). Figure IV-3 shows typical voltage-current density curves for these cells. Because the partial pressure of lithium is low under regeneration conditions (0.42 Torr, minimum), special regenerator designs will be required for the lithium/tin system. An integrated cell-regenerator system design has been conceived; mathematical analysis of the mass and energy transport processes occurring in this regenerator is reported elsewhere.[5]

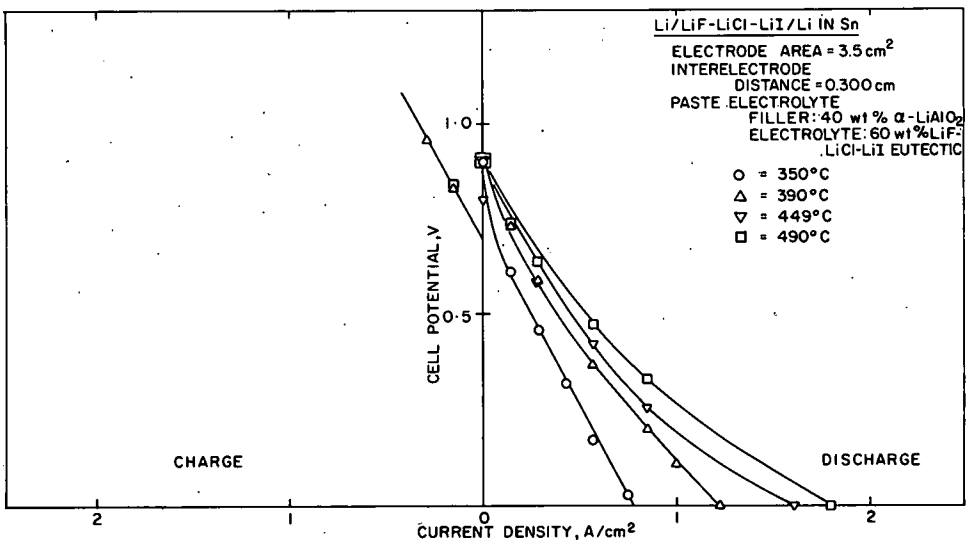


Fig. IV-3. Voltage-Current Density Curves for a Lithium/Tin Cell.

## 2. Phase Equilibrium Studies of the Lithium-Tellurium System

The solid-liquid equilibria in the lithium-tellurium system have been defined by thermal analysis and X-ray diffraction studies. The crystallization temperatures obtained from thermal analysis experiments are shown in Table IV-1. The compositions shown were obtained by chemical analysis.

Several lithium-tellurium alloys, prepared by direct combination of the elements and then annealed, were examined by X-ray diffraction. The results, also shown in Table IV-1, indicate the presence of a compound,

possibly $LiTe_3$, that has a body-centered cubic structure with a lattice constant of 6.162 Å. Although an alloy of exact 1:3 stoichiometry has not been examined, the X-ray pattern of the new phase, which is strongest at 78 at. % tellurium, suggests this stoichiometry. Also, the characterization of this phase as $LiTe_3$ is consistent with the observations of emf experiments and of X-ray patterns of other lithium-tellurium alloys. Therefore, $Li_2Te$ and $LiTe_3$ are assigned as the two compounds of lithium and tellurium in alloys containing more than 33 at. % tellurium.

TABLE IV-1. Results of Thermal Analysis and X-Ray Diffraction Studies of the Lithium-Tellurium System

| Composition (at. % Te) | Crystallization Temperature[a] (°C) | | X-Ray Diffraction Analysis of Annealed Alloy[b] |
|---|---|---|---|
| | Liquidus | Eutectic | |
| 94.6 | 442.9 | 423.7 | Te |
| 85.0 | 451.7 | 424.2 | - |
| 82.0 | - | - | "$LiTe_3$" major phase, Te intermediate |
| 77.9 | 467.0 | 427.1 | "$LiTe_3$" major phase, Te very minor |
| 70.0 | (none observed) | 453.3 | - |
| 43.0 | - | - | $Li_2Te$ major phase, "$LiTe_3$" very minor |

[a]From slow heating curves.
[b]After annealing at 350°C for 28 days.

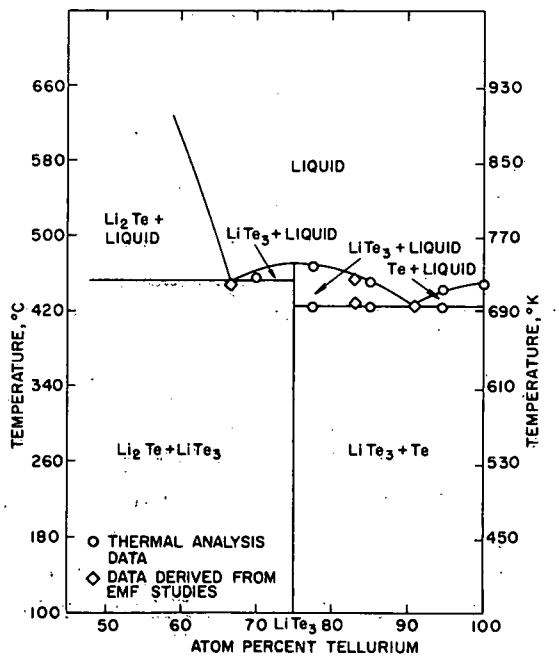


Fig. IV-4. Tellurium-Rich Portion of Lithium-Tellurium Phase Diagram.

The lithium-tellurium phase diagram from 50 to 100 at. % tellurium is presented in Fig. IV-4. The phase diagram shows that the cathode alloy in a lithium/tellurium cell operating at 480-500°C can contain up to about 35 at. % lithium before solid $Li_2Te$ will precipitate. At higher compositions of lithium, solid $Li_2Te$ will be formed in the cathode and must be redissolved during recharge of the cell.

### 3. Phase Equilibrium Studies of Lithium Halide-Containing Electrolytes

Phase diagram studies of lithium halide-containing fused-salt electrolytes have been extended to systems with more than one cation (see ANL-7425, p. 176). Results for the

LiCl-LiI-KI system have been obtained using guidance from phase diagrams calculated from the conformal ionic solution theory.[7] The advantage of this theory is that with a minimum of information (the melting point, heat of fusion, standard Gibbs free energy of formation for each component, and the eutectic temperature of each of the four nonreciprocal pairs in the system), the complete liquidus surface for the system can be computed.

The LiCl-LiI-KI system had been chosen for further investigation because preliminary experiments indicated that this system had a minimum melting point of 264°C, one of the lowest observed for ternary alkali halide mixtures.

Eight thermal analysis experiments were performed on the LiCl-LiI-KI system using apparatus and techniques that have been described elsewhere.[8] These experiments provided solid-liquid equilibrium data (Table IV-2) for three pseudo-binary mixtures which traversed the predicted minimum temperature-compositional regime.

TABLE IV-2. Crystallization Temperatures for the LiCl-LiI-KI System

| Series I Mole Ratio LiCl:LiI 1:1 | | Series II Mole Ratio LiCl:LiI 3:7 | | Series III Mole Ratio LiI:KI 6:4 | |
|---|---|---|---|---|---|
| mol % KI | Temperature (°C) | mol % KI | Temperature (°C) | mol % LiCl | Temperature (°C) |
| 30.0 | 399.5 | 20.0 | 341.3 | 20.0 | 330.0 |
| 35.0 | 392.1 | 25.0 | 338.0 | | |
| 47.3 | 436.8 | 31.5 | 330.0 | | |
| | | 38.3 | 346.1 | | |

A contour diagram of the liquidus isotherms for the ternary LiCl-LiI-KI system, given in Fig. IV-5, was constructed from the pseudo-binary data of Table IV-2 and data for the three binary component systems. Superimposed on the figure, as dashed lines, are the isotherms predicted by the conformal ionic solution theory. The experimental data indicated that the minimum temperature in the system, 265°C, was at 8.5 mol % LiCl, 59 mol % LiI, 32.5 mol % KI. The theoretical calculations predicted a minimum temperature of 276°C at a composition of 6 mol % LiCl, 62 mol % LiI, 32 mol % KI. Since this agrees quite well with the experimental work, it is clear that the conformal ionic solution theory offers significant saving of experimental effort in the selection of low-melting electrolyte mixtures. Cesium- and rubidium-containing systems are among those to be investigated using this approach.

[7]M. Blander, S. J. Yosim, J. Chem. Phys. 39, 2610 (1963); see also ANL-7425, p. 176.
[8]C. E. Johnson, C. E. Crouthamel, S. E. Wood, Inorg. Chem. 3, 1487 (1964).

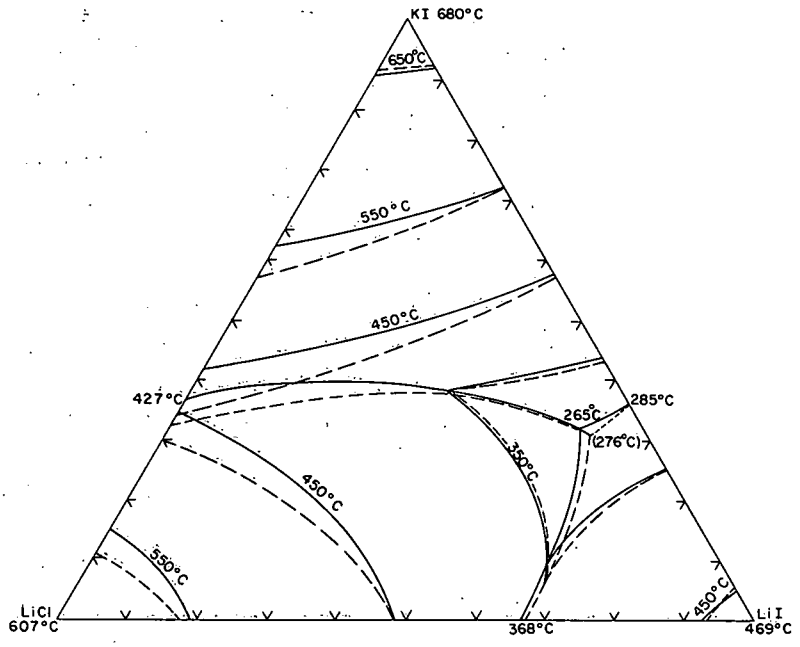


Fig. IV-5

Solid-Liquid Equilibrium Data for the LiCl-LiI-KI System (solid curves: experimental; dashed curves: conformal ionic solution theory).

## 4. Raman Spectroscopy of Halide-Containing Systems

Raman spectroscopy is being used to characterize the species present in halide-containing fused salts. The systems $Li_2Se$-LiF-LiCl and $Li_2Te$-LiF-LiCl were examined by this technique. Spectra of 5-10 mol % $Li_2Se$ or $Li_2Te$ in the LiF-LiCl eutectic did not contain bands that could be attributed to selenium- or tellurium-containing species. It was concluded from these studies that $Li_2Se$ and $Li_2Te$ dissociate in alkali halide melts. Further evidence for the ionic nature of lithium selenide was obtained previously in a study of the infrared spectrum of solid $Li_2Se$ as a function of pressure (see ANL-7450, p. 102).

A study of complex formation in $MgCl_2$-containing fused salt systems that are pertinent to compact pyrochemical processes has also been carried out by means of Raman spectroscopy.[9] Molten samples of $MgCl_2$ in various proportions with KCl were examined to determine the effect on the Mg-Cl vibrational bands of varying the $Cl^-/Mg^{+2}$ mole ratio. Spectra obtained for $Cl^-/Mg^{+2}$ ratios in the range 2.5 to 4.0 all show a strong polarized band in the region of 200 to 300 $cm^{-1}$ and a broad depolarized band centered near 160 $cm^{-1}$. The spectrum for an $MgCl_2$-KCl melt with $Cl^-/Mg^{+2}$ = 4.0, shown in Fig. V-13 of ANL-7450, p. 101, is typical of the results obtained for the entire series of compositions. As the $Cl^-/Mg^{+2}$ ratio is increased from 2.5 to 4.0, the position of the maximum of the polarized band shifts continuously to higher frequencies.

These results suggest that a complex equilibrium, which involves several structurally different species, exists in $MgCl_2$-containing melts. This equilibrium was studied in detail by subjecting the series of

[9] This portion of the work was performed in cooperation with the CEN Pyrochemical Research Group. Preliminary studies of $MgCl_2$-containing salt systems were reported in ANL-7450, p. 101.

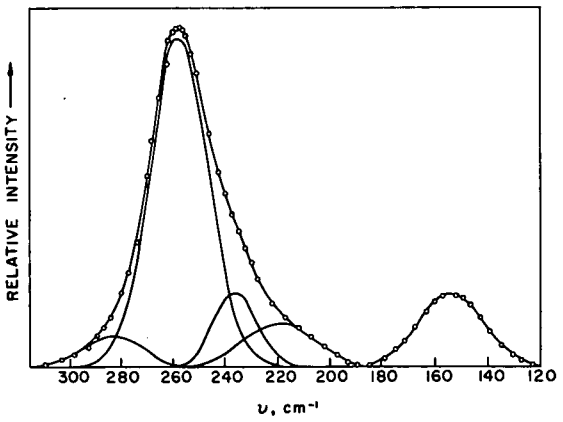


Fig. IV-6

Resolved Raman Spectrum of $MgCl_2$-KCl at 550°C, $Cl^-/Mg^{+2}$ = 4.0. (Points represent the recorded spectrum; solid lines, the computer-resolved Gaussian peaks and total calculated intensity curve.)

$MgCl_2$-KCl spectra to a computerized Gaussian-curve resolution analysis.[2] The analysis of the spectrum for the melt with $Cl^-/Mg^{+2}$ = 4.0 is shown in Fig. IV-6, and results for the entire series of compositions are summarized in Table IV-3.

The four bands at 282, 251, 234, and 217 $cm^{-1}$, which constitute the completely polarized envelope at 200-300 $cm^{-1}$, probably arise from species of the type $MgCl_n^{(2-n)}$ or from the solid-like lattice structure $(MgCl_2)_n$ persisting into the melt phase. A continuous-variations study of the integrated intensities for these resolved bands indicates that the bands at 234 and 217 $cm^{-1}$ are due to symmetric stretching vibrations of polymeric $(MgCl_2)_n$ units, and that the bands at 282 and 251 $cm^{-1}$ arise from the totally symmetric stretching vibrations of $MgCl_3^-$ and $MgCl_4^{-2}$, respectively. The intensity of the band at 163 $cm^{-1}$ was relatively invariant over the range of the continuous-variations plot; therefore, this band has been attributed to a composite of bond-bending vibrations for $MgCl_3^-$, $MgCl_4^{-2}$, and the polymeric lattice structure.

TABLE IV-3. Summary of Curve-Resolution Data for $MgCl_2$-KCl System

| Frequency ($cm^{-1}$) at Indicated $Cl^-/Mg^{+2}$ Ratio[a] | | | | Average Frequency[b] ($cm^{-1}$) | Assignment |
|---|---|---|---|---|---|
| 4.0 | 3.6 | 3.0 | 2.5 | | |
| 283 (0.6) | 277 (0.3) | 287 (0.3) | - | 282 ± 5, p | $\nu_1(A_1')$ $MgCl_3^-$ |
| 257 (5.9) | 257 (0.8) | 254 (0.6) | 245 (0.3) | 251 ± 6, p | $\nu_1(A_1)$ $MgCl_4^{-2}$ |
| 236 (1.0) | 238 (1.0) | 227 (1.0) | 241 (1.0) | 234 ± 7, p | $(MgCl_2)_n$ polymer |
| 219 (1.0) | 220 (0.6) | 224 (0.6) | 210 (0.4) | 217 ± 7, p | $(MgCl_2)_n$ polymer |
| 158 (3.2) | 158 (0.6) | 168 (0.5) | 167 (0.3) | 163 ± 5, dp | Cl-Mg-Cl bending modes |

[a]Numbers in parentheses indicate intensity relative to 234 ± 7 $cm^{-1}$ band.
[b]The average frequencies are used in the text to identify the bands; p = polarized, dp = depolarized.

The Raman spectrum of $UO_2^{+2}$ in $MgCl_2$-KCl-NaCl eutectic and the effect of dissolved $UO_2Cl_2$ on the magnesium (II)-chloride complex equilibrium have also been investigated. The spectrum of 1.5 M $UO_2Cl_2$ in $MgCl_2$-KCl-NaCl eutectic (uranium/magnesium mole ratio = 0.18) at 600°C

is shown in Fig. IV-7. The band at 850 $cm^{-1}$ is the totally symmetric stretching vibration characteristic of $UO_2^{+2}$.[10] The broad band centered near 205 $cm^{-1}$ is assigned to vibrations of the various magnesium (II)-chloride species; as the uranium/magnesium mole ratio is increased, this band shifts continuously to lower frequencies. From the direction of the shift, it appears that $UO_2^{+2}$ is complexing some of the chlorine atoms that give rise to the higher frequency vibrations in the region from 200 to 300 $cm^{-1}$. Therefore, the band at 267 $cm^{-1}$ is assigned to vibrations associated with a structure having uranium-chlorine-magnesium bridges.

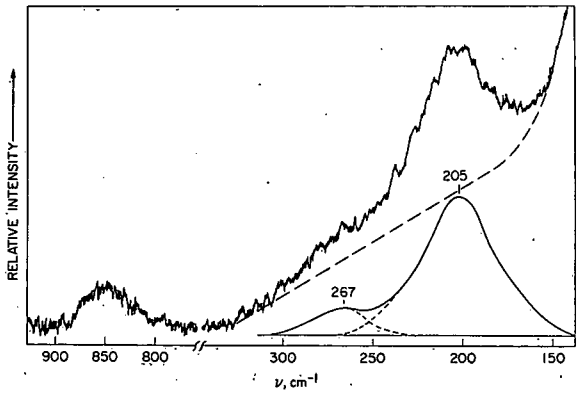


Fig. IV-7. Raman Spectrum of 1.5 M $UO_2Cl_2$ in $MgCl_2$-KCl-NaCl Eutectic at 600°C (uranium-to-magnesium mole ratio = 0.18).

These studies may be extended to determine the effect of the structure of the fused salt phase on distribution coefficients of various dissolved species between a fused-salt phase and one or more liquid metal phases.

A Raman study has been made of complex formation in molten $MgBr_2$-KBr mixtures as a function of the $Br^-/Mg^{+2}$ ratio for compositions having $Br^-/Mg^{+2}$ ratios ranging from 2.5 to 5.0. All of the spectra show a strong polarized band in the region of 125-175 $cm^{-1}$ and a broad weak band centered near 90 $cm^{-1}$. The interpretation of the data for this system is analogous to that for the MgCl-KCl system, that is, the magnesium-bromide stretching modes are in the 125-175 $cm^{-1}$ region, and the bending modes are at about 90 $cm^{-1}$.

A normal coordinate analysis of the $Al_2Cl_6$ vapor-bridged dimer has been performed[11] based on our recent gas phase Raman data and gas phase infrared data of Klemperer.[12] The analysis had not been possible previously because the Raman spectrum of the vapor had been lacking. The work has been published in full elsewhere.[13]

[10] G. K. T. Conn, C. K. Wu, Trans. Faraday Soc. 34, 1483 (1938).

[11] This portion of the work was performed in cooperation with D. Gruen and R. McBeth of the ANL Chemistry Division.

[12] W. Klemperer, J. Chem. Phys. 24, 353 (1956).

[13] V. A. Maroni, D. M. Gruen, R. L. McBeth, E. J. Cairns, "Raman Spectrum and Vibrational Analysis for Gaseous Aluminum Chloride," Inorg. Chem. (in press).

## 5. Lithium/Chalcogen Secondary Cells

Recent interest in high-specific-energy (W-hr/lb), high-specific-power (W/lb) sources of electricity has fostered research and development work on secondary cells that promise characteristics of power and energy superior to those of currently available cells. Studies at Argonne have indicated that lithium/sulfur and lithium/phosphorus cells possess these characteristics.

### a. Lithium/Sulfur Cells

Two types of experimental lithium/sulfur cells have been studied: a cell with a liquid electrolyte and a cell with a paste electrolyte.

The first cell employed a molten salt electrolyte (26 mol % LiCl, 54 mol % LiI, 20 mol % KI) held in an alumina crucible. The cathode consisted of an iron cup that contained sulfur and twelve layers of expanded Armco iron mesh, the latter aiding in current collection. The anode current collector consisted of concentric rings of corrugated stainless steel sheet and was prewetted with lithium at 400°C. In the fully discharged condition, the ratio of lithium to sulfur corresponded to a cathode alloy composition of 33 at. % lithium in sulfur. The cell was operated under a helium atmosphere at 347°C. The maximum capacity of the cell was 5.7 A-hr.

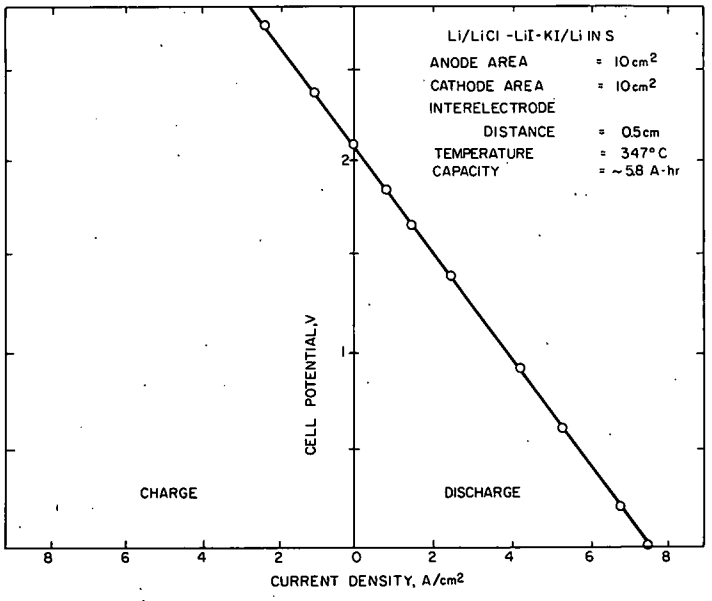


Fig. IV-8. Voltage-Current Density Curve for a Lithium/Sulfur Cell.

The short-term voltage-current density curve for this cell at a temperature of 347°C is shown in Fig. IV-8. An open-circuit voltage of 2.1 V and a short-circuit current density of 7.5 A/cm$^2$ were obtained. The cell was charged between experiments in which the discharge data were obtained. After 18 hr of operation, the iron mesh current collector was found to be dissolved in the sulfur. (Recent tests show tantalum or niobium current collectors to be suitable.)

The experimental lithium/sulfur cell with a paste electrolyte was constructed of type 304 stainless steel and had electrodes of 3.8-cm$^2$ area. The paste electrolyte consisted of a mixture of 26 mol % LiCl, 54 mol % LiI, 20 mol % KI and an inert ceramic powder in a one-to-one weight ratio.

Special care was taken in constructing the cathode to minimize electronic resistivity. The molten sulfur was mixed with graphite powder (which served as a current collector) at 150°C under a helium atmosphere. The resulting 75 wt % sulfur, 25 wt % carbon mixture formed a plastic paste with a specific resistance at room temperature of about 75 ohm-cm. The mixture was pressed into the cathode compartment in five layers with sheets of expanded stainless steel mesh separating the layers. The anode compartment contained lithium without any current collectors.

This cell, which was operated at 310°C, yielded an open-circuit voltage of 2.2 V and a short-circuit current density of 0.67 A/cm$^2$. The cell resistance was 0.9 ohm. Such a high resistance means that carbon is not a satisfactory current collector. In future experiments, other methods of current collection will be investigated.

b. Lithium/Phosphorus Cell

An experimental lithium/phosphorus cell with a liquid electrolyte of LiF-LiCl-LiI eutectic has been operated from 374 to 425°C under a helium atmosphere. The cathode consisted of an Armco iron cup with an effective cathode area of 10 cm$^2$ and contained several layers of expanded Armco iron mesh to aid in current collection. The cathode material was a 50 at. % lithium, 50 at. % phosphorus mixture prepared by successive additions of red phosphorus to liquid lithium at 200°C. The anode, also 10 cm$^2$ in area, consisted of two concentric rings made from corrugated stainless steel sheet, prewetted with lithium.

The open-circuit voltage of this cell ranged from 0.89 V at 374°C to 0.875 V at 425°C. The maximum short-circuit current density observed was 1.7 A/cm$^2$. The corresponding cell resistance was 0.052 ohm, as compared with a theoretical value of 0.013 ohm.

An open-circuit voltage of about 1.3 V was observed at 386°C after charging the cell for over 2 A-hr; at this point the cathode composition was 29 at. % lithium and 71 at. % phosphorus. On slow discharge ($<0.5$ A), the cell maintained a voltage plateau of 1.3 V for about 40 min; the voltage then dropped rather quickly to another plateau at 0.98 V. The plateau at 1.3 V is attributed to the P-$Li_2P_5$ equilibrium, whereas the plateau at 0.98 V is attributed to the $Li_2P_5$-$Li_3P$ equilibrium.

More experiments are planned with the lithium/phosphorus cell; however, a different type of current collector will be used to improve the current density. Although the anticipated cell performance was not attained in this preliminary experiment, the advantages of a lithium/phosphorus cell, e.g., low mass, low cost, and good availability of phosphorus, warrant further experimental work.

### c. Performance Comparison

To put the capabilities of the various cells studied into perspective, the performance data presented above, along with data for Li/Se and Li/Te,[3,4,14] are summarized in Table IV-4. (The data given for the Li/S cell with paste electrolyte in this table are the results of preliminary experiments; considerably better results are anticipated.) These performance data were used, together with the battery design shown in Fig. IV-9, to calculate the expected performance for fully engineered batteries with paste electrolytes. The calculations (based on a 10-min rate for specific power and a 1-hr rate for specific energy) indicate the following: a Li/Te battery would have a specific power of 250 W/lb and a specific energy of 90 W-hr/lb; a Li/Se battery would have a specific power of 380 W/lb and a specific energy of 130 W-hr/lb; and a Li/S battery would have a specific power of 500 W/lb and a specific energy of 160 W-hr/lb. The characteristics for these three types of secondary batteries are compared with those for some others in Fig. IV-10.

Some of the applications that could be considered for a practical lithium/chalcogen battery include power for spacecraft, military communications, materials handling vehicles, military vehicles, boats and submarines, remote locations, buses and trucks, urban automobiles, and

TABLE IV-4. Summary of Performance Data for Lithium/Chalcogen Cells

Cells with Liquid Electrolytes

| Cell | Open-Circuit Voltage (V) | Short-Circuit Current Density ($A/cm^2$) | Maximum Power Density ($W/cm^2$) | Temperature (°C) |
|---|---|---|---|---|
| Li/Te | 1.75 | 8 | 3.5 | 470 |
| Li/Se | 2.3 | 11 | 6.3 | 365 |
| Li/S | 2.1 | 7.5 | 3.9 | 347 |
| Li/P | 0.89 | 1.7 | 0.38 | 374 |

Cells with Paste Electrolytes

| Cell | Open-Circuit Voltage (V) | Short-Circuit Current Density ($A/cm^2$) | Maximum Power Density ($W/cm^2$) | Temperature (°C) | Resistivity Ratio[a] |
|---|---|---|---|---|---|
| Li/Te | 1.75 | 2.1 | 0.96 | 475 | 7.6 |
| Li/Se | 2.3 | 4.0 | 2.7 | 375 | 3.9 |
| Li/S | 2.2 | 0.67 | 0.37 | 310 | -[b] |

[a]Resistivity of the paste divided by the resistivity of the pure fused-salt electrolyte.
[b]The resistivity was not calculated because part of the electrolyte was solid.

[14]H. Shimotake, G. L. Rogers, E. J. Cairns, "Performance Characteristics of a Lithium-Tellurium Cell," presented at the Electrochem. Soc. Meeting, Chicago, Illinois, Oct. 15-19, 1967 (see extended abstracts of the Battery Div.); also, ANL-7450, pp. 92-100.

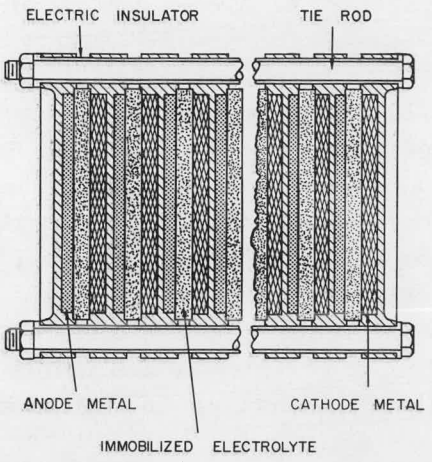


Fig. IV-9. Design of Lithium/Chalcogen Battery with Immobilized (Paste) Electrolyte.

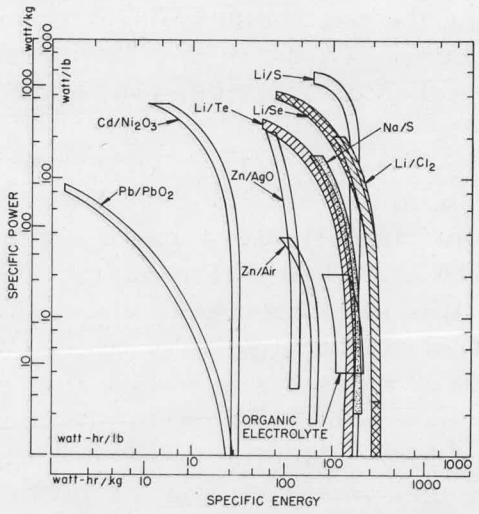


Fig. IV-10. Specific Energy-Specific Power Characteristics of Various Batteries.

off-peak energy storage for central stations. (This list is arranged in a possible order of higher-probability applications first.)

6. Immobilization of Lithium Halide Electrolytes: Paste Electrolyte Preparation and Properties

An important phase of the development of practical cell configurations is the immobilization of one or more of the three liquid phases. Recently, a program was initiated with the goal of understanding and optimizing the immobilization of the electrolyte phase by using disks of paste electrolyte. The filler that is being studied at the present time is meta-lithium aluminate, $LiAlO_2$, which appears to have the important property of being stable toward molten lithium. Other important factors are particle size and shape, since these influence the strength and rheological properties of the disk.

Two crystalline modifications of $LiAlO_2$ are known: a low-temperature, high-density $\alpha$ form (3.4 $g/cm^3$) and a high-temperature, low-density $\gamma$ form (2.6 $g/cm^3$). The conditions necessary for the preparation of $LiAlO_2$ in either the pure $\alpha$ or the pure $\gamma$ form are being investigated. Synthesis of $LiAlO_2$ from $Al_2O_3$ and $Li_2CO_3$, either in the presence or absence of $Na_2CO_3$, yielded $\alpha$-$LiAlO_2$ at temperatures below 625°C, and $\gamma$-$LiAlO_2$ at temperatures above 625°C.

Powdered filler materials that were either prepared as described above or obtained commercially were combined (by grinding, heating, and regrinding) with a powdered mixture of LiF-LiCl-LiI eutectic and hot-pressed into paste electrolyte disks. The electrochemical properties of these paste electrolytes were determined by testing the performance of lithium/tin cells that incorporated the pastes. The cell used for

testing the paste electrolytes consisted of a 2.5-cm dia paste electrolyte disk between 2.2-cm dia lithium and tin electrodes. Cell performance data were taken at 350, 400, 450, and 500°C.

The data from the paste electrolyte disks tested to date are presented in Table IV-5. (A typical voltage-current density curve for the lithium/tin cell with a paste electrolyte was shown in Fig. IV-3 in Section IV.A.1 of this report.) Thus far, the highest short-circuit current densities have been achieved with a paste electrolyte made of 60 wt % electrolyte-40 wt % GK-2 ($\alpha$-$LiAlO_2$). Further tests now under way may result in a paste electrolyte that shows even higher current densities. A reasonable goal is a paste electrolyte having a resistivity 2.5 times that of the corresponding fused salt with no filler, and having sufficient strength to be used in sheets about 2 mm thick.

TABLE IV-5. Properties of Paste Electrolyte Disks

| Electrolyte Concentration[a] (wt %) | Filler | Thickness (cm) | Density[b] ($g/cm^3$) | Durability | Wetting by Liquid Metals | Resistivity Ratio[c] at 400°C | Short-Circuit Current Density[d] at 400°C ($A/cm^2$) |
|---|---|---|---|---|---|---|---|
| 50 | GK-2: $\alpha$-$LiAlO_2$ | 0.465 | 1.69 | Brittle | - | - | - |
| | KD-15: $\gamma$- + $\alpha$-$LiAlO_2$ | 0.458 | 1.74 | Brittle | - | - | - |
| | Vitro: $\gamma$-$Al_2O_3$ | - | - | Brittle | - | - | - |
| | KD-7: $\gamma$-$LiAlO_2$ | 0.332 | 2.426 | Small crack | Good | 11.9 | 0.515 |
| | G&S: $\gamma$-$LiAlO_2$ | 0.338 | 2.42 | Soft | Good | 8.7 | 0.70 |
| | ESP: $\gamma$-$LiAlO_2$ | 0.335 | 2.389 | Satisfactory | Good | 8.55 | 0.715 |
| | KD-11: $LiAl_5O_8$ + minor $LiAlO_2$ | 0.317 | 2.53 | Satisfactory | Good | 5.45 | 1.18 |
| 60 | KD-15: $\gamma$- + $\alpha$-$LiAlO_2$ | 0.414 | 1.932 | Very strong | No (Sn) | - | <0.1 |
| | X: proprietary | 0.358 | 2.237 | Split, crack | No (Li) | 10.0 | 0.57 |
| | Vitro: $\gamma$-$Al_2O_3$ | 0.295 | 2.686 | Satisfactory | Good | 48.5 | 0.143 |
| | KD-9: $LiCO_3$ + $\gamma$-$Al_2O_3$ | 0.338 | 2.435 | Satisfactory | Good | 7.07 | 0.856 |
| | GK-2: $\alpha$-$LiAlO_2$ | 0.297 | 2.73 | Satisfactory | Very good | 3.72 | 1.58 |
| | GK-2: $\alpha$-$LiAlO_2$ | 0.297 | 2.73 | Satisfactory | Very good | 5.5 | 1.23 |
| 70 | KD-9: $LiCO_3$ + $\gamma$-$Al_2O_3$ | 0.312 | 2.588 | Soft | Satisfactory | 5.27 | 1.15 |

[a]LiF-LiCl-LiI eutectic.
[b]Calculated on basis of formula density: wt of paste/(circular area)(thickness).
[c]Ratio of the resistivity of the paste to the resistivity of the pure electrolyte; the resistivity of the pure electrolyte is 0.44 ohm-cm.
[d]Open-circuit voltages = 0.8 to 1.0 V (see Fig. IV-3); electrode area = 3.5 $cm^2$.

## B. Cells with Sodium Anodes

Cells with sodium anodes have been of particular interest in connection with thermally regenerative systems for use with heat sources having temperatures in the range 800 to 1000°C. The sodium-bismuth system has been thoroughly investigated using emf, vapor-liquid equilibrium, and thermal analysis methods. Recently, all of these data have been used in a detailed thermodynamic treatment of the results using the quasi-ideal solution theory. A portion of this treatment and some new results are presented below.

## 1. Thermodynamics of the Sodium-Bismuth System by an Emf Method

The quasi-ideal solution theory[15,16] has been used to correlate the thermodynamic properties of sodium-bismuth alloys as calculated from vapor-liquid equilibrium measurements by the transpiration and total pressure methods;[17] this discussion appeared in an earlier report (ANL-7350, p. 78). Application of this theory has now been extended to include emf data as a function of temperature and composition, as observed for cells of the type:

$$Na(\ell)/NaCl(s)/Na \text{ in } Bi(\ell).$$

The quasi-ideal solution theory, as applied to the sodium-bismuth system, assumes that the compounds $Na_3Bi$ and NaBi persist in the melt, and that the compound species, as well as Na and Bi, behave ideally. Experimental data obtained at 1173°K[17] were used to calculate the activity coefficients of sodium and bismuth as components of the sodium-bismuth system. More recently, the activity coefficient of sodium as a component was obtained from cell emf data as a function of temperature and composition of the liquid alloy (ANL-7375, p. 160). The emf data were obtained over the temperature range 550 to 1050°K. The composition of the alloy ranged between 40 and 90 at. % bismuth in sodium, although at the lower temperatures it was not possible to reduce the bismuth concentration below 70 at. % owing to the precipitation of the solid compounds NaBi or $Na_3Bi$.

The two parameters required for a description of the quasi-ideal sodium-bismuth system are the equilibrium constants for the formation of the species $NaBi(K_1)$ and $Na_3Bi(K_2)$. At a single temperature, these may be determined by a nonlinear least-squares technique using the observed activity coefficients of sodium and bismuth as components.

Plots of log $K_1$ and log $K_2$ as functions of reciprocal absolute temperature for emf and for vapor pressure measurements were both straight lines. The data were calculated by multiple regression for temperatures greater than 700°K. At lower temperatures, the smaller range of the bismuth concentration allowed only an estimation of $K_2$ by extrapolation and a calculation of $K_1$ using a single nonlinear least-squares technique.

The values of $K_1$ and $K_2$ were used to calculate the expected emf of the experimental cells. The standard deviation of the calculated emf values from the observed data was 10 mV, which is within the accuracy of the measurements. The calculated curves of the activity coefficients of

[15]E. Högfeldt, Arkiv Kemi 7, 315 (1954).
[16]E. Högfeldt, Rec. Trav. Chim. 75, 790 (1956).
[17]A. K. Fischer, S. A. Johnson, S. E. Wood, J. Phys. Chem. 71, 1465 (1967).

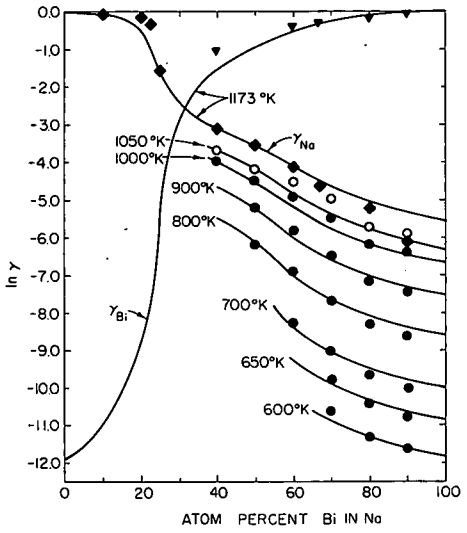


Fig. IV-11

Calculated and Observed Activity Coefficients in Sodium-Bismuth Alloys. (Calculated values were derived from the quasi-ideal solution theory.)

sodium and bismuth are compared with experimental data points in Fig. IV-11. Also included for comparison are the vapor pressure-transpiration measurements at 1173°K.[17]

The two parameters, $K_1$ and $K_2$, expressed as a function of temperature, were also used as the basis for calculating the equilibrium vapor composition and pressure above liquid sodium-bismuth alloys. At equilibrium, the activity of sodium as a species in the quasi-ideal solution is equal to its concentration. Also, the activity of sodium as a species in the solution is equal to the activity of Na monomer in the vapor phase in equilibrium with the solution. Assuming that the species in the gas phase behave ideally, the activity of Na monomer may be calculated as the ratio of its partial pressure over the solution to its partial pressure over pure sodium. Since the activity of Na monomer and its partial pressure over pure sodium are known, the partial pressure of Na monomer in the gas phase could be calculated. Similar reasoning can be applied to the Bi monomer.

The vapor above the liquid alloy was assumed to contain Na, $Na_2$, $Na_4$, Bi, and $Bi_2$, i.e., the species usually found or postulated to explain the behavior of pure sodium and pure bismuth vapors. The partial pressure of each of these species was calculated, and the sum was used as the total pressure over the solution.

The results are shown in Fig. IV-12 where the composition of the liquid and vapor phase is shown as a function of temperature for a total system pressure of 240 Torr. In addition, liquid-solid phase equilibrium data reported in the following subsection are shown for comparison. The proximity of the liquid-vapor loop to the liquid-solid curve should be noted. At lower pressures, overlap would occur, creating a solid-vapor region.

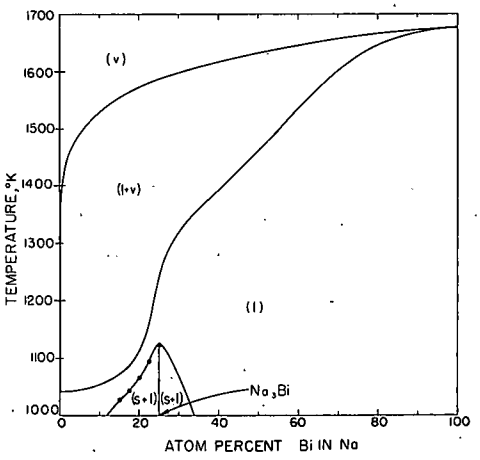


Fig. IV-12. Phase Relationships in the Sodium-Bismuth System for a Total System Pressure of 240 Torr.

The results presented above illustrate the usefulness of the quasi-ideal theory in the treatment of thermodynamic data for the sodium-bismuth system over a wide range of temperatures and over the

full composition range. The success of this treatment in the prediction of the vapor-liquid loop and other thermodynamic behavior is not offered as a proof of the existence of the species NaBi and $Na_3Bi$ in the liquid alloy. This question may best be answered by direct experimental observation.

## 2. Phase Equilibrium Studies of the Sodium-Bismuth System

In a report on the liquid-vapor equilibria for the sodium-bismuth system,[17] certain experimental results were discussed that indicated an error in the published sodium-bismuth phase diagram,[18] which was based on the work of Kurnakov and Kusnetzow[19] and Mathewson.[20] From the thermal analysis and solubility data reported herein, a more accurate phase diagram for the sodium-bismuth system has been constructed.

The apparatus and techniques for the thermal analysis study are described elsewhere;[8] they included the use of closed sample capsules for the sodium-rich half of the phase diagram and of open sample crucibles for the bismuth-rich half. In the solubility study,[21] equilibrated mixtures of solid $Na_3Bi$ and sodium were filtered and analyzed.

A sodium-bismuth phase diagram constructed from the thermal analysis and solubility data is presented in Fig. IV-13. The data for compositions between those examined in the thermal analysis studies and those of the solubility studies were obtained by Walker, Pratt, and Mott.[22] Our work indicates that the melting point of $Na_3Bi$ is 848.1°C, approximately 75° higher than the previously accepted value of 775°C.

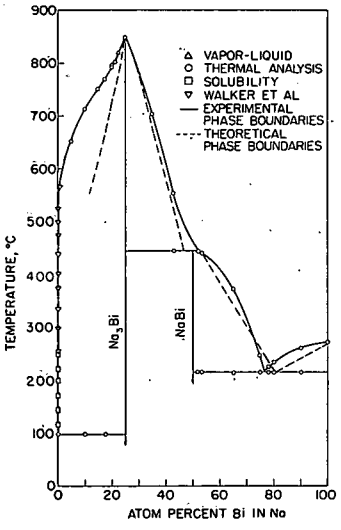


Fig. IV-13

Solid-Liquid Phase Diagram for the Sodium-Bismuth System. (Theoretical calculations made using the equation $\ln \frac{x_2}{x_1} = \frac{\Delta H}{R}\left(\frac{1}{T_2} - \frac{1}{T_1}\right)$ with the data: Bi, $T_m$ = 271.3°C and $\Delta H_m$ = 2600 cal/mol; NaBi, $T_m$ = 500°C and $\Delta H_m$ = 3600 cal/mol; $Na_3Bi$, $T_m$ = 848.1°C and $\Delta H_m$ = 11,100 cal/mol.)

---

[18] M. Hansen, K. Anderko, Constitution of Binary Alloys, p. 321, McGraw-Hill, New York (1958).

[19] N. S. Kurnakov, A. N. Kusnetzow, Z. Anorg. Chem. 23, 455 (1900).

[20] C. H. Mathewson, Z. Anorg. Chem. 50, 187 (1906).

[21] This problem was selected for study by the 1968 AUA-ANL Summer Engineering Practice School.

[22] R. A. Walker, J. N. Pratt, B. W. Mott, "The Solubility of Metallic Elements in Liquid Sodium," presented at the 1968 AEC Corrosion Symposium, Battelle Memorial Institute, Columbus, Ohio, May 6-8, 1968.

Walker et al[22] reported that for the temperature range from 252 to 563°C, the solubility of bismuth in sodium is given by the relationship

$$\log (\text{at. \% Bi in Na}) = 5.0038 - 4188.9/T \qquad (1)$$

from which the heat of solution of $Na_3Bi$ in sodium is calculated to be 19.17 ± 1.47 kcal/mol. In the temperature region 550-775°C, the heat of solution was previously deduced (ANL-7316, p. 74) from the solubility of $Na_3Bi$ in molten NaF-NaCl-NaI mixtures to be 10.7 kcal/mol.

The solubility data obtained in this study may be represented by the relationship

$$\log (\text{at. \% Bi in Na}) = 2.0266 - 2424.7/T. \qquad (2)$$

The solubilities are greater than would be expected from an extrapolation of Walker's data. The heat of solution of $Na_3Bi$ in sodium calculated from Eq. 2 is 11.1 ± 0.9 kcal/mol, a value that is smaller than that obtained by Walker. These results indicate that the system cannot be considered a simple ideal solution of $Na_3Bi$ in sodium. The more dilute solutions studied in our experiments should yield a better approximation for the heat of solution of $Na_3Bi$, because these solutions are presumably the more ideal.

In Fig. IV-13, theoretical phase boundaries have been plotted for comparison with the experimental data. Work continues in an attempt to find a more suitable model that will account for the behavior of this system.

The shape of the sodium-bismuth phase diagram is unusual in that there is a sharp peak at the congruent melting point of $Na_3Bi$ (25 at. % Bi). However, our sodium-bismuth phase diagram resembles the lithium-bismuth phase diagram, particularly in the area of this peak, if the latter is drawn strictly through the experimental points determined by Grube, Vössuhler, and Schlecht.[23] Just to the left of the peak, both curves show an upward concavity. To the right of the peak, the curves are initially concave downward and then inflect to concave upward. Similar characteristics can also now be recognized in the rubidium-bismuth and cesium-bismuth systems (data are sparse for the potassium-bismuth system), if literal curve fitting is done.

## C. Materials Stability

Because many of the systems of interest in the electrochemical energy conversion program represent couples having high reactivity, the materials-compatibility problem is a difficult one. The experimental

[23] G. Grube, H. Vössuhler, and H. Schlecht, Z. Electrochem. 40, 270 (1934).

program requires that apparatus be constructed of very stable materials to avoid contamination and corrosion and to allow thermodynamically meaningful results to be obtained. In addition, the construction of laboratory cells for power production requires that long lifetimes be achievable. A continuing program is being carried out to identify metallic and ceramic (insulator) materials that resist the corrosive action of molten alkali metals, fused alkali halides, and molten heavy metals or chalcogens.

1. Ceramic Materials

To have efficient utilization of space in cells and batteries, effective electrical insulators must be developed. Aluminum oxide ($Al_2O_3$) is suitable as an insulator material for cells or batteries containing sodium and sodium alloys. For cells containing lithium and its alloys, three double oxides, $LiAlO_2$, $Li_2ZrO_3$, and $CaZrO_3$, are being considered as insulators. To test the behavior of these double oxides in a quasi-cell environment, pellets of each were fabricated under varying conditions of (1) reactants, (2) particle size, (3) pressing force, and (4) sintering temperature, and then exposed to liquid lithium at temperatures ranging from ~400°C to ~550°C. Those pellets that, on visual inspection, appeared to have suffered attack were removed, washed, and examined. Only $LiAlO_2$ appeared to be suitably resistant to lithium attack. As the density of the pellet was increased, the amount of attack decreased significantly. Presoaking the pellet in molten LiF-LiCl-LiI eutectic, to simulate more closely the environment that would be present in a working cell, also reduced the extent of lithium penetration and improved the resistance of the pellet to attack. With suitable pellet preparation and presoaking, attack of $LiAlO_2$ by lithium was moderate to negligible up to 450°C, a temperature higher than is expected in an operating cell. However, molten lithium at 500°C did cause appreciable attack on a $LiAlO_2$ pellet.

In summary, the tests indicated that, for compatibility with liquid lithium, the optimum fabrication conditions of $LiAlO_2$ shapes include a pressing force of about $8 \times 10^4$ psi, a sintering temperature of about 1100°C, and a molding powder fine enough so that the pellet density approaches the theoretical density of $LiAlO_2$.

2. Metals

Corrosion of Metals by Liquid Tellurium. Tungsten has been found to provide suitable resistance to attack by tellurium and lithium-tellurium alloys at temperatures up to 525°C. However, because of the high density and difficulty of fabrication of tungsten, as well as its cost, other metals have been sought for use in constructing lithium/tellurium cells. An attempt to contain tellurium in molybdenum at 500°C failed when the tellurium reacted completely in 18 hr to form a solid (ANL-7425, p. 189). In other experiments, tellurium was observed to react with iron,

forming a solid scale of $FeTe_2$. This $FeTe_2$ scale did not prevent further attack. Further tellurium corrosion tests are being held in abeyance because of greater interest in other lithium/chalcogen cells.

Corrosion of Metals by Liquid Selenium. Selenium is a particularly difficult material to contain in conductive metals because selenides of most common metals can be prepared by direct contact of the two elements at temperatures below 1000°C. Static corrosion tests have been conducted to determine the corrosion resistance of various materials to molten selenium at 375°C. These results show that neither Fansteel 85 alloy nor niobium is severely attacked by selenium under static conditions. However, tantalum and a tantalum-10 wt % tungsten alloy are less corrosion-resistant, and both Armco iron and molybdenum are severely attacked. The corrosion resistance of these and other materials to molten selenium will be tested under conditions of mild agitation.

Corrosion of Metals by Liquid Tin. Since little information on the corrosion of refractory metals by tin is available for temperatures above 800°C, corrosion studies have been made at 1300°C. (Common metals such as iron, nickel, and chromium have high solubilities in tin at temperatures above 800°C.) The results of these static tests are shown in Table IV-6.

TABLE IV-6. Corrosion of Refractory Metals by Tin at 1300°C

| Material Tested | Form of Test Material | Test Duration (hr) | Result |
|---|---|---|---|
| Tungsten | Crucible | 211 | No corrosion |
| Mo-30 wt % W | Crucible | 123 | No corrosion |
| Re-50 wt % W | Coupon | 136 | No corrosion |
| Nb-10 wt % W-2.5 wt % Zr | Crucible | 100 | 50-$\mu$m penetration by Sn; Nb-Sn interaction |
| Nb-27 wt % Ta-11 wt % W-0.8 wt % Zr | Crucible | 114 | 60-$\mu$m penetration by Sn; Nb-Sn interaction |
| Mo-0.5 wt % Ti-0.08 wt % Zr | Coupon | 137 | 50-$\mu$m penetration by Sn; Ti found in Sn |

Of the materials tested, tungsten, Mo-30 wt % W, and Re-50 wt % W appear to be suitable for construction materials in a lithium/tin thermally regenerative system. The Mo-30 wt % W is the most promising of the three because of its relative ease of fabrication.

# V. NUCLEAR CONSTANTS

An understanding of fast-neutron processes is essential to the design and development of fast breeder reactors. The objective of the nuclear constants program is to obtain cross-sectional data for neutron reactions of interest to the overall fast-reactor physics program. Two types of measurements are being made: (1) determination of selected cross sections as a function of monoenergetic neutron energies between 30 and 1700 keV, and (2) determination of integral (spectrum-averaged) cross sections in EBR-II. In a separate program on the development of methods for the determination of burnup in fast-reactor fuels, integral fission yields and integral cross sections of special interest to the burnup program are being measured.

## A. Monoenergetic Cross-Section Measurements

Measurements of monoenergetic neutron cross sections have been directed primarily toward (n,$\gamma$) reactions in fuel, cladding, and structural materials. However, effort is now being directed principally toward measurement of the production of a low-mass particles (tritium, hydrogen, and helium) in fast-neutron fission. Information on the production of tritium in fast reactors is particularly needed because of the problems of tritium disposal in fuel reprocessing and, possibly, in reactor operations. The production of hydrogen and helium are of interest because of the chemical and physical effects of their interactions, mainly with cladding material.

An experiment has been designed to measure the fission yields of these low-mass particles as a function of neutron energy. Various uranium and plutonium isotopes will be irradiated in a monoenergetic neutron beam, and the low-mass particles produced will be detected in a three-detector telescope array. After appropriate electronic manipulation, the energy of a particle will be determined from the sums of the signals from the three detectors; the type of particle will be determined from the relative energy loss in each of the three detectors.

A scattering tube has been designed and built that will house a wheel containing several targets, the telescope array, and the neutron monitoring equipment. The hardware and electronics have been assembled and calibrated. Final checkout of the instrumentation is awaiting receipt of a $^{252}$Cf source, which will yield low-mass particles by spontaneous fission. On-beam experiments with $^{235}$U and $^{239}$Pu are expected to begin upon completion of a new ANL neutron generator, which will produce higher neutron fluxes than those available in the past.

Monoenergetic capture cross-section measurements have been completed for the reactions $^{51}$V(n,$\gamma$)$^{52}$V and $^{50}$Ti(n,$\gamma$)$^{51}$Ti. Measurements for

$^{51}V$ (ANL-7425, p. 105) have been extended, and an assessment of errors has been made for all $^{51}V$ and $^{50}Ti$ data. The data for $^{50}Ti$ are presented in Fig. V-1. Cross-section measurements for the reactions $^{89}Y(n,\gamma)^{90m}Y$, $^{85}Rb(n,\gamma)^{86m}Rb$, and $^{87}Rb(n,\gamma)^{88}Rb$ have also been completed.

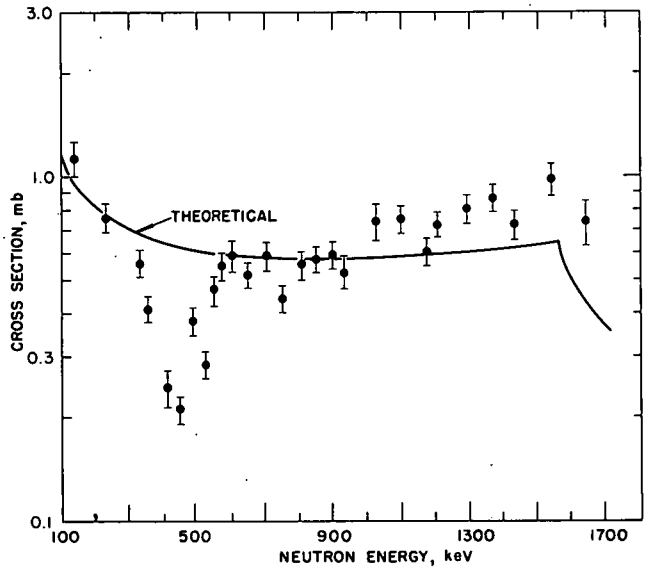


Fig. V-1. Capture Cross Section of $^{50}Ti$.

Theoretical calculations for the $(n,\gamma)$ reactions of $^{51}V$, $^{50}Ti$, and $^{87}Rb$ were performed using computer codes and the theoretical description of Moldauer,[1,2] and were compared with experimental data. The experimental and calculated values were in good agreement for $^{87}Rb$. However, the experimental measurements for $^{51}V$ and $^{50}Ti$ showed deviations from theoretical calculations that were considerably greater than the experimental uncertainties. One such deviation can be seen clearly in the data for $^{50}Ti$ at about 400 keV (see Fig. V-1). This deviation is attributed to a resonance-type structure that is not predicted by our theoretical calculations. The nature of the structure is presently being investigated.

## B. Integral Cross-Section Measurements

Many cross sections that cannot be readily measured by monoenergetic techniques can be measured in a fast-reactor neutron flux. These spectral-averaged or integral cross sections are valuable for evaluating differential data, for monitoring the number of neutrons present in a given position of a reactor, and for evaluating the spectral shape of the neutron-energy distribution.

Integral measurements have been made on specimens of type 304L stainless steel irradiated at various positions throughout the core and blankets of EBR-II. The principal purposes of this study were (1) to measure the neutron flux of EBR-II as a function of radial position and (2) to estimate the integral cross sections of important (n,p), $(n,\gamma)$, and $(n,\alpha)$ reactions occurring in irradiated stainless steel.

[1] P. A. Moldauer, Rev. Mod. Phys., 63, 1079 (1964).

[2] P. A. Moldauer, C. A. Engelbrecht, G. J. Duffy, "Nearrex, A Computer Code for Nuclear Reaction Calculations," USAEC Report ANL-6978 (1964).

The irradiated stainless steel samples were analyzed radiochemically to determine the reaction products $^{58}Co$, $^{60}Co$, $^{54}Mn$, $^{55}Fe$, and $^{63}Ni$. From these results, calculations were made of specific atom production rates, that is, the number of atoms of each of these nuclides produced per megawatt-day per gram of type 304L stainless steel; these data are shown in Fig. V-2.

Differential cross sections for the two reactions $^{54}Fe(n,p)^{54}Mn$ and $^{58}Ni(n,p)^{58}Co$ were used to determine the total EBR-II flux per megawatt at eight radial positions. These values are shown in Fig. V-3, where they are compared with a diffusion-theory calculation of the flux, and with values reported by Jackson and Ulseth[3] for an EBR-II power level of 20 kW. The excellent agreement between our full-power measurements and the low-power values of Jackson and Ulseth indicates that the flux per megawatt is independent of EBR-II reactor power level, contrary to previous conclusions.[3] From the measured value of the EBR-II flux, integral cross sections were calculated for four reactions of stainless steel at the core center and were estimated for three additional reactions. These data are summarized in Table V-1 and are compared with the data of Jackson and Ulseth.[3]

The ratio of the atom production rates of $^{54}Mn$ and $^{55}Fe$, both of which are produced from $^{54}Fe$, can serve as a very sensitive indicator of a reactor's spectral shape. This ratio at eight radial positions in EBR-II is

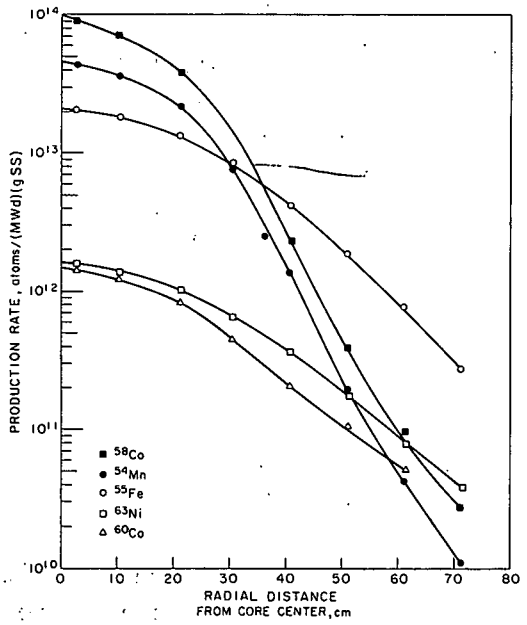


Fig. V-2. Specific Atom Production Rates in Type 304L Stainless Steel as a Function of Irradiation Position in EBR-II.

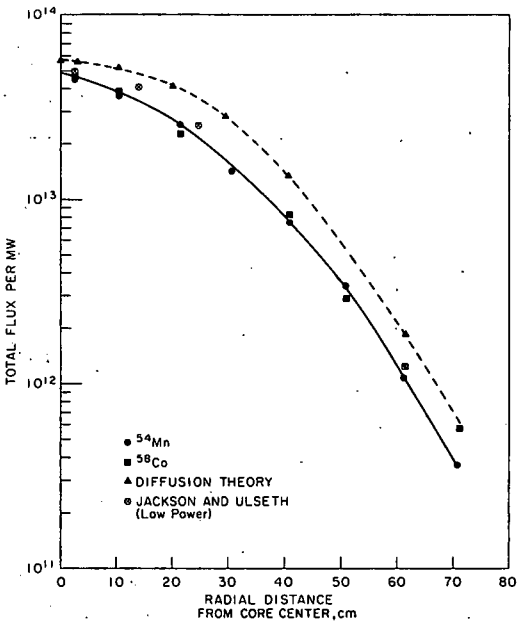


Fig. V-3. EBR-II Radial Flux per Megawatt Measured at Full Power.

[3] J. L. Jackson, J. A. Ulseth, Nucl. Appl. 5, 275 (1968).

TABLE V-1. EBR-II Spectrum-Averaged Cross Sections of Type 304L Stainless Steel Constituents

| Reaction | Cross Section at EBR-II Core Center (mb) | |
|---|---|---|
| | This Work | Jackson-Ulseth[a] |
| $^{54}Fe(n,p)^{54}Mn$ | 26 | 24 |
| $^{58}Ni(n,p)^{58}Co$ | 36 | 35 |
| $^{60}Ni(n,p)^{60}Co$ | ≈0.5 | |
| $^{58}Ni(n,\alpha)^{55}Fe$ | ≈0.1 | |
| $^{62}Ni(n,\gamma)^{63}Ni$ | 9.6 | |
| $^{54}Fe(n,\gamma)^{55}Fe$ | 9.3 | |
| $^{59}Co(n,\gamma)^{60}Co$ | ≈8.7 | |

[a]Ref. 3.

shown in Table V-2; the median neutron energy calculated by a diffusion theory is also included to demonstrate the sensitivity of this indicator.

TABLE V-2. "Spectral Hardness" Indicator in EBR-II: Atom Ratio $^{54}Mn/^{55}Fe$ Produced from $^{54}Fe$

| Radial Position[a] (cm) | Atom Ratio $^{54}Mn/^{55}Fe$ | Calculated Median Neutron Energy (keV) |
|---|---|---|
| 2.86 | 2.18 | 470 |
| 10.21 | 1.98 | 465 |
| 21.25 | 1.63 | 405 |
| 30.62 | 0.893 | 320 |
| 40.83 | 0.320 | 206 |
| 51.03 | 0.102 | |
| 61.24 | 0.056 | 140 |
| 71.45 | 0.040 | |

[a]Distance from core center.

In an extension of this work, specimens of Ti, V, S, Fe, Ni, Co, Sc, Cu, and Au were irradiated in EBR-II, and analyses of all radiochemically measurable (n,γ), (n,p), (n,α), and (n,2n) reaction products are in progress.

Work is also continuing on the determination of alpha (capture-to-fission cross-section ratio) for uranium and plutonium isotopes previously irradiated in EBR-II (see ANL-7175, p. 216). Alpha measurements for $^{233}U$ are nearly complete.

# VI. FLUIDIZED-BED COMBUSTION OF FOSSIL FUELS

The objective of this program[1] is to study the pollution abatement potential of fluidized-bed combustion systems for fossil fuels.

The concept of fluidized-bed combustion involves burning fuel in a fluidized bed of solids in which the boiler tubes are immersed. Since a fluidized bed is a highly efficient contacting medium for carrying out gas-solid reactions, use of a bed material that will react with gaseous sulfur compounds (and possibly nitrogen compounds) released during combustion appears potentially attractive. Due to the excellent heat-transfer characteristics of fluidized beds (and the resulting possibly smaller size of fluidized-bed combustors), decreased capital and operating costs compared with conventional units may also be achieved.

In the past, combustion of coal and oil in fluidized beds has been explored by a number of organizations in this country and abroad. Intensive investigation is now under way in England and in the U.S. U.S. work on process and equipment development is sponsored by NAPCA (of the Department of Health, Education, and Welfare) and the Office of Coal Research (OCR) of the U.S. Department of the Interior. NAPCA-sponsored pilot-plant studies at Pope, Evans, and Robbins complement the work of this Division, which will concentrate on pollution control aspects of fluidized-bed combustion. Our program will involve literature surveys, laboratory-scale experimental studies of potential sulfur-fixing additives, bench-scale fluid-bed tests, and appropriate evaluations. Combustion schemes such as multistage operation under oxidizing or reducing conditions will be investigated.

In the initial phase of this program, literature surveys were made to select potential additives for controlling emission of the oxides of sulfur and nitrogen. For sulfur dioxide absorption, the potential additives selected for evaluation in a fluid bed were a series of metal oxides, industrial waste materials such as red mud and spent oil shale, and phosphate rock. The initial literature survey to find additives suitable for $NO_x$ absorption was unsuccessful; it would appear at present that the control of $NO_x$ emission can be achieved mainly by controlling the combustion conditions, i.e., temperature and excess air.

Preliminary laboratory-scale experiments were initiated to investigate the potential of additives believed suitable for reacting with pollutants ($SO_2$, $H_2S$, or $NO_x$) in a fluidized bed. Relative capacities of ten materials for sulfur dioxide at 1700°F were determined in a dynamic system in which a gas mixture (0.5 vol % $SO_2$ in air) was continuously passed through a 10-g, ~1/16-in.-thick layer of additive in a vertical reactor. The additives tested

[1]Work sponsored by the National Air Pollution Control Administration (NAPCA) and performed under an agreement between NAPCA and the U.S. Atomic Energy Commission.

were dolomite, phosphate rock, spent oil shale, red mud (waste from alumina extraction from bauxite), lead oxide, manganese oxide, nickel oxide, copper oxide, cobalt oxide, and zinc oxide. Dolomite far outperformed the other materials studied. From the data, it was calculated that to remove 80% of the $SO_2$, 0.4 ton of dolomite would be required per ton of coal with 4% sulfur content.

Construction of the bench-scale fluid-bed combustor (Fig. VI-1) is under way. Initial tests will involve the addition of limestone-dolomite materials along with the coal feed into a fluidized bed to effect a reduction in sulfur oxide emissions. An objective of the tests will be to determine the conditions necessary to achieve both a high degree of $SO_2$ removal from the combustor flue gas and a high degree of utilization of the limestone material. This equipment will have the capability of varying the bed depth and fluidizing air velocity, allowing investigation of (1) the effect of gas residence time on the sulfur dioxide-additive reaction and (2) the effect of various particle sizes on sorbent utilization. Other conditions that may be varied are combustor temperature, amount of excess air, and quantity of limestone-dolomite added (number of CaO stoichiometric additions).

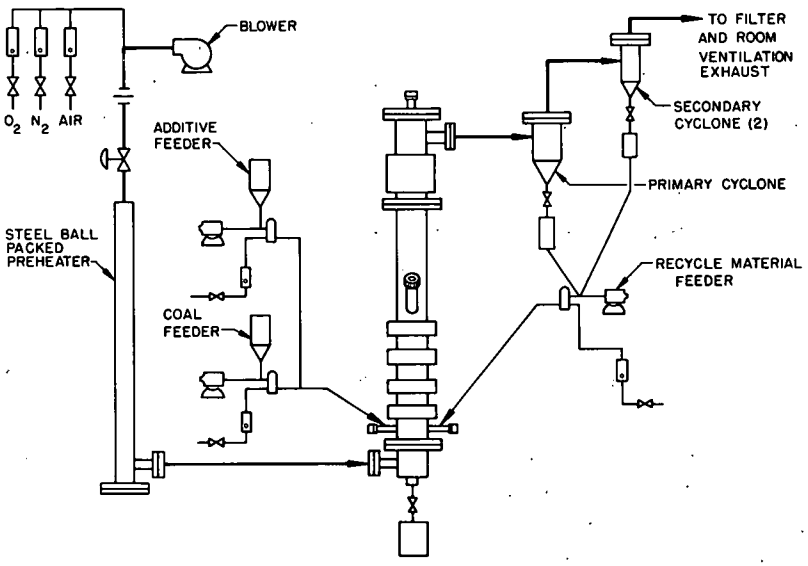


Fig. VI-1. Simplified Diagram of Fluidized-Bed Combustor and Other Bench-Scale Equipment.

Estimates have been made of the degree of $SO_2$ removal by limestone-dolomite during fluid-bed combustion of coal as a function of the fluid-bed reaction parameters. A model was developed to relate the extent of $SO_2$ removal to the selected parameters (bed height, superficial gas velocity, and particle size) as functions of stoichiometric additions of CaO for a dolomitic limestone (BCR-1337)[2] and a calcitic limestone (BCR-1360)[2] at 1600°F. The $SO_2$-limestone reaction data used was from an in-house

[2] This designation indicates materials characterized by Bituminous Coal Research, Inc. under a Public Health Service contract.

study by the National Air Pollution Control Administration. A computer program was written to perform the calculations, which in effect quantified the expected relationships between the extent of $SO_2$ removal and the operating parameters of a fluid-bed combustor, namely, that $SO_2$ absorption will be enhanced by decreasing the particle size and superficial gas velocity and by increasing the bed height.

A preliminary evaluation of the computer output allows the following conclusions to be reached: To achieve 90% removal of $SO_2$ with BCR-1337 at a superficial gas velocity of 1 ft/sec in a 1-ft high bed would require little more than one stoichiometric addition of CaO for a particle size of 282 $\mu$m, but would require about 1.7 stoichiometric additions for a 1095-$\mu$m particle size. Under the same conditions, 90% removal of $SO_2$ with BCR-1360 would require about one stoichiometric addition of CaO for a particle size of 96 $\mu$m and 1.3 stoichiometric additions for a particle size of 1095 $\mu$m.

For operation under reasonable fluid-bed conditions (a gas residence time of 2 sec or less and a $SO_2$ removal level of 90%), the maximum CaO utilizations that can be expected for BCR-1337 material are $>0.99$, 0.90, 0.75, and 0.60 for particle sizes of 96, 282, 507, and 1095 $\mu$m, respectively. For BCR-1360 material, the corresponding maximum CaO utilizations are ~0.95 and 0.75 for 96-$\mu$m and 1095-$\mu$m particles, respectively.

Preliminary experimental data of the British National Coal Board and Pope, Evans, and Robbins for $SO_2$ capture in fluidized-bed coal combustors have been compared with results predicted by the model. The results agree reasonably well.

# ADDENDUM

Publications
during 1968
by
Chemical Engineering Division
Personnel

## A. Open Literature Publications

M. D. Adams, S. C. Tong
Laser Microscope System as a Microsampling Device
Anal. Chem. 40, 1762-1765 (October 1968).

M. D. Adams, S. C. Tong, L. E. Ross
Determination of Isotope Distribution in the Microstructure of Irradiated Ceramic Fuels
Abstracts of Papers, 155th Amer. Chem. Soc. Mtg., San Francisco, March 31-April 5, 1968. Abstract 0-19.

L. J. Anastasia, P. G. Alfredson, M. J. Steindler
Fluorination of Uranium, Plutonium and Neptunium from a Fluidized Bed of Alumina
Abstracts of Papers, 155th Amer. Chem. Soc. Mtg., San Francisco, March 31-April 5, 1968. Abstract 0-145.

L. J. Anastasia, P. G. Alfredson, M. J. Steindler
Fluidized-Bed Fluoride Volatility Processing of $UO_2$-$PuO_2$ Fuels with Simulated Burnups of 10,000 and 30,000 MWD/T
Trans. Amer. Nucl. Soc. 11(2), 447 (1968).

L. J. Anastasia, P. G. Alfredson, M. J. Steindler
Fluidized-Bed Fluorination of $UO_2$-$PuO_2$ Fission Product Fuel Pellets with Fluorine
Nucl. Appl. 4, 320 (1968).

L. Baker, Jr., D. T. Eggen, R. O. Ivins, S. A. Szawlewski
The United States Liquid Metal Fast Breeder Reactor Safety Program
Proc. Intern. Conf. on the Safety of Fast Reactors, Aix-en-Provence, France, September 19-22, 1967, pp. VI-1-1 to VI-1-8, Commissariat a l'Energie Atomique, France, 1968.

J. J. Barghusen
Volatility Processes
Reactor and Fuel-Process. Technol. 10(4), 309-313 (Fall 1967).

J. J. Barghusen
Volatility Processes
Reactor and Fuel-Process. Technol. 11(1), 54-59 (Winter 1967-1968).

J. E. Battles, G. E. Gundersen, R. K. Edwards
A Mass Spectrometric Study of the Rhenium-Oxygen System
J. Phys. Chem 72(12), 3963 (1968).

J. E. Battles, J. W. Reishus, W. A. Shinn
Physical Properties of Nuclear Ceramics
American Ceramic Society Bulletin, 47(4), 414 (1968).
Abstract 8-N-68.

P. Budininkas, R. K. Edwards, P. G. Wahlbeck
Dissociation Energies of Group VIa Gaseous Homonuclear Diatomic Molecules,
I. Sulfur, J. Chem. Phys. 48(7), 2859 (1968).
II. Selenium, J. Chem. Phys. 48(7), 2867 (1968).
III. Tellurium, J. Chem. Phys. 48(7), 2870 (1968).

E. J. Cairns, A. M. Breitenstein, A. J. Scarpellino
The Kinetics of Adsorption, Surface Reaction, and Electrochemical Oxidation of Propane on Platinum in Hydrofluoric Acid
J. Electrochem. Soc. 115, 569 (1968).

E. J. Cairns, E. L. Simons, A. D. Tevebaugh
Ammonia-Oxygen Fuel Cell
Nature 217, 780-781 (February 1968).

E. J. Cairns, J. Paynter
Electrocatalysts for the Direct Anodic Oxidation of n-Octane in Fuel Cells
J. Electrochem. Soc. 115, 1218 (1968).

A. A. Chilenskas
Fluidized-Bed Fluoride Volatility Processing of Irradiated $UO_2$ Fuels
Nucl. Appl. 5, 11 (July 1968).

A. A. Chilenskas, K. S. Turner
Engineering Development of a Fluidized-Bed Fluoride Volatility Process. III. Bench-Scale Studies with Irradiated Uranium Alloy Fuels*
Nucl. Appl. 4, 6-16 (January 1968).

H. H. Claassen, E. L. Gasner, H. Kim, J. L. Huston
Vibrational Spectra and Structure of $XeO_2F_2$
J. Chem. Phys. 49, 253-257 (July 1968).

H. H. Claassen, E. L. Gasner, H. Selig
Vibrational Spectra of $IF_7$ and $ReF_7$
J. Chem. Phys. 49, 1803-1807 (August 1968).

P. M. Danielson
Helium Pumping with a Sputter-Ion Pump
J. Vacuum Sci. Technol. 5(3), 89 (1968).

*Also listed in ANL-7450.

P. M. Danielson, J. S. Hetherington
Ultrahigh Vacuum Equipment for Materials Studies above 2000°C
International Transactions, Vacuum Metallurgy Conference - 1967,
E. L. Foster (Ed.), pp. 305-319, New York, 1968.

J. J. Dutton, J. Royal, D. H. Lennox, R. Gold, K. K. Brown,
P. H. Gregory (Eds.)
Reactor and Fuel-Processing Technology
Division of Technical Information, U.S. Atomic Energy Commission,
Vol. 10(4) (Fall 1967).

J. J. Dutton, J. Royal, D. H. Lennox, R. Gold, K. K. Brown,
P. H. Gregory (Eds.)
Reactor and Fuel-Processing Technology
Division of Technical Information, U.S. Atomic Energy Commission,
Vol. 11(1) (Winter 1967-1968).

J. J. Dutton, J. Royal, D. H. Lennox, R. Gold, K. K. Brown,
P. H. Gregory (Eds.)
Reactor and Fuel-Processing Technology
Division of Technical Information, U.S. Atomic Energy Commission,
Vol. 11(2) (Spring 1968)

J. J. Dutton, J. Royal, D. H. Lennox, R. Gold (Eds.)
Reactor and Fuel-Processing Technology
Division of Technical Information, U.S. Atomic Energy Commission,
Vol. 11(3) (Summer 1968)

E. Greenberg, W. N. Hubbard
Fluorine Bomb Calorimetry. XXIII. The Enthalpy of Formation of
Carbon Tetrafluoride*
J. Phys. Chem. 72(1), 222-227 (1968).

D. E. Grosvenor
Compact Centerless Grinds "Hot" Materials
The Tool and Manufacturing Engineer, ASTME, 61(5), 22-24 (1968).

D. E. Grosvenor, D. J. Raue, R. V. Kinzler
Electrical Connectors that Resist High Temperature
Chem. Eng. 75, 172-174 (October 21, 1968).

D. E. Grosvenor, I. O. Winsch, W. E. Miller, G. J. Bernstein, R. D. Pierce
Corrosion-Resistant Heated Transfer Tubes for Molten Metals
and Salts
Nucl. Appl. 5, 329-332 (November 1968).

*Also listed in ANL-7450.

D. M. Gruen, M. Krumpelt, I. Johnson
Electronic Absorption Spectra of Solutions of Sodium Metal in Solid and Liquid Sodium Chloride
Abstracts of Papers, 156th Amer. Chem. Soc. Mtg., Atlantic City, September 8-13, 1968, ANAL-26.

R. J. Gulley, D. R. Armstrong, L. J. Harrison
Transient Irradiation Experiments with Vibrationally Compacted $UO_2$ Fuel Rods in TREAT
Trans. Amer. Nucl. Soc. 11(1), 111 (1968).

J. C. Hesson, M. S. Foster, H. Shimotake
Self-Discharge in Alkali Metal-Containing Bimetallic Cells
J. Electrochem. Soc. 115, 787-790 (August 1968).

J. C. Hesson, R. O. Ivins, R. E. Wilson
Effects of Metal-Water Reactions on Reactor Loss-of-Coolant Accidents
Abstracts of Papers, 156th Amer. Chem. Soc. Mtg., Atlantic City, September 8-13, 1968, NUCL-122.

J. C. Hesson, R. O. Ivins
Heat Transfer from Small Hot Spheres Moving Through Water
Trans. Amer. Nucl. Soc. 11(1), 327 (1968).

J. C. Hesson, H. Shimotake, J. M. Tralmer
Densities of Molten Sodium-Lead and Sodium-Bismuth Alloys*
J. Metals 20(2), 6-7 (1968).

J. C. Hesson, H. Shimotake, J. M. Tralmer
Density, Surface Tension, and Viscosity of NaF-NaCl-NaI Eutectic
J. Chem. Eng. Data 13(2), 272 (1968).

J. C. Hesson, L. C. Witte, R. O. Ivins, A. D. Tevebaugh
Transient Heat Transfer Studies in Water and in Sodium Coolant
Heat Transfer Newsletter No. 2, pp. 9-10, Committee Reactor Safety Technology, European Nuclear Energy Agency, O.E.C.D. (December 1967).

J. T. Holmes, L. B. Koppel
Use of a Fractional Factorial Experiment in the Development of a Fluid-Bed Disposal Unit for Fluorine
Abstracts of Papers, 155th Amer. Chem. Soc. Mtg., San Francisco, March 31-April 5, 1968, L-84.

J. T. Holmes, L. B. Koppel, J. D. Gabor, D. Ramaswami, A. A. Jonke
Engineering-Scale Studies of the Fluorination of Uranium Oxide with Bromine Pentafluoride
Ind. Eng. Chem. Process Des. Develop. 8(1), 43 (1969).

*Also listed in ANL-7450.

W. N. Hubbard, P. A. G. O'Hare, H. M. Feder
Experimental Inorganic Thermochemistry
Ann. Rev. Phys. Chem. 19, 111-128 (1968).

R. L. Jarry, M. J. Steindler
The Reaction of Gaseous Bromine Pentafluoride with Uranium Compounds. II. The Kinetics of the Reaction with $U_3O_8$, $UO_2$, and $UO_3$
J. Inorg. Nucl. Chem. 30(1), 127-132 (1968).

C. E. Johnson
Solid-Liquid Phase Equilibria and Specific Conductivity for the Ternary Lithium Fluoride-Lithium Chloride-Lithium Iodide System
Abstracts of Papers, 155th Amer. Chem. Soc. Mtg., San Francisco, March 31-April 5, 1968, M-128.

C. E. Johnson, A. K. Fischer, E. J. Cairns, M. S. Foster
New Measurements for the Sodium-Bismuth Binary System
Abstracts of Papers, 156th Amer. Chem. Soc. Mtg., Atlantic City, September 8-13, 1968. PHYS-94.

G. K. Johnson, E. H. VanDeventer, O. L. Kruger, W. N. Hubbard
The Enthalpies of Formation of Plutonium Dioxide and Plutonium Nitride
Abstracts of Papers, 23rd Annual Calorimetry Conference, Midland, Michigan, August 13-15, 1968.

T. R. Johnson, F. G. Teats, R. D. Pierce
An Induction Probe for Measuring Levels in Liquid Metals*
Nucl. Appl. 4(1), 47 (1968).

I. E. Knudsen, W. F. Olsen
Direct Indication of Particle Size in Fluidized Beds*
Chem. Eng. 75, 190 (January 15, 1968).
(Republication of an article in Chem. Eng. 74, 224 (April 10, 1967) in recognition of an award.)

L. B. Koppel
Dynamics and Control of a Batch Reactor
Ind. Eng. Chem. Process Des. Develop. 7, 416 (July 1968).

T. S. Krolikowski, L. Leibowitz, R. O. Ivins, S. K. Stynes
Violently Sprayed Sodium-Air Reaction in an Enclosed Volume
Abstracts of Papers, 156th Amer. Chem. Soc. Mtg., Atlantic City, September 8-13, 1968, NUCL-123.

M. Krumpelt, J. Fischer, I. Johnson
The Reaction of Magnesium Metal with Magnesium Chloride
J. Phys. Chem. 72, 506-511 (February 1968).

*Also listed in ANL-7450.

M. L. Kyle, R. D. Pierce, L. F. Coleman, J. D. Arntzen
Removal of Nitrogen from Argon with Titanium-Metal Sponge
Ind. Eng. Chem. Process Des. Develop. 7, 447-453 (July 1968).

N. M. Levitz, G. J. Vogel, E. L. Carls, D. Grosvenor, B. Kullen, D. Raue, W. Murphy
Kilogram-Scale Production of Plutonium Hexafluoride in a Fluidized Bed
Trans. Amer. Nucl. Soc. 11(1), 35 (1968).

H. A. Liebhafsky, E. J. Cairns
Fuel Cells and Fuel Batteries
John Wiley and Sons, New York, 1968.

G. J. Macur, R. K. Edwards, P. G. Wahlbeck
Measurement of Activities in Gallium-Indium Liquid Alloys
J. Phys. Chem. 72(3), 1047-1050 (1968).

V. A. Maroni, E. J. Cairns
A Review of Raman Spectroscopy of Fused Salts and Studies of Some Halide-Containing Systems
Abstracts of Papers, 156th Amer. Chem. Soc. Mtg., Atlantic City, September 8-13, 1968, ANAL-30.

W. E. Miller, R. K. Steunenberg
Compact Pyrochemical Processes
Reactor and Fuel-Process. Technol. 10(4), 314-318 (Fall 1967).

W. E. Miller, R. K. Steunenberg
Compact Pyrochemical Processes
Reactor and Fuel-Process. Technol. 11(1), 60-64 (Winter 1967-1968).

W. E. Miller, R. K. Steunenberg
Compact Pyrochemical Processes
Reactor and Fuel-Process. Technol. 11(2), 96-100 (Spring 1968).

W. E. Miller, R. K. Steunenberg
Compact Pyrochemical Processes
Reactor and Fuel-Process. Technol. 11(3), 154-158 (Summer 1968).

P. A. G. O'Hare, J. L. Settle, H. M. Feder, W. N. Hubbard
The Thermochemistry of Some Uranium Compounds
in Thermodynamics of Nuclear Materials, pp. 265-278, Int. Atomic Energy Agency, Vienna, 1968.

E. J. Petkus, T. R. Johnson, R. K. Steunenberg
Uranium Monocarbide Preparation in a Liquid Metal
Nucl. Appl. 4, 388 (June 1968).

C. Postmus, V. A. Maroni, J. R. Ferraro, S. S. Mitra
High Pressure-Laser Raman Spectra
Inorg. Nucl. Chem. Letters 4, 269 (1968).

J. G. Schnizlein, D. F. Fischer
Ignition Behavior of Plutonium Metal and Certain Binary Alloys
J. Electrochem. Soc. 115(5), 462-466 (1968).

H. Selig, E. L. Gasner
The Rhenium Heptafluoride-Hydrogen Fluoride System
J. Inorg. Nucl. Chem. 30, 658 (1968).

H. Selig, A. Reis, E. L. Gasner
Raman Spectra of Liquid $NbF_5$ and $TaF_5$
J. Inorg. Nucl. Chem. 30, 2087-2090 (August 1968).

J. L. Settle, J. H. E. Jeffes, P. A. G. O'Hare, W. N. Hubbard
The Enthalpies of Formation of Iodine Pentafluoride and Iodine Heptafluoride
Abstracts of Papers, 23rd Annual Calorimetry Conference, Midland, Michigan, August 13-15, 1968.

H. Shimotake, E. J. Cairns
A Lithium/Tin Cell with an Immobilized Fused-Salt Electrolyte: Cell Performance and Thermal Regeneration Analysis
Intersoc. Energy Conversion Eng. Conf. 1968 Record, pp. 76-91, IEEE, New York, 1968.

H. Shimotake, E. J. Cairns
A High-Rate Lithium/Selenium Secondary Cell with a Fused-Salt Electrolyte
Extended Abstracts of Electrochemical Society, Industrial Electrolytics Div. 4, 674 (May 1968), Abst. 282; J. Electrochem. Soc. 115, 92C (1968). Abstract.

H. Shimotake, E. J. Cairns
A High Rate Lithium/Selenium Secondary Cell with a Fused-Salt Electrolyte
Comité Intern. de Thermodynamique et de Cinetique Electrochemiques. Intern. Union Pure and Appl. Chem., 19th Meeting, Detroit, September 23-27, 1968. Extended Abstracts, pp. 254-258.

H. Shimotake, J. C. Hesson
A Sodium-Bismuth Bimetallic Galvanic Cell
J. Electrochem. Soc. Japan 36(2), 118 (1968).

H. Shimotake, G. L. Rogers, E. J. Cairns
Secondary Cells with Lithium Anodes and Immobilized Fused-Salt Electrolytes
Ind. Eng. Chem. Process Des. Develop. 8(1), 51 (1969).

E. L. Simons, E. J. Cairns, D. J. Surd
The Performance of Direct Ammonia Fuel Cells
J. Electrochem. Soc. 225C (1968). Abstract.

R. K. Steunenberg, I. Johnson, R. D. Pierce
Salt Transport Process for Fast Breeder Reactor Fuels
Trans. Amer. Nucl. Soc. 11(2), 447 (1968).

D. C. Stupegia, M. Schmidt, C. R. Keedy, A. A. Madson
Neutron Capture between 5 keV and 3 MeV
J. Nucl. Energy 22, 267-281 (May 1968).

M. Tetenbaum, P. D. Hunt
High-Temperature Thermodynamic Properties of Oxygen - Deficient Urania
J. Chem. Phys. 49(11), 4739 (1968).

L. E. Trevorrow, T. J. Gerding, M. J. Steindler
Studies in the Chemistry of $NpF_6$
Abstracts of Papers, 155th Amer. Chem. Soc. Mtg., San Francisco, March 31-April 5, 1968. Abstract 0-25.

L. E. Trevorrow, T. J. Gerding, M. J. Steindler
The Fluorination of Neptunium (IV) Fluoride and Neptunium (IV) Oxide
J. Inorg. Nucl. Chem. 30(10), 2671-2678 (1968).

L. E. Trevorrow, T. J. Gerding, M. J. Steindler
The Reaction of Neptunium Hexafluoride with Sodium Fluoride
Inorg. Chem. 7(11), 2226-2229 (1968).

D. R. Vissers, M. J. Steindler
Removal of $TeF_6$ from Gaseous Systems by Solid Reagents
Ind. Eng. Chem. Process Des. Develop. 7(4), 496 (1968).

G. J. Vogel, J. J. Barghusen
Volatility Processes
Reactor and Fuel-Process. Technol. 11(2), 101-106 (Spring 1968).

G. J. Vogel
Volatility Processes
Reactor and Fuel-Process. Technol. 11(3), 149-153 (Summer 1968).

D. A. Wenz
Solubility and Spectra of Cadmium in Dilute Cadmium Chloride-Molten Salt Mixtures
J. Chem. Eng. Data 13, 448-449 (July 1968).

L. C. Witte
An Experimental Study of Forced-Convection Heat Transfer from a Sphere to Liquid Sodium*
Trans. ASME (J. Heat Transfer) 90C, 9-12 (February 1968).

L. C. Witte
Film Boiling from a Sphere
Ind. Eng. Chem. Fundamentals 7(3), 517-518 (August 1968). Letter.

*Also listed in ANL-7450.

L. C. Witte, M. B. Silverman, R. O. Ivins, L. Baker, Jr.
An Apparatus for Obtaining Extremely Large Heat Flux Densities
J. Sci. Instrum. (J. Phys. E) Ser. 2, 1, 555-557 (May 1968).

L. C. Witte, L. Baker, Jr., D. R. Haworth
Heat Transfer from Spheres into Subcooled Liquid Sodium during Forced Convection
Trans. ASME (J. Heat Transfer) 90C, 394-398 (November 1968).

B. Papers Accepted for Publication in the Open Literature

J. J. Barghusen, A. A. Jonke, N. M. Levitz, M. J. Steindler, R. C. Vogel
Fluid-Bed Fluoride Volatility Processing of Reactor Fuel Materials*
Accepted for publication as a chapter in Progr. Nucl. Energy, Ser. III, Process Chemistry, Vol. 4.

E. J. Cairns, H. A. Liebhafsky
Increased Irreversibility Caused by Composition Changes in Fuel Cells
Accepted for publication in Energy Conversion.

E. J. Cairns, H. Shimotake
High Temperature Batteries
Accepted for publication in Science.

E. J. Cairns, H. Shimotake
Recent Advances in Fuel Cells and their Application to New Hybrid Systems
Accepted for publication in Advan. Chem. Ser.

M. G. Chasanov, R. V. Schablaske, I. Johnson
The System Ta-Zn: Phase Studies
Accepted for publication in J. Electrochem. Soc. Japan.

P. M. Danielson, F. C. Mrazek
A Foreline Trap for Contamination-Free Roughing
Accepted for publication in J. Vac. Sci. Technol.

D. F. Fischer, J. G. Schnizlein
The Ignition of Irradiated Uranium
Accepted for publication in J. Nucl. Mater.

J. D. Gabor
Interaction Effects on the Fluid Dynamics of Bubbles in a Fluidized Bed: Chain of Rising Bubbles in an Infinite Two-dimensional Medium
Accepted for publication in Ind. Eng. Chem. Fundamentals.

E. C. Gay, P. A. Nelson, W. P. Armstrong
Flow Properties of Suspensions with High Solids Concentration
Accepted for publication in A.I.Ch.E. (Amer. Inst. Chem. Eng.) J.

*Also listed in ANL-7450.

J. T. Holmes, L. B. Koppel, J. D. Gabor, D. Ramaswami, A. A. Jonke
Engineering Scale Studies of the Fluorination of Uranium Oxide with Bromine Pentafluoride
Accepted for publication in Ind. Eng. Chem. Process Des. Develop.

R. L. Jarry, M. J. Steindler
The Reaction of Gaseous Bromine Trifluoride with $U_3O_8$
Accepted for publication in J. Inorg. Nucl. Chem.

G. K. Johnson, E. H. VanDeventer, O. L. Kruger, W. N. Hubbard
The Enthalpies of Formation of Plutonium Dioxide and Plutonium Mononitride
Accepted for publication in J. Chem. Thermodynamics.

L. B. Koppel, R. D. Patel, J. T. Holmes
Statistical Models for Surface Renewal in Heat and Mass Transfer: Part III. Residence Time and Age Distributions
Accepted for publication in A.I.Ch.E. (Amer. Inst. Chem. Eng.) J.

L. B. Koppel, R. D. Patel, J. T. Holmes
Statistical Models for Surface Renewal in Heat and Mass Transfer: Part IV. Wall-to-Fluidized-Bed Heat Transfer Coefficients
Accepted for publication in A.I.Ch.E. (Amer. Inst. Chem. Eng.) J.

L. Leibowitz, L. W. Mishler, M. G. Chasanov
Enthalpy of Solid Uranium Dioxide from 2500°K to its Melting Point
Accepted for publication (as a letter to the editor) in J. Nucl. Mater.

L. Leibowitz, M. G. Chasanov, L. W. Mishler
The Enthalpy of Solid Tungsten from 2800°K to its Melting Point
Accepted for publication in Trans. Met. Soc. AIME.

N. M. Levitz, G. J. Vogel, E. L. Carls, D. E. Grosvenor, B. Kullen, D. Raue, W. Murphy
Kilogram Scale Production of Plutonium Hexafluoride by Fluorination in a Fluidized Bed
Accepted for publication in Nucl. Appl.

L. E. Ross, R. A. Juvinall
A Small Cylindrical Separatory Funnel and Rack
Accepted for publication in J. Chem. Education.

R. K. Steunenberg, R. D. Pierce, L. Burris, Jr.
Pyrometallurgical and Pyrochemical Fuel Processing Methods*
Accepted for publication as a chapter in Progr. Nucl. Energy, Ser. III, Process Chemistry, Vol. 4.

E. Veleckis, R. K. Edwards
Thermodynamic Properties in the Systems V-H, Nb-H, and Ta-H
Accepted for publication in J. Phys. Chem.

*Also listed in ANL-7450.

C. ANL Reports

L. J. Anastasia, P. G. Alfredson, M. J. Steindler, G. W. Redding, J. G. Riha, M. Haas
Laboratory Investigations in Support of Fluid-Bed Fluoride Volatility Processes. Part XVI. The Fluorination of $UO_2$-$PuO_2$-Fission Product Oxide Pellets with Fluorine in a 2-Inch-Diameter Fluid-Bed Reactor
ANL-7372.

E. J. Cairns, C. E. Crouthamel, A. K. Fischer, M. S. Foster, J. C. Hesson, C. E. Johnson, H. Shimotake, A. D. Tevebaugh
Galvanic Cells with Fused-Salt Electrolytes
ANL-7316.

E. L. Carls, N. M. Levitz
Blowback of Sintered-Metal Filters: A Review of Tests and Operating Experience
ANL-7392.

N. D. Dudey
Review of Low-Mass Atom Production in Fast Reactors
ANL-7434.

J. C. Hesson, J. L. Anderson, R. O. Ivins
CHEMLOC-II: A Computer Program Describing the Core Heating and Cladding-Steam Reaction for a Water-Cooled Power Reactor following a Loss of Coolant
ANL-7361.

J. T. Holmes, L. B. Koppel, N. Saratchandran, J. B. Strand, D. Ramaswami
Engineering Development of Fluid-Bed Fluoride Volatility Processes. Part 13. Pilot-Plant Studies of the Fluorination of Uranium Oxide with Bromine Pentafluoride
ANL-7370.

R. L. Jarry, J. J. Stockbar, M. J. Steindler
Laboratory Investigations in Support of Fluid-Bed Fluoride Volatility Processes. Part XIX. Reaction of Bromine Pentafluoride with Selected Compounds of Uranium and Plutonium
ANL-7412.

N. M. Levitz, G. J. Vogel, E. L. Carls, D. E. Grosvenor, W. A. Murphy, B. J. Kullen, D. J. Raue
Engineering Development of Fluid-Bed Fluoride Volatility Processes. Part 15. Material Balance Demonstrations, Production Rates, and Fluorine Utilizations in Fluorination of Kilogram Quantities of $PuF_4$ to $PuF_6$ with Elemental Fluorine in a Fluid-Bed Reactor
ANL-7468.

W. E. Miller, G. J. Bernstein, R. M. Fryer, R. F. Malecha, M. A. Slawecki, R. C. Paul
The EBR-II Skull Reclamation Process. Part III. Skull Oxidation Equipment*
ANL-7338.

P. A. G. O'Hare
The Thermodynamic Properties of Some Chalcogen Fluorides
ANL-7315.

R. D. Patel
Surface-Renewal Models for Heat Transfer between Walls and Fluidized Beds
ANL-7353.

D. Ramaswami, L. J. Anastasia, N. M. Levitz, W. J. Mecham, A. A. Jonke
Engineering Development of Fluoride Volatility Processes. Part II. Off-gas Analysis
ANL-7339.

W. A. Shinn, M. J. Steindler
Laboratory Investigations in Support of Fluid-Bed Fluoride Volatility Processes. Part XVIII. Neutron Counting as an Analytical Method for Plutonium Fluorides
ANL-7402.

L. E. Trevorrow, T. J. Gerding, M. J. Steindler
Laboratory Investigations in Support of Fluid-Bed Fluoride Volatility Processes. Part XVII. Fluorination of Neptunium (IV) Fluoride and Neptunium (IV) Oxide
ANL-7385.

L. E. Trevorrow, M. J. Steindler
Laboratory Investigations in Support of Fluid-Bed Fluoride Volatility Processes. Part XV. Estimation of Rates of Thermal Decomposition of Plutonium Hexafluoride in Process Streams*
ANL-7347.

D. R. Vissers, M. J. Steindler
Laboratory Investigations in Support of Fluid-Bed Fluoride Volatility Processes. Part XX. Fission Product Tellurium Off-Gas Disposal in the Fluid-Bed Fluoride Volatility Process
ANL-7469.

R. C. Vogel, E. R. Proud, J. Royal
Chemical Engineering Division Semiannual Report, January-June 1967
ANL-7375.

*Also listed in ANL-7450.

R. C. Vogel, E. R. Proud, J. Royal
Chemical Engineering Division Semiannual Report, July-December 1967
ANL-7425.

R. C. Vogel, E. R. Proud, J. Royal
Chemical Engineering Division Research Highlights, May 1967-April 1968
ANL-7450.

D. Papers Presented at Scientific Meetings

L. J. Anastasia
Fluorination of Uranium Oxides in Fluidized-Bed Reactors
Presented at 1968 Tripartite Chemical Engineering Conference, A.I.Ch.E., Montreal, September 22-25, 1968.

L. Baker, Jr., R. O. Ivins
Metal-Water Reactions
Presented at Symposium on Chemical Engineering in the Reactor Safety Program, A.I.Ch.E.-IIQPR joint meeting, Tampa, Florida, May 19-22, 1968.

M. H. Barsky, A. F. Panek
The Flame Spectrophotometric Determination of Ruthenium
Presented at the 12th Conference on Analytical Chemistry in Nuclear Technology, Gatlinburg, Tennessee, October 8-10, 1968.

J. E. Battles, J. W. Reishus, W. A. Shinn
A Mass Spectrometric Study of the Volatilization of Plutonia
Presented at the 70th Annual Meeting, Amer. Ceram. Soc., Chicago, April 20-25, 1968.

F. A. Cafasso
The Thermodynamic Properties of Liquid Binary Alkali Metal Alloys; A Study in Atomic Absorption Spectrophotometry
Presented to the Department of Chemistry, DePaul University, February 23, 1968.

E. J. Cairns
The Adsorption and Anodic Oxidation of Propane
Presented at Illinois Institute of Technology, Chicago, March 6, 1968.

E. J. Cairns
The Physical Chemistry of Fused Salts and Liquid Metals in Relation to Energy Conversion
Presented at University of California, Berkeley, March 29, 1968.

E. J. Cairns
Chemistry of Fuel Cells and Batteries
Presented at ACS meeting, Chicago, April 29, 1968.

A. A. Chilenskas
Volatility Experiments on Irradiated Fuels
Presented at Rocky Flats Fluoride Volatility Meeting, Golden, Colorado, June 24-25, 1968.

P. M. Danielson
Developments for Using Ultrahigh Vacuum Systems with Plutonium Gloveboxes
Presented at 6th Annual Symposium of Midwest Section, American Vacuum Society, Gatlinburg, Tennessee, May 23-24, 1968.

N. D. Dudey, V. E. Noshkin, L. E. Ross
Application of Activation Analysis and Ge(Li) Detection Techniques for the Determination of Stable Elements in Marine Aerosols - Modern Trends in Activation Analysis
Presented at International Conference on Neutron Activation Analysis, Gaithersburg, Maryland, October 9, 1968.

R. K. Edwards, M. Chandrasekharaiah, P. M. Danielson
Congruent Vaporization and the Temperature Dependence of Congruently Vaporizing Compositions of Urania
Presented at Gordon Research Conference, Washington, July 29-August 2, 1968.

J. D. Gabor
Chairman, Symposium on Fundamental and Applied Fluidization, Tampa, Florida, May 19-22, 1968.

E. C. Gay, P. A. Nelson, W. P. Armstrong
Flow Properties of Suspensions with High Solids Concentration
Presented at Symposium on Structural and Molecular Rheology, A.I.Ch.E. National Meeting, St. Louis, February 18-21, 1968.

E. Greenberg
Fluorine Bomb Calorimetry
Presented to the Department of Chemistry, DePaul University, November 15, 1968.

W. N. Hubbard
Fluorine Bomb Calorimetry
Presented at the IVth All-Union (Soviet) Conference on Calorimetry, Leningrad, USSR, May 20-25, 1968.

W. N. Hubbard
Thermodynamic Studies on Fluoride Bond Strengths
Presented at Gordon Conference, Tilton, New Hampshire, July 15-19, 1968.

R. O. Ivins
TREAT Fuel Failure Experiments
Presented to Advisory Committee on Reactor Safeguards, Safety Research Subcommittee Meeting on Reactivity and Spatial Neutronic Effects in Large Water Reactors, Washington, D.C., March 14, 1968.

R. O. Ivins
Fuel and Coolant Dynamics
Presented at 7th Annual Student-Faculty Conference, Argonne, August 22, 1968.

I. Johnson
Status of the Salt-Transport Process - Laboratory Development
Presented to Chemistry and Chemical Separations Branch, Division of Reactor Development and Technology, USAEC, Washington, May 16, 1968.

I. Johnson
Salt Transport Process for Recovery of Fast Breeder Reactor Fuels. Part II. Chemical Basis
Presented at Oak Ridge National Laboratory, July 17, 1968.

T. R. Johnson, R. D. Pierce, F. G. Teats, E. F. Johnston
Behavior of Countercurrent Liquid-Liquid Columns with a Liquid Metal
Presented at 61st Annual Meeting, A.I.Ch.E., Los Angeles, December 1-5, 1968.

A. A. Jonke
Development of Volatility Process for Thermal and Fast Reactor Fuels
Presented at Rocky Flats Fluoride Volatility Meeting, Golden, Colorado, June 24-25, 1968.

A. A. Jonke, E. L. Carls, R. L. Jarry
Reduction of Atmospheric Pollution by the Application of Fluidized-Bed Combustion
Presented at 1st International Conference on Fluidized-Bed Combustion, Heuston Woods State Park, Ohio, November 18-22, 1968.

R. W. Kessie
Containment of $PuF_6$
Presented at Rocky Flats Fluoride Volatility Meeting, Golden, Colorado, June 24-25, 1968.

M. L. Kyle, R. D. Pierce
Salt Transport Process Materials Testing
Presented at 1968 AEC Corrosion Symposium, Battelle Memorial Institute, Columbus, Ohio, May 6, 1968.

R. P. Larsen
Determination of Burnup on Nuclear Fuel
Presented at Atomic Energy Commission of Canada, Chalk River, Ontario, April 8, 1968.

R. P. Larsen, L. E. Ross, E. C. Bogusch
The Liquid Scintillation Determination of Plutonium
Presented at the 12th Conference on Analytical Chemistry in Nuclear Technology, Gatlinburg, Tennessee, October 8-10, 1968.

N. M. Levitz
Fluorination of Uranium and Plutonium to Hexafluorides
Presented at Rocky Flats Fluoride Volatility Meeting, Golden, Colorado, June 24-25, 1968.

C. Luner, H. M. Feder, F. A. Cafasso
Carbon Transport in Sodium Systems
Presented at AEC-ANL International Symposium on Sodium Technology and Large Fast Reactor Design, Argonne, November 7-9, 1968.

R. J. Meyer, C. E. Johnson, L. E. Ross
Trace Element Behavior in Liquid Sodium
Presented at AEC-ANL International Symposium on Sodium Technology and Large Fast Reactor Design, Argonne, November 7-9, 1968.

L. W. Mishler, L. Leibowitz
A High Temperature Calorimetric System
Presented at 23rd Annual Calorimetry Conference, Midland, Michigan, August 13-15, 1968.

P. A. Nelson, D. E. Grosvenor, S. Vogler, N. Quattropani, P. Krause
Synthesis of (U-Pu)C from U-Pu Alloy and Fabrication of Fuel Pellets
Presented at 70th Annual Meeting, Amer. Ceram. Soc., Chicago, April 23, 1968.

P. A. Nelson
The Future of the Nuclear Power Industry
Presented to 23rd Naval Research Reserve Unit, 9th Naval District, May 23, 1968.

P. A. Nelson, J. Fischer, J. F. Lenc, R. K. Steunenberg
Pyrochemical Processing of Plutonium-238 Scrap
Presented at Plutonium-238 Isotopic Fuels and Heat Source Program Review, AEC Headquarters, Germantown, Maryland, October 29-30, 1968.

V. E. Noshkin, N. D. Dudey, L. E. Ross
Stable Elements in Over-Ocean Aerosols
Presented at the 12th Conference on Analytical Chemistry in Nuclear Technology, Gatlinburg, Tennessee, October 8-10, 1968.

R. D. Pierce
Status of the Salt-Transport Process - Engineering Development
Presented to Chemical and Chemical Separations Branch, Division of Reactor Development and Technology, USAEC, Washington, May 16, 1968.

R. D. Pierce
Salt Transport Process for Recovery of Fast Breeder Reactor Fuels. Part III. Engineering Developments
Presented at Oak Ridge National Laboratory, July 17, 1968.

R. D. Pierce
Mass Transfer Studies with Liquid Metal-Salt Systems
Presented to Chemical Engineering Department, University of Notre Dame, December 4, 1968.

R. V. Schablaske, M. I. Homa, R. P. Larsen
The X-Ray Spectrometric Determination of Fission Product Rare Earths--Application to the Measurement of Burnup in Nuclear Fuels
Presented at the 12th Conference on Analytical Chemistry in Nuclear Technology, Gatlinburg, Tennessee, October 8-10, 1968.

H. Shimotake
Regenerative Galvanic Cell Systems*
Presented at Northwestern University, January 22, 1968.

H. Shimotake
Bimetallic Galvanic Cells*
Presented at RESA Colloquium, Whirlpool Branch, St. Joseph, Michigan, January 26, 1968.

H. Shimotake, E. J. Cairns
Lithium/Chalcogen Secondary Cells
Presented at The Fourth Advances in Battery Technology Symposium, Los Angeles, California, December 6, 1968.

N. R. Stalica
Uranium, Plutonium, and Fission Product Distribution in Irradiated Fuels
Presented at General Electric - Atomic Products Division, San Jose, California, June 28, 1968.

N. R. Stalica, C. A. Seils
Distribution of Plutonium and Uranium in a Mixed Oxide Fuel Irradiated in a Fast Neutron Flux
Presented at 3rd National Conference on Electron Microprobe Analysis, Chicago, August 2, 1968.

M. J. Steindler
The Chemistry of Plutonium Hexafluoride
Presented at Rocky Flats Fluoride Volatility Meeting, Golden, Colorado, June 24-25, 1968.

M. J. Steindler
Volatility Process Principles and Applications
Presented at USAEC Safeguards Training Program, Argonne, November 4, 1968.

*Also listed in ANL-7450.

R. K. Steunenberg
Status of the Salt Transport Process
Presented to Chemistry and Chemical Separations Branch, Division of Reactor Development and Technology, USAEC, Washington, May 16, 1968.

R. K. Steunenberg
Salt Transport Process for Recovery of Fast Breeder Reactor Fuels. Part I. Background and General Status
Presented at Oak Ridge National Laboratory, July 17, 1968.

M. Tetenbaum
High Temperature Vaporization Properties of Hypostoichiometric Urania
Presented to the Department of Chemistry, DePaul University, Chicago, March 29, 1968.

M. Tetenbaum
Thermoelectric Properties of UP-US and UP-ThP Systems
Presented at Actinide Review Meeting, Argonne, May 27, 1968.

M. Tetenbaum, P. D. Hunt
High Temperature Carbon Activity Measurements over Uranium Carbides
Presented at American Ceramic Society Meeting, Pittsburgh, October 7, 1968.

A. D. Tevebaugh
Review of Secondary Cell Work
Presented at Annual Review and Planning Meeting, Electrochemical Working Group Power Information Center, Philadelphia, April 16-17, 1968.

L. E. Trevorrow
Process Chemistry of $NpF_6$
Presented at Rocky Flats Fluoride Volatility Meeting, Golden, Colorado, June 24-25, 1968.

E. Veleckis, K. E. Anderson, F. A. Cafasso, H. M. Feder
Solubility of Nitrogen Gas and Sodium Cyanide in Liquid Sodium
Presented at AEC-ANL International Symposium on Sodium Technology and Large Fast Reactor Design, Argonne, November 7-9, 1968.

R. C. Vogel
The Work of the Chemical Engineering Division
Presented to Department of Chemical Engineering, Carnegie-Mellon University, October 17, 1968.

R. C. Vogel
The Non-Aqueous Processing of Spent Fast Reactor Fuels
Presented at LMFBR Program Office meeting, October 25, 1968.

R. C. Vogel, A. A. Jonke, R. K. Steunenberg
The Non-Aqueous Processing of Spent Fast Reactor Fuels
Presented at Symposium on Dry Reprocessing, Mol, Belgium, October 28-29, 1968.

R. C. Vogel
The Work of the Chemical Engineering Division
Presented at University of Notre Dame, November 20, 1968.

S. Vogler
Aqueous Processing Principles and Theory
Presented at USAEC Nuclear Safeguards Training Course, Argonne, October 28, 1968.

W. J. Walsh, I. O. Winsch, R. D. Pierce
Pyrochemical Processing of Nuclear Fuels
Presented at 61st Annual Meeting, A.I.Ch.E., Los Angeles, December 1-5, 1968.